MARITIME TRANSPORTATION RESEARCH AND EDUCATION CENTER
TIER 1 UNIVERSITY TRANSPORTATION CENTER
U.S. DEPARTMENT OF TRANSPORTATION

Rapid Assessment of Internal Erosion Damage and Erodibility in Levees

July 2020 – December 2023

Michelle Barry, Ph.D. (PI, University of Arkansas, mlbernha@uark.edu)
Clinton Wood, Ph.D., P.E. (Co-PI, University of Arkansas, cmwood@uark.edu)

Samuel Ross Hokett (M.S. Student)
Viktor Hoestbo (M.S. Student)
Edgar Ortega De La Cruz (M.S. Student)

FINAL RESEARCH REPORT
Prepared for:
Maritime Transportation Research and Education Center

University of Arkansas
4190 Bell Engineering Center
Fayetteville, AR 72701
479-575-6021

ACKNOWLEDGEMENTS

This material is based upon work supported by the U.S. Department of Transportation under Grant Award Number 69A3551747130. The work was conducted through the Maritime Transportation Research and Education Center at the University of Arkansas. The research team would like to thank the United States Army Corps of Engineers Little Rock District and the Crawford County Levee District for their assistance and for allowing access to the field test site.

DISCLAIMER

The contents of this report reflect the views of the authors, who are responsible for the facts and the accuracy of the information presented herein. This document is disseminated under the sponsorship of the U.S. Department of Transportation's University Transportation Centers Program, in the interest of information exchange. The U.S. Government assumes no liability for the contents or use thereof.

Contents

List of Figures

List of Tables

Executive Summary

Recent flooding events have tested the nation's levee systems and highlighted the vulnerability of our transportation system to disruptions and delays caused by natural disasters. Levee failures not only disrupt navigable waterways, but they can also impact rail and truck transportation. Most levee failures occur because of instabilities caused by internal and overtopping erosion. Sand boils are the most common signs of distress for levees experiencing underseepage or internal erosion. These surficial defects indicate that a path has developed through or below the levee in which water is able to freely move. In some cases, sand boils are low-risk and are left without repair, but in other cases, sand boils can indicate that a much larger problem exists below the surface. Sand boils are often remediated using relief wells, seepage berms, or cutoff walls; however, determining the extent of the damage within the levee is difficult, and estimating future performance of the levee without this information can be dangerous.

Traditional drilling and sampling techniques only provide discrete data points which can lead to ineffective repairs and wasted funds. Alternatively, seismic and electrical geophysical techniques can be used to assess large sections of levees in a timely manner to locate weak and saturated zones which often indicate locations where internal erosion damage may be present. The ability of geophysical methods to enable quick measurements of material properties over large areas was demonstrated in a previous project, MarTREC 5006, however, there is currently no widely accepted correlation between geophysical properties and many vital engineering properties such as erodibility. This means the data gathered from geophysical methods may be used to compare different sections of the same levee qualitatively, but they cannot be used to make a quantitative assessment of the levee for engineering purposes. This hampers efforts to identify which levee segments are in the greatest need of repair.

The main goal of this study is to develop a rapid technique for mapping and assessing erodibility and internal erosion damage. The research objectives include: (1) identify levees where sand boils, seepage damage, or erosion damage are present, (2) conduct laboratory tests on benchmark samples and samples retrieved from levees to define relationships between soil type, erodibility, and resistivity, (3) measure resistivity and shear wave velocity in the field and map internal damage using the relationships defined, (4) evaluate erosion predictions by comparing mapped damage with visible distress signs and collect samples to confirm these predictions (when possible).

A series of geophysical field trials were conducted to determine the most accurate and efficient methods and the best procedures for imaging internal erosion zones. Benchmark samples were used to further characterize soil erodibility and resistivity so that a more robust inspection system can be developed. By linking soil type and internal erosion potential to the field geophysical data, a more rapid and proactive approach can be taken to estimate the risk associated with a particular levee system and determine a mitigation strategy. In addition, the geophysical techniques allow for the eroded or damaged subsurface zones to be mapped to ensure efficient repairs are made with the limited funds available.

1 Introduction

Levee systems are critical to reduce the loss of property and life during floods. Hurricane Katrina and the associated levee failures resulted in the costliest disaster in terms of loss of life and property in US history. Hurricanes Sandy, Irma, Maria, Harvey, Ida, and Ian make up the next six most costly natural disasters. Due to urbanization and deterioration of flood protection infrastructure, even smaller events can result in large economic losses. For example, in the spring of 2019 alone, historic flooding in the Midwest led to $20 billion in damages (ASCE, 2021). The health and performance of the US levee systems could prove to be a major problem in the coming decades, where continued deterioration, urban development, and an increase in extreme weather events will test these structures to and beyond their capacity and significantly increase the risk associated with failure.

Erosion of soil during high water events is the primary cause of levee failures, with soil erosion occurring through overtopping and internal erosion (Bonelli, 2013). Without the condition and performance evaluation of a particular levee, there is no way to determine the risk associated with it. Typically, levees are evaluated based on a simple visual inspection program to identify critical or weak spots in the levee system. This method can detect surface distress or erosion failures, but it cannot identify defects that exist within the inner core or foundation soil that could lead to failure during a future extreme event. Even when sand boils exist, knowing the extent of the damage below the surface is impossible with the visual inspection methods used. The drilling and sampling methods traditionally used to obtain internal soil data are extremely time intensive, they damage the levees, and they only provide a small amount of discrete data. Therefore, there is a need for a rapid and non-destructive assessment procedure that can quickly and cost-effectively gather continuous data, so that the most accurate performance evaluation can be made. The ability to quickly identify critical areas within a levee system so that they may be monitored or repaired is crucial if the levee system is to be improved with the limited federal funds available. While overtopping erosion is easily assessed with visual methods, determining the extent of internal erosion damage with visual methods alone is problematic.

This research focuses on the geophysical assessment of internal erosion damage in levees and laboratory erosion and resistivity methods that can be used to provide a quantitative estimate of soil erodibility and link it with the field geophysical methods. Electrical and seismic geophysical methods were used to investigate internal erosion damage at the Crawford County Levee System in Van Buren, AR to determine the extent and resolution that could be detected.

2 Literature Review

2.1 Levees in the United States

There are approximately 100,000 miles of levees in the United States (US), protecting an estimated 17 million people and $2.3 trillion in property value (ASCE, 2021). Levee systems in the US received a “D” rating corresponding to “Poor, at Risk” infrastructure in the most recent 2021

Infrastructure Report card produced by the American Society of Civil Engineers (ASCE), (ASCE, 2021). These levees are aging and many are near or even beyond their design life and require significant annual maintenance and repairs. With the limited amount of funding available, prioritizing repairs and maintenance activities for the most critical levees is important.

The United States Army Corps of Engineers (USACE) operates the National Levee Database (NLD) to inventory and assess levee systems. The data in the NLD is used to estimate the levee safety action classification (LSAC) rating (also contained in the NLD) which is used to communicate risk with levee personnel, stakeholders, and the general public. According to the most recent risk assessment, only 4 percent of levees within the USACE portfolio are classified as high or very high-risk, but approximately 45 percent of the population resides or works in these areas. More importantly, as of the publication of the 2021 Infrastructure report card, the USACE has inventoried 30,000 miles of levees, of which only approximately 75 percent have been assessed (ASCE, 2021). This means that the condition of the majority of the levees in the US is unknown and with the very limited funding available for the assessment of existing levee systems, there is a need for a cost-effective method capable of evaluating large sections of levees quickly.

2.2 Levee Failure Mechanisms and Internal Erosion in Levees

Various classification schemes for failure modes in levees have been proposed (e.g., Moss & Eller, 2007; USACE, 2021). For example, the USACE Engineer Circular on the Levee Safety Program (USACE, 2021) lists the most common potential levee failure modes as:

(a) Piping and internal erosion of soil embankments or foundations.
(b) Stability of embankments and floodwalls.
(c) Interaction between structures and embankments.
(d) Overtopping and breach of embankments.
(e) Riverside erosion and scouring of slopes.
(f) Failure due to operational issues such as inability to access and operate gates and closures.

Moss and Eller (2007) propose a classification of levee failure mechanisms based on loading types, including seismic loading, hydraulic loading during flooding, and loading under static conditions. These loading types lead to bearing, sliding, slumping and spreading, seepage, erosion, and overtopping failure mechanisms (Figure 1). Erosion of soil, whether from internal erosion or overtopping erosion, is the most common cause of levee and embankment dam failures (Bonelli, 2013). Seepage through levees can lead to internal erosion and piping, which may ultimately progress into levee failure. In a review of earthen dam failures, Richards and Reddy (2007) classified piping failures into four categories: foundation-related piping failures, conduit and internal erosion piping failures, suffusion piping failures, and piping failures due to biological activity. The review found that thirty-one percent of piping failures were due to backward erosion piping (BEP), with an additional fifty percent due to internal erosion and piping along conduits and structures. However, determining the type of piping failure responsible is often not possible

with the evidence of failure type being destroyed during embankment failures. Due to the prevalence of internal erosion-related levee failures, understanding internal erosion mechanisms is critical for assessing levee safety.

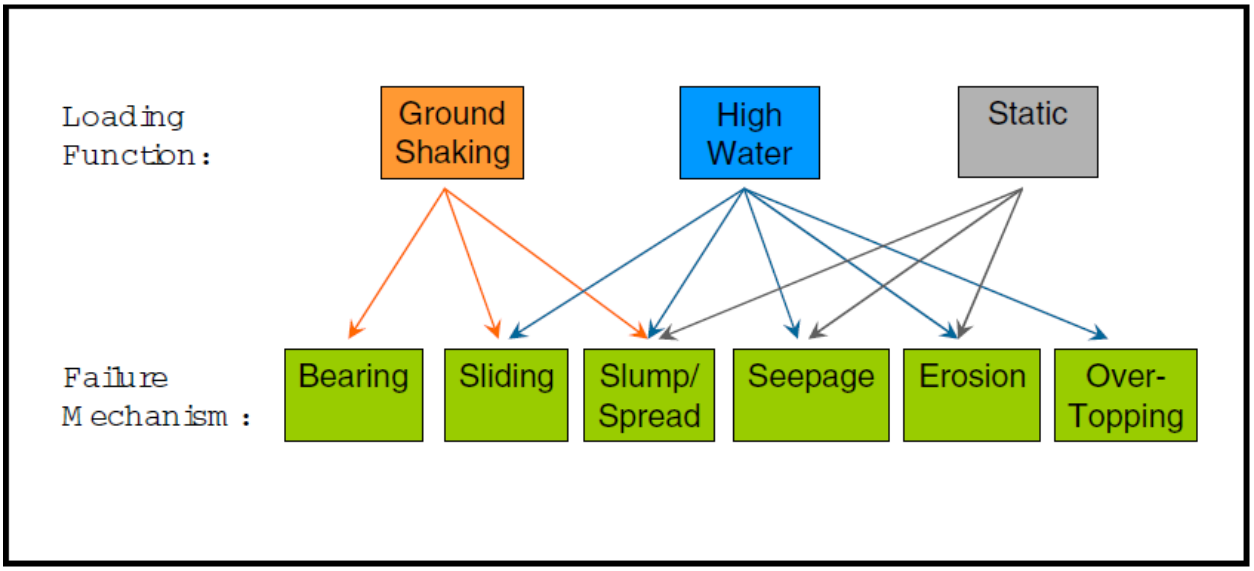

Figure 1 Relationship between loading type and failure mechanisms (Moss & Eller, 2007)

Internal erosion can be classified into four modes of initiation, including concentrated leak, backward erosion piping, suffusion, and contact erosion (Bonelli, 2013). In concentrated leak erosion, internal erosion initiates through an existing crack or pathway for water (e.g. cracks from differential settlement and conduits) (Bonelli, 2013). According to Bonelli (2013), concentrated leak erosion will progress into piping erosion if the soil holds open a pipe, there is sufficient hydraulic gradient, inadequate filtering of seepage, and the fracture remains open. Both plastic and dispersive plastic soils are susceptible to the concentrated leak erosion process (Bonelli, 2013).

Backward erosion piping requires the formation of an open pipe in the subsurface and typically occurs in levees when there is a cohesive layer (or structure) overlying a cohesionless layer. For levees located along meandering rivers, the common depositional sequence of fine-grained floodplain deposits overlying coarse-grained channel deposits facilitates the open pipe formation required for BEP to occur. In BEP, groundwater seepage forces progressively remove soil particles, and modeling studies show that the hydraulic gradient at the piping tip controls whether continued piping progression will occur (Robbins & Griffiths, 2019). If the BEP progresses to the upstream water source, rapid enlargement of the pipe and levee failure is likely (Robbins & Griffiths, 2019). Under the hydraulic gradients typical for levees, only non-plastic soils are susceptible to BEP (Bonelli, 2013).

In suffusion erosion, fine-grained soil particles are eroded and transported through the pores of the coarse-grained matrix material. Suffusion typically occurs in well-graded or gap-graded materials such as colluvium and glacial deposits (Bonelli, 2013). For suffusion to occur, the fines must be small enough to flow through the coarse-grained matrix, the volume of matrix space must be

greater than the amount of fines, and there must be sufficient flow velocity to transport the fines (Bonelli, 2013). Only non-plastic soils are typically susceptible to suffusion (Bonelli, 2013).

Contact erosion occurs along an interface between different soil types (e.g., coarse-grained sand and silt or the levee body and in-situ foundation materials)(Bonelli, 2013). In contact erosion, the finer-grained soil is eroded due to higher seepage velocities within the coarser-grained material and transported within the coarser-grained soil. Similarly to suffusion erosion, the pore spaces of coarse-grained material must be large enough to transport the fine-grained material, and the seepage velocity must be high enough to transport the fine-grained material (Bonelli, 2013). Contact erosion in levees may result in sinkhole formation, piping erosion, and slope stability failures (Bonelli, 2013).

Surface erosion damage during levee overtopping can easily be assessed using visual methods. However, determining the extent of internal erosion damage is not possible using only visual methods. During USACE levee inspections, sand boils, and saturated areas are noted as signs of excessive seepage (Flood Damage Reduction/System Inspection Report, n.d.). Sand boils are cone-shaped deposits of granular materials that form on the land side of levees due to seepage induced by high vertical hydraulic gradients (Robbins et al., 2020). A conceptual model of sand boil formation and subsequent backward erosion piping development from Robbins et al. (2020) is presented in Figure 2.

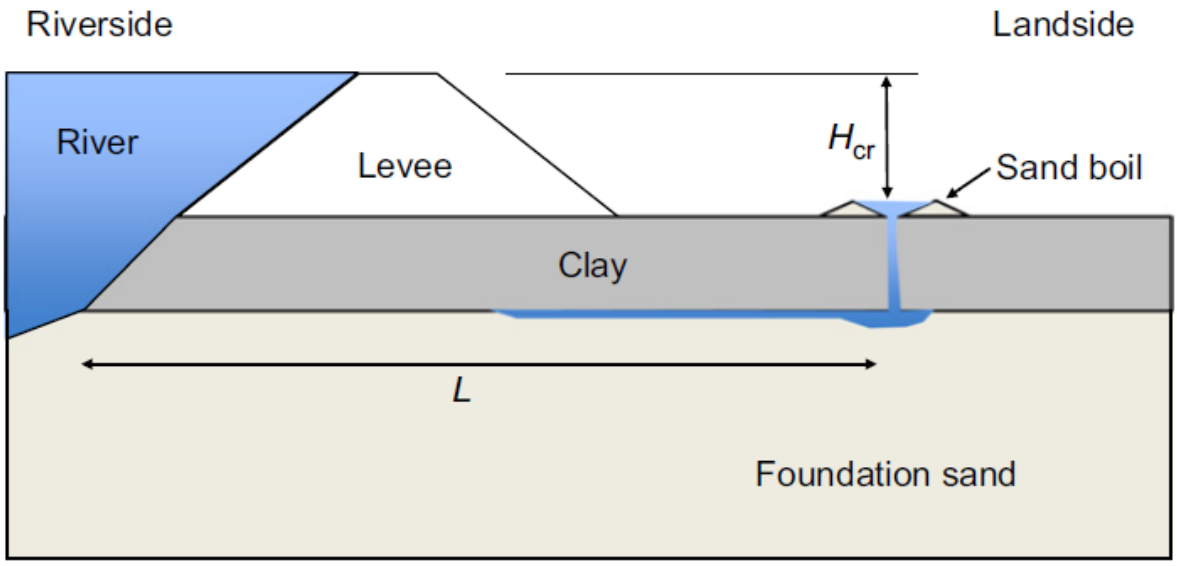

Figure 2 Conceptual model of sand boil formation and subsequent backward erosion piping with typical foundation materials for levees along meandering rivers (Robbins et al., 2020)

The vertical gradients required for sand boil formation are generated during flooding due to the presence of a confining layer on the landside of the levee. These confined groundwater conditions lead to high uplift forces and sand boil formation through defects in the confining layer (Schaefer et al., 2017). Additionally, the confining layer may fracture from the uplift forces leading to sand boil formation at the point of concentrated flow (Robbins et al., 2020). Sand boils may continue

increasing in size during BEP through levees, and if the BEP process reaches the riverside of the levee, settlement, and breaching will likely occur (Robbins et al., 2020).

While sand boils may progress into complete BEP failures of levees, they often do not. The critical head for BEP in levees is the head across the levee at which piping will propagate until levee failure occurs (Van Beek et al., 2015). However, the piping progression may stabilize if the horizontal gradient is less than the critical gradient. The horizontal gradient at sand boils is generally low due to long seepage distances, and this is likely the reason many sand boils do not lead to levee failures (Schaefer et al., 2017). However, the horizontal gradient at levees is difficult to determine as head losses in the soil, piping zone and sand boil affect the horizontal gradient. (Schaefer et al., 2017; Van Beek et al., 2015). Due to these factors, visual identification of sand boils alone cannot determine the extent of internal erosion in a levee. Geophysical methods provide a method to map internal erosion and determine which sand boils may be in danger of progressing to BEP failures, but a link to erodibility is needed if they are to be robust and capable of assessing levees to the extent necessary.

2.3 Electrical Resistivity Methods

The electrical resistivity (ER) of a material is a measure of the resistance of the material to the flow of electrical current. The ER method was introduced in the 1920s and is one of the most commonly used geophysical methods (Loke et al., 2013). Electrical resistivity, often in combination with other geophysical methods, has been used widely in geotechnical engineering for the assessment of levees and embankment dams (e.g., Rahimi et al., 2018, 2019; Tucker-Kulesza et al., 2019). The objective of the ER method is to determine the subsurface distribution of ER.

In the simplest form of the ER method, electrical current is injected into the ground with two electrodes (current electrodes), and the resulting voltage is measured with another pair of electrodes (potential electrodes). To calculate the apparent resistivity of the subsurface, the current injected at the current electrodes, the voltage measured at the potential electrodes, and the electrode array geometry are required (Loke et al., 2013). This apparent resistivity value represents the subsurface resistivity distribution that would be due to a homogenous half-space and the same electrode arrangement (Kuras et al., 2006; Loke, 2022). The apparent resistivity is equal to the product of the measured resistivity and the geometric factor for the chosen array type. Solving for the true subsurface resistivity distribution requires an inversion of the apparent resistivity data.

Electrical resistivity methods can be divided into static or dynamic methods depending on the acquisition type. In static methods, electrodes are staked into the ground during surveying, while in dynamic methods, the electrodes are moved during surveying (e.g. Capacitively Coupled Resistivity (CCR) methods)(Loke, 2022). Until the late 1980s, primarily one-dimensional (1-D) ER surveying was performed using profiling and sounding methods (Loke et al., 2013). In the profiling method, the distance between the current and potential electrodes remains constant as the current and potential electrodes move along the survey line. In the sounding method (also known

as vertical electrical sounding (VES)), current and electrode pairs are moved at increasing distances about the center point of the survey line (Samouëlian et al., 2005). As the distance between the current and potential electrodes increases, the volume and depth of the soil surveyed increase (Loke, 2022). Early VES surveys were processed qualitatively using sounding curves and later with computer inversion in the linear filtering method (Loke et al., 2013). The sounding method assumes the subsurface is a series of horizontal layers and does not account for lateral changes along the survey line. Two-dimensional (2-D) and higher ER surveys allow for more realistic subsurface models.

Multi-electrode ER systems first became available in the late 1980s and typically consist of 25 or greater electrodes (Loke et al., 2013). These systems feature a control box that injects current at two electrodes and can measure potential across multiple sets of potential electrodes (for multichannel systems). Multichannel systems may take hundreds of measurements for a chosen array type. An example of the series of measurements using the Wenner array to build a pseudo section is shown in Figure 3 (Loke, 2022). Surveys using these systems are commonly referred to as Electrical Resistivity Tomography (ERT) surveys, although ERT can refer to any method that produces 2-D or higher ER images (e.g., CCR). While these systems can perform three-dimensional (3-D) and four-dimensional (4-D)(i.e., variable in time) surveys, 2-D surveys are the most economical for many applications (Loke, 2022). Two-dimensional ERT surveys allow for detecting both horizontal and vertical changes in the subsurface. However, 2-D ERT relies on the assumption that there is no change in resistivity perpendicular to the survey line.

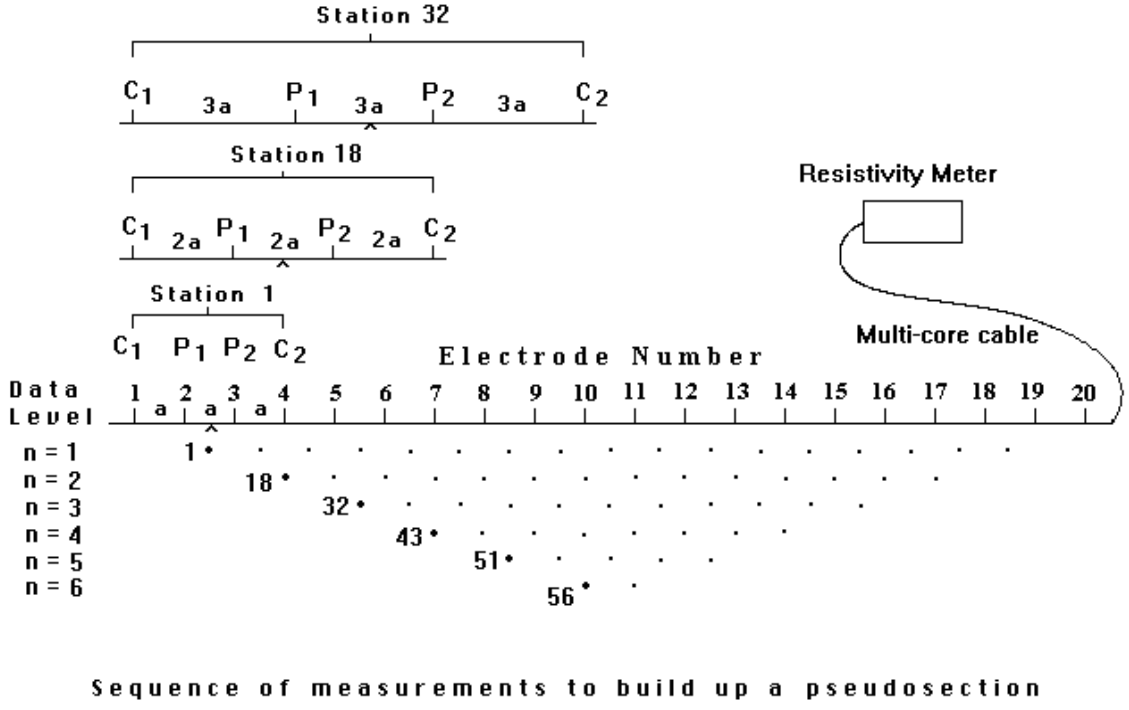

Figure 3 The series of measurements in a Wenner array to build a 2-D pseudo section of apparent resistivity measurements (Loke, 2022)

Electrode arrays in direct current (DC) ER methods refer to the arrangement of electrodes for injection of current and measurement of potential. The selection of array types is an important consideration when planning an ERT survey and controls the geometric factor used in calculating apparent resistivity. Moreover, different array types may be better suited for the geological target of interest. The most commonly used array types in 2-D ERT are Wenner, dipole-dipole (DD), Wenner-Schlumberger, pole-pole, pole-dipole, and multiple gradient arrays (Loke, 2022; Samouëlian et al., 2005). This ERT surveying for this research utilized 2-D, multiple gradient, and dipole-dipole array types; accordingly, these array types are the focus of this literature review (Figure 4).

In the DD array, the current is injected at two electrodes (electrodes A and B) and potential (electrodes M and N) is measured across another set of electrodes (Figure 4). In a dipole-dipole survey, the depth of investigation is increased by increasing the distance between the current and potential electrode pairs. The DD array is more sensitive to horizontal changes in resistivity (e.g., voids, dikes) than vertical changes (e.g., horizontal stratigraphy changes) (Dahlin & Zhou, 2004; Loke, 2022). Additionally, the DD array is more sensitive to noisy site conditions and has poorer resolution at depth than other array types (Dahlin & Zhou, 2004).

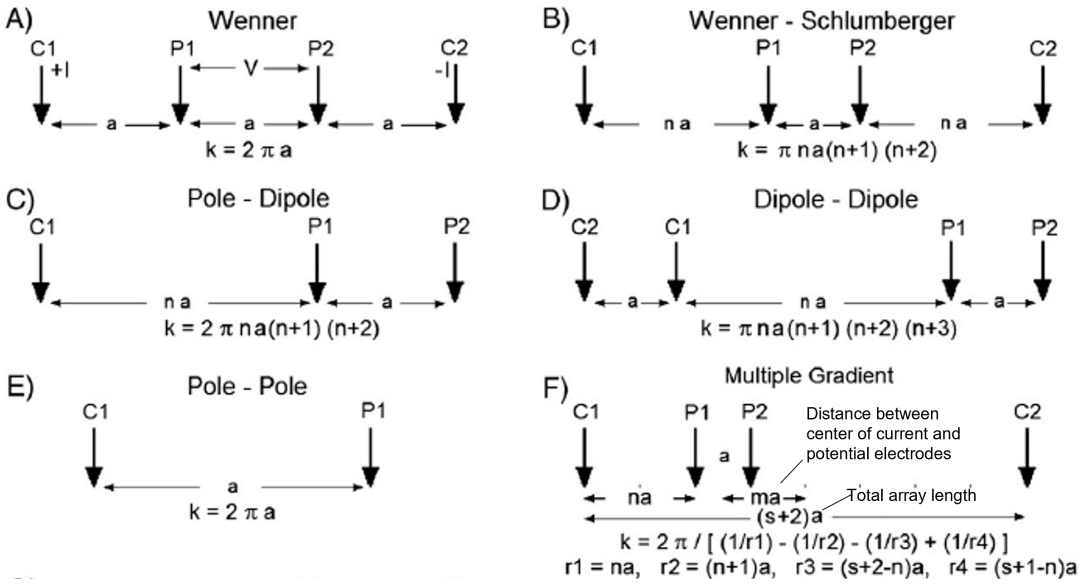

Figure 4 Common electrode array types and geometric factors (k) (modified from Loke et al. (2013))

Multiple gradient arrays were developed for usage with multichannel ER systems and allow for simultaneous measurement of potential at multiple electrode pairs while current is injected at an electrode pair (Figure 4). These arrays allow for more efficient ERT surveys without compromising the ERT image quality and produce inverted imagery comparable to more traditional arrays (e.g. Wenner, dipole-dipole, and Schlumberger) and a high signal-to-noise ratio (Dahlin & Zhou, 2004, 2006). This research uses a combination of the dipole-dipole array and the strong gradient array. In the strong gradient array, the current is injected into an outer pair of electrodes, and the potential is measured across each electrode pair within the current electrode

(Sean, 2019). The strong gradient array measurement sequence moves each current electrode spacing sequentially through the array, which produces a strong signal-to-noise ratio and reduces the number of measurements (Sean, 2019).

The primary disadvantage of DC ERT surveys is that installing electrodes and collecting the required data is very time-consuming. Additionally, increasing the number of electrodes to cover a larger area increases data acquisition time. Conversely, in dynamic methods, the survey area is increased by dragging the array of transmitters and receivers (Loke, 2022). The capacitively coupled resistivity (CCR) method of ER is commonly applied to evaluate levees and embankment dams (e.g., Rahimi et al., 2018, 2019). The CCR method utilizes capacitive line antennas as the receiver and transmitter dipoles in a towed dipole-dipole array allowing for rapid acquisition of ER data over large areas (e.g., entire levee systems). In CCR surveying, capacitive coupling of the transmitter and receivers to the surface allows for the initiation of current flow in the soil and measurement of voltage across the DD array without the need for staked electrodes (OhmMapper TR1 Operation Manual, 2001).

After completing an ER survey, a pseudo section of apparent resistivity versus pseudo depth is plotted. Standard pseudo section plotting convention places the measured apparent resistivity at the center of the current and potential electrodes. The measured apparent resistivity is often placed vertically by intersecting lines at 45 degrees between the current and potential electrodes. Once plotted, the pseudo section is useful for removing anomalous points from the apparent resistivity data. To determine the subsurface distribution of ER, first, numerical methods (e.g., finite difference, finite element) are used to forward model the apparent resistivity distribution, then inversion methods are used to find the ER distribution that results in the modeled apparent resistivity (Loke, 2022; Loke et al., 2013).

The resolution of an ER survey must be considered when interpreting the survey results. In general, for staked DC ERT surveys, the highest horizontal resolution is taken to be half of the electrode spacing. However, increased dipole spacing is required to obtain deeper subsurface information, leading to decreased resolution with depth. The resolution of surface ER methods decreases exponentially with depth (Loke, 2022). Additionally, the influence of offline features (e.g., a zone of internal erosion damage that is offset from and parallel to the survey line) must be considered when interpreting the results of DC ERT surveys. Generally, the horizontal influence of an offline interfering object is taken to be equal to the depth of the interfering object (i.e., the width of horizontal influence on a survey line increases with depth). Other important considerations when interpreting the results of an ER survey include poor current penetration due to surficial high or low ER layers, depth of investigation (generally one-fifth to one-sixth of the array length), and non-uniqueness of the subsurface model (Loke, 2022).

The ER of natural materials is dependent on many factors, which leads to a significant overlap in the resistivity values of materials. The ER of igneous and metamorphic rocks is largely dependent on the degree of fracturing and the presence of fluid-filled fractures (Loke, 2022). For sedimentary rocks, ER is primarily controlled by porosity and the composition of pore fluids (Loke, 2022). An

early relationship referred to as Archie's Law relates the ER of a saturated soil to the soil porosity, pore fluid ER, and constants related to the soil solids and pore structure (Abu-Hassanein et al., 1996; Archie, 1942). In Archie's Law, the soil ER increases as porosity and porewater ER increases; however, Archie's Law is primarily applicable for granular soils with free pore water (Abu-Hassanein et al., 1996; Mofarraj Kouchaki et al., 2019). Electrical resistivity values of soils are influenced by porosity (both distribution and connectivity of soil pores), pore fluid conductivity, soil mineralogy, particle size distribution and orientation, saturation level, and temperature (Abu-Hassanein et al., 1996; Mofarraj Kouchaki et al., 2019; Rein et al., 2004; Samouëlian et al., 2005). In sand and gravel-sized material, electrical conduction is primarily within the pore fluids (Abu-Hassanein et al., 1996). In clays, electrical conduction occurs both in the pore water and along the surface of clay particles (Abu-Hassanein et al., 1996). Significant overlap in the resistivity ranges of different USCS soil types, as shown in Table 1, makes the determination of soil type based on ER alone problematic.

Table 1 Resistivity ranges of USCS soil types (modified from (Mofarraj Kouchaki et al., 2019))

USCS Soil Type	Resistivity (Ω.m) (Kaufman and Hoekstra, 2001)	Resistivity (Ω.m) (Palacky, 1987)
CH	10-50	3-100
CL	24-60	-
OL	27-75	-
ML	27-73	-
SC	47-178	-
MH	72-240	-
SM	96-453	475-10,000
GW	563-918	475-10,000
GC	129-405	-
GP	915-2,333	-

A study by (Mofarraj Kouchaki et al., 2019) investigated the effect of pore water composition, water content, saturation level, density, and temperature on laboratory measured ER. The study found that under saturated conditions, the measured ER is not sensitive to soil density, and the soil types tested were easily distinguished by ER when fully saturated. These results support that the soil type for saturated soils can potentially be determined using ER. The height of the capillary fringe above the water table must be considered when interpreting ERT data to estimate soil type. The zone of capillarity can extend the saturated zone and high saturation levels many meters above the water table. Generic Soil Water Characteristic Curves (SWCC) can estimate the capillary fringe height above the water table and aid in the interpretation of ERT data (Kouchaki et al., 2019). Additionally, Mofarraj Kouchaki et al. (2019) showed that the ER of soils is highly dependent on saturation levels up to approximately 60 percent saturation. The dependence of

measured ER on saturation level makes differentiation of soil types above the water table problematic and requires developing site-specific relationships (Kouchaki et al., 2019; Rahimi et al., 2018).

Temporal changes in ER must also be considered when interpreting ER data collected over extended periods. A long-term DC ER monitoring study by (Rein et al., 2004) found that natural changes to subsurface ER are primarily due to changes in soil saturation, soil and groundwater temperatures, and groundwater ionic concentration. The temporal changes in the saturation of soils are primarily due to groundwater level fluctuations and water content changes within the vadose zone. Rein et al. (2004) found that changes in saturation and near-surface soil temperature have the largest influence on ER.

2.4 Surface Wave Methods

Seismic waves are classified as body waves and surface waves. Body waves occur within the surface of a medium and are either compressional waves (P-Waves), with particle motion parallel to the propagation direction, or shear waves (S-Waves), with particle motion perpendicular to the propagation direction. Surface waves occur at the interface between a free surface and a medium (e.g., the ocean floor or the surface of the earth) due to the interaction of body waves. The primary surface waves of interest for geophysical site characterization are Rayleigh waves and Love waves (Figure 5).

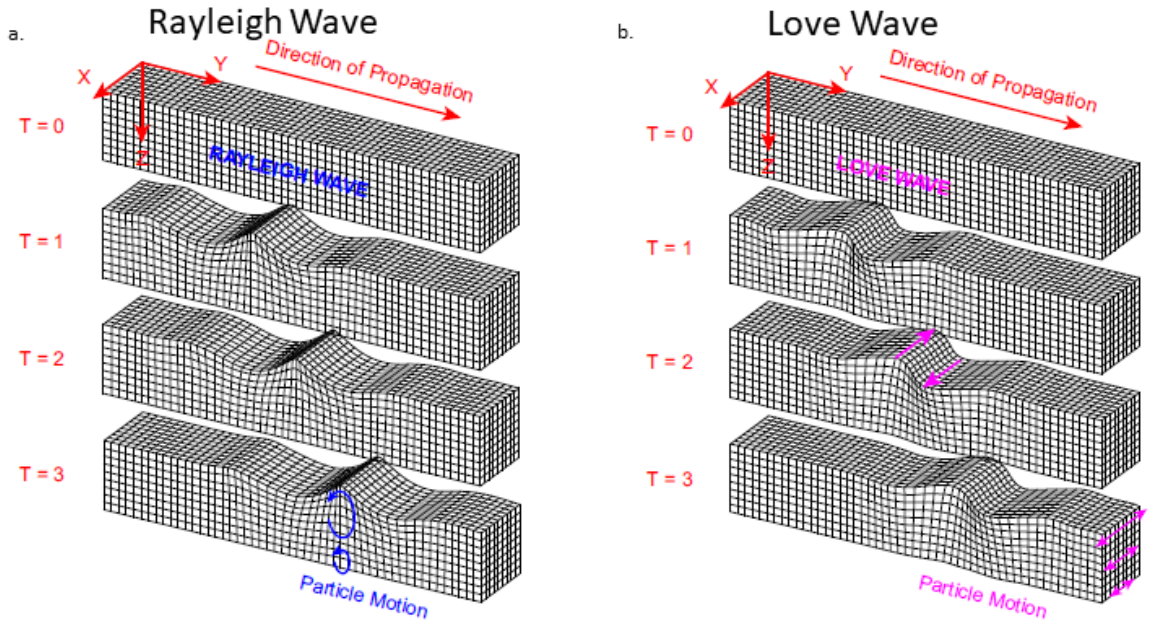

Figure 5 The direction of propagation and particle motion of a) Rayleigh Waves and b) Love waves (modified from (Dal Moro, 2015))

The multichannel analysis of surface waves (MASW) method relies on the dispersive nature of surface waves to obtain the subsurface distribution of shear wave velocity (Vs). As a result of surface wave dispersion, the depth of materials influencing surface wave propagation increases as

the wavelength (λ) of a given surface wave component increases. For typical geotechnical applications, the frequency content of surface waves utilized ranges from 4-50 Hz, and as a rule of thumb, the maximum depth influencing surface wave propagation is taken as λ/2 to λ/3 of the longest wavelength resolved (Dal Moro, 2015).

The Vs of a material is directly related to the shear modulus and stiffness of the material. Accordingly, the generation of 2-D Vs profiles along levees can delineate subsurface stratigraphy and anomalous zones in levees and dams (e.g., Rahimi et al., 2018, 2019). Multichannel Analysis of Surface Waves can be performed using active sources (e.g., sledgehammer surveys, drop weights, vibroseis, explosives) or passively generated surface waves from ambient noise (e.g., waves along sea levees, wind turbines, traffic). The frequency content from active sources generally provides the depth of exploration needed for many geotechnical applications. However, passive sources can provide the required low-frequency content when deep Vs profiles are required.

Active source MASW data is collected using a linear array of geophones and can be performed with the same data acquisition system used for traditional refraction surveys. For typical geotechnical applications, a linear array of 24 to 48 horizontal or vertical geophones are used for MASW surveys acquired using Love or Rayleigh Waves, respectively. A sledgehammer source is adequate for many applications, with Love Waves generated by horizontal blows to a shear beam and Rayleigh Waves generated by vertical blows to a steel plate.

In MASW data acquisition, no mid-array sources are required; typically, multiple source offsets off each array end are acquired. At each source location, sledgehammer blows are stacked to increase the signal-to-noise ratio. In sledgehammer surveys, a trigger mounted to the sledgehammer initiates seismograph recording of the seismic record. The array geometry, length of the seismic record, and sampling interval (digital sampling of the analog signal from geophones) must be selected considering both the survey objectives and geological conditions (Dal Moro, 2015).

Once the MASW data are collected, the data must be transformed from the offset-time domain to the frequency-velocity domain to generate a frequency-velocity spectra. Notably, this phase-velocity spectra is a product of mathematical operations prior to any interpretation, and any subsequent products require user interpretation of the phase-velocity spectra (Dal Moro, 2015). Various transformations exist to generate a frequency-velocity spectra of the acquired MASW data, and common transformations include the frequency-slowness, frequency-wavenumber, frequency domain beam former, and phase shift transformations (Rahimi et al., 2021). The frequency domain beam former method (FDBF) developed by (Zywicki, 1999) was utilized to generate the frequency-velocity spectra for this research and generally provides the highest resolution for most geological conditions (Rahimi et al., 2021).

After generation of the frequency-velocity spectra, dispersion curves are created through interpretation of the frequency-velocity spectra. This research uses the multiple source offset method, where the maximum spectral peak for each source offset is automatically picked to reduce

user bias (Cox & Wood, 2011). The automatically picked points of maximum spectral acceleration are then combined into a composite dispersion curve. The use of multiple source offsets aids in the identification of higher modes, identification of near-field and far-field effects and provides an estimate of the uncertainty in the dispersion data (Cox & Wood, 2011). Once the final experimental (i.e., the field data) dispersion curve is obtained, an inversion process is performed to obtain a 1-D Vs profile. In addition to MASW surveys, horizontal-to-vertical spectral ratio (HVSR) tests were performed on the levee crest and landside toe to allow for joint inversion of the MASW data. The joint inversion of MASW data and HVSR peaks allows for the greater constraint of inversions at depth, as there is limited low-frequency content when using a sledgehammer source. Further details of dispersion curve processing and the inversion process are presented herein.

The resolution and depth of investigation of the MASW method are important considerations for interpretation of the resulting 2-D Vs profiles. Generally, the vertical and horizontal resolution of the MASW method are taken as twice the receiver spacing and 10 percent of the array length, respectively (Moody, 2017). Additionally, the resolution of the active source MASW method decreases with depth resulting in greater uncertainty in the Vs profiles at depth (Foti et al., 2015). Generally, for the MASW method, the depth of investigation can be estimated as half the length of the array (Foti et al., 2015). However, following experimental data collection, the depth of investigation is generally controlled by the maximum measured wavelength observed in the experimental dispersion curve.

2.5 Existing Research on Geophysical Assessment of Internal Erosion Damage in Levees

Geophysical methods allow for rapid assessments of levees and are continuous, cost-effective, and non-destructive. Geophysical methods commonly applied to levee assessment include ER methods, electromagnetics (EM), Seismic Refraction Tomography (SRT), MASW, and Ground Penetrating Radar (GPR) (Barner et al., 2001; Dunbar et al., 2003, 2007; Hayashi & Konishi, 2010; Rahimi et al., 2018; Wodajo et al., 2019). The geophysical properties measured by these geophysical methods allow for detecting defects in levees. For example, in ER and EM surveys, the measured ER/conductivity can be used to estimate the subsurface distribution of soil types. The presence of reflections and refractions in GPR data can be used to detect shallow levee defects (e.g., animal burrows). In MASW and S-Wave SRT, a 2-D profile of shear wave velocity is generated and allows for the identification of low Vs zones, which may represent levee defects. Similarly, the measured P-Wave velocity in P-Wave SRT can identify low Vp zones due to levee defects. Additionally, the measured Vp from SRT can identify the line of saturation in levees. The following sections will first review studies on the general geophysical assessment of levees (e.g., determination of foundation and levee soil types), followed by a review of studies on the geophysical assessment of internal erosion and erodibility in levees.

Electrical resistivity and EM methods are commonly applied to levees to determine soil type in the foundation and bodies of levees (Dunbar et al., 2003; Gillip & Payne, 2011; Llopis & Simms, 2007; McKenna et al., 2006). These methods can detect coarse-grained channel deposits that cross underneath levees and characterize the fine-grained floodplain deposits present on the landside of

levees. Continuous geophysical characterization of levee foundation materials provides insights into the geological controls on internal erosion in levees. Llopis and Simms (2007) investigated the foundation conditions at California levees using CCR, DC ERT, and EM. The CCR, DC ERT, and EM surveys yielded comparable results and were used to produce 2-D soil profiles and identify anomalous zones in the foundation soils. The study found CCR and EM methods the most effective; however, the EM methods required multiple passes, while the Ohm-Mapper five receiver CCR unit allowed collection in one pass. Similarly, McKenna et al. (2006) successfully applied EM and CCR surveys to map an obscured paleo-channel deposit under a levee on the Rio Grande River in Texas. The study observed a sharper anomaly response to the paleo-channel in the CCR data than in the EM data, potentially due to anthropogenic noise at the site.

Airborne multi-frequency EM surveys have been effectively used for large-scale characterization of levee systems and targeting of higher resolution surface-based geophysics (Dunbar et al., 2003, 2007a). Dunbar et al. (2003) used aerially collected EM along 270 miles of the levee on the Rio Grande in Texas to identify anomalous regions for surface geophysical testing. The airborne collected EM data displayed an overall smoother profile when compared to surface-based EM due to the lower resolution of airborne methods. While airborne EM can be valuable for assessing levees, the method is significantly more expensive than surface-based geophysics.

Ground penetrating radar has been applied to assess damage from burrowing animals in levees that may lead to internal erosion in levees (Barner et al., 2001; Chlaib et al., 2014). Chlaib et al. (2014) successfully used GPR to locate air-filled, water-filled, and clay-filled animal burrows at the Lollie Levee in Arkansas. However, levees are typically constructed with electrically conductive clay-rich soils, which severely limits the depth of investigation for GPR. Chlaib et al. (2014), for example, had a maximum depth of investigation of 1.05m at the Lollie Leeve. The limited depth of investigation of GPR in conductive soils limits the utility of GPR for the assessment of internal erosion in levees.

Multichannel analysis of surface waves is commonly applied to levee assessment. Pseudo 2-D Vs profiles generated by MASW can be used to identify low Vs anomalies corresponding to levee defects. Lane et al. (2008) used the MASW method at the Citrus Lake Levee in Louisiana in an early application of the method for levee evaluation. The surveys successfully detected lateral and vertical changes in subsurface materials consistent with on-site boring logs in a seismically active area that would be problematic for refraction-based methods. Additionally, low Vs anomalies potentially representing levee defects were resolved; however, due to the prevalence of higher modes and non-Rayleigh wave types in the dispersion data, Lane et al. (2008) suggested further numerical modeling of surface wave propagation in levees was needed. In the inversion of an MASW-derived dispersion curve, the assumption that the subsurface can be modeled as a layered elastic half-space is implicit (Karl et al., 2011). Karl et al. (2011) evaluated the validity of this assumption through numerical modeling and field studies. In the numerical modeling study, the dispersion curves of various synthetic levee models were compared to forward modeling of equivalent layered elastic half-space models. Karl et al. (2011) found that for levees with a width-

to-height ratio greater than four, the subsurface at a levee can be modeled as a layered elastic half-space. The modeling included the presence of a velocity inversion and verified the application of MASW to detect low Vs anomalies in levees. In addition to active source MASW methods, passively sourced surface wave methods have been applied to levee evaluations. Kita et al. (2013) applied the 2-D Linear Array Microtremor Survey (2D-LAMS) method to levee evaluation, finding the combination of 2D-LAMS and active source MASW effective for obtaining high-resolution data for levee body and foundation materials.

Multiple geophysical methods are often applied to levee evaluations to provide complementary information. Dunbar et al. (2007b) performed multiple method time-lapse geophysical monitoring during a ponding experiment on a section of the Retamal Levee in Texas. Time-lapse geophysical monitoring included ERT, spontaneous potential (SP), GPR, SRT, and MASW. Landstreamer applied MASW effectively detected increasing Vs due to the hydration of levee soils, leading to increased soil density during the ponding experiment. Additionally, Vs measured by MASW was the material property most sensitive to hydration-induced soil density increases during the ponding experiment. Notably, Dunbar et al. (2007b) found the accurate measurement of Vs using SRT problematic due to the influence of levee geometry. Two–dimensional ERT was successful in monitoring changes in soil moisture content; however, SP was unsuccessful in detecting anomalous seepage during the ponding experiment, likely due to the low permeability of the levee. Dunbar et al. (2007b) highlight the complementary nature of Vs measured by MASW and ER measured by ERT in levee assessments.

Similarly, Cardarelli et al. (2010, 2014) applied MASW, SRT, and ERT to assess embankment dams. In combination with seismic methods, the studies found ERT capable of verifying the continuity of embankment and embankment foundation materials. Cardarelli et al. (2014) applied MASW and SRT (P-Wave and S-Wave) to characterize the body and foundation of an embankment dam, respectively, with the MASW data reaching twice the depth of investigation as the SRT data for the same data set due to increased attenuation of body waves. Samyn et al. (2014) applied integrated CCR and MASW geophysical surveys to assess sinkhole susceptibility along dykes on the Loire River in France. The study correlated CCR-derived ER to soil type using boring logs and found ERT valuable for detecting the flow of soils into karst networks. While Vs from MASW effectively determined the degree of karstification of the limestone bedrock below the Loire River dykes. By integrating ERT and MASW results, Samyn et al. (2014) produced a quantitative method of assessing sinkhole susceptibility. Similarly, the integration of MASW and ERT has the potential to provide an assessment of internal erosion and erodibility in levees. Rahimi et al. (2018) applied MASW and CCR to the Wood River Levee in Illinois to assess the levee body and foundation materials for defects causing internal erosion issues at the levee. The study successfully correlated Vs and ER to soil type, allowing for the determination of geological controls on internal erosion at the site. Shear wave velocity was correlated to soil type based on reference Vs curves from Lin et al. (2014) and blow counts from boring logs. The relationship between ER and soil type was primarily defined by comparison with boring logs. The relationships between soil types and geophysical properties developed allowed for the detection of paleo-

channels crossing underneath the Mel Price Levee. The paleo-channels were interpreted to have eroded the surface clay layer on the landside of the levee and correspond well to locations of sand boil clusters. Rahimi et al. (2018) demonstrate the complementary nature of CCR and MASW for assessing levees, finding CCR valuable for shallow characterization and MASW effective for deeper characterization.

Cross-plot analysis is another approach for the integration of multiple geophysical methods; cross-plot analysis of ER and seismic velocities combines the strengths of both seismic and ER methods for levee assessments (e.g., Goff et al., 2015; Hayashi & Inazaki, 2013; Hayashi & Konishi, 2010; Inazaki et al., 2008). The cross-plot analysis method has been applied extensively to Japanese levees, primarily utilizing CCR and MASW to measure ER and Vs, respectively. Inazaki et al. (2008) collected MASW and CCR data for cross-plot analysis on a 3000m levee reach with seepage and internal erosion issues. Cross-plots of Vs versus ER showed that seepage and piping zones in the levee foundation and body correspond to low Vs and high ER zones. Additionally, ground-truthing of CCR and MASW data at an open cut showed a clear relationship between mean grain size, allowing for estimation of permeability based on ER. Conceptually in cross-plot analysis, high ER and low Vs correspond to a dangerous, loose, and sandy levee condition, while low ER and high Vs correspond to a safe, stiff, and clayey levee condition (Hayashi & Konishi, 2010). Hayashi & Konishi (2010) applied cross-plot analysis using MASW and CCR to 1800m of levee on the Kuwano River in Japan to estimate soil type for both levee and foundation materials. The cross-plot criteria were developed by comparing measured ER and Vs with boring logs within the geophysical surveys. Hayashi & Inazaki (2013) used cross-plot analysis to estimate soil type on the Chikuma River levees in Japan and found anomalous seepage zones correlated to gravel zones from the cross-plot analysis. Hayashi et al. (2014) applied a more rigorous statistical approach to cross-plot analysis resulting in polynomial approximations for estimated soil type based on extensive geophysical surveys (CCR and MASW) and borings; however, these approximations were formulated based on Japanese levees and modifications may be necessary for other levee systems. Goff et al. (2015) applied the polynomial approximation developed by Hayashi et al. (2014) for statistical estimation of soil type at the London Avenue Canal levee, located along a brackish lake in Louisiana. The study found that the polynomial approximation developed for Japanese levees effectively estimates soil type for levees in the Mississippi River delta, although modification of the classification system was required to distinguish silts from clays. The existing studies on cross-plot analysis provide insight into the interpretation of ER and Vs derived from geophysical surveys on levees.

In a recent development for integrated geophysical assessment of levees, Arato et al. (2022) developed a “seiesmo-electric” land streamer that can acquire data for MASW and ERT. The siesmo-electric streamer combines a seismic land streamer with the galvanically coupled DC ER streamer developed by Comina et al. (2020). The electrical streamer consists of electrodes resembling wire brushes and a drip irrigation system to reduce electrode contact resistances, allowing for a towable galvanically coupled ER system (Comina et al., 2020). The towable array of electrodes allows for increased horizontal and vertical data coverage through the overlapping

of electrode arrays (e.g., shifting the array in 2m increments) and increased survey efficiency over traditional staked DC ERT surveys (Comina et al., 2020). Arato et al. (2022) implemented the siesmo-electric streamer on a levee crest of the Chisola River in Italy, finding the results consistent with staked DC ERT and standard land streamer acquisitions along the same line. Additionally, Arato et al. (2022) acquired transverse DC ERT lines, observing that the 3-D nature of levees leads to an averaging of ER in longitudinal lines (i.e., the measured ER does not precisely match for transverse and longitudinal ERT lines); accordingly, the 3-D nature of internal erosion in levees must be considered in the interpretation of 2-D geophysical data. As reviewed in the preceding section, there are numerous studies on the general geophysical assessment of levees. However, the research on geophysical assessment of internal erosion in levees is far more limited. The use of geophysical methods at internal erosion sites can allow for more effective levee repair and aid in determining the cause of internal erosion for a given site. Both surface wave and ER methods have been applied to assess internal erosion in levees. Time-lapse geophysical monitoring of levees can provide valuable information for assessing internal erosion. A study by Planès et al. (2016) used passive seismic interferometry (using passively generated surface waves) to monitor levees during internal erosion experiments at both the laboratory and field scales. The study found a 30 percent decrease in surface wave velocities during a field-scale internal erosion experiment and concluded that zones of severe internal erosion are likely detectable with surface wave methods. Similarly, Planès et al. (2017) used the same methodology for time-lapse monitoring of a Netherlands sea levee at a location with sand boils present. The time-lapse seismic interferometry monitoring showed anomalous surface wave velocity responses to tidal hydraulic loading in suspected internal erosion zones. Liu et al. (2021) used MASW and ERT in an embankment dam to locate a seepage zone characterized by low shear wave velocity. These studies indicate that zones of significant internal erosion are likely to produce low Vs anomalies in surface wave data. The use of time-lapse (at various time scales) ER surveys is more common than time-lapse surface wave methods to assess internal erosion. Sjödahl et al. (2010) used multiple ER and self-potential measurements during a field scale embankment test with defects blindly placed in the embankment. The study located several of the constructed defects; however, the defects were primarily detected through the use of time-lapse ER surveys. Rahimi et al. (2019) used a combination of ERT, CCR, MASW, and Full Waveform Inversion (FWI) to detect seepage channels at an embankment dam. The authors found seasonal ER measurements most effective for the detection of seepage channels and internal erosion zones.

The formation of sand boils is common on the downstream side of levees founded on the alluvial deposits of meandering rivers. Geophysical methods can investigate the geological controls on sand boil formation and the risk of sand boils progressing into piping failures. Both electrical and seismic geophysical methods have been used to assess levee internal erosion sites with sand boils present (Brackett, 2012; Kelley et al., 2019, 2019; Tucker-Kulesza & Rutherford, 2019; Wodajo et al., 2019). Kelley et al. (2019) used ERT to investigate under seepage and sand boil formation at the Preston Levee District on the Middle Mississippi River. Additionally, geological mapping, cone-penetrometer testing, laboratory testing of sand boil ejecta, and trenching of sand boils were

performed at the site. The ERT lines at the site were able to image the top stratum thickness and the seepage damage to the top stratum resulting in sand boil formation. The overall good agreement between ERT and CPT results in Kelley et al. (2019) demonstrate the utility of ERT in the assessment of internal erosion sites. Strange et al. (2016) used ERT to determine the geological controls of sand boil formation at the Tara Wildlife Lodge Area on the Lower Mississippi River Levee System. The ERT results showed that the impervious top stratum at the site is thin to nonexistent, leading to sand boil formation. Additionally, the ERT was valuable in the interpretation of the ridges and swales of the point bar deposits underlying the levee. Electrical resistivity methods combined with more traditional methods (e.g., geological mapping, invasive methods, laboratory testing) allow for more effective assessments of sand boil areas (Kelley et al., 2019; Strange et al., 2016; Tucker-Kulesza et al., 2019).

Cross-plot analysis of electrical and seismic geophysical data is another method to assess internal erosion sites on levees. In cross-plot analysis, levees are classified (in terms of safety) both on seismic velocities (Vs or Vp) and ER. Wodajo et al. (2019) used cross-plot analysis of SRT and ERT data to investigate an internal erosion site at the Francis Levee on the Mississippi River. Conceptually in cross plot analysis, as the seismic velocity increases and the ER decreases, the levee safety increases, the conceptual model of cross-plot analysis for Francis Levee from Wodajo et al. (2019) is presented in Figure 6. Wodajo et al. (2019) identified anomalous zones of low Vp and high resistivity on both the landside and riverside of the Francis Levee. Identification of anomalous zones aided in interpreting the geological cause of internal erosion at the site. Cross-plot analysis of seismic and electrical geophysical data has also been used to estimate soil type and soil parameters of levee materials (e.g., Hayashi et al., 2014, 2019). Hayashi et al. (2019) performed a cross-plot analysis utilizing CCR and MASW surveys, including approximately 670 km of surveys and 400 borings on Japanese levees. A database of shear wave velocity, ER, and soil properties (from borings) was created to allow for statistical estimation of soil type, percent fines content (Fc), the effective grain size (D20), and blow counts (N-value). However, the correlations were developed for Japanese levees and cannot be applied directly to other levee systems (Hayashi et al., 2019). While the development of cross-plot relationships to soil properties at the project site is beyond the scope of this research, the work of Hayashi et al. (2019) provides insight into the interpretation of ERT and MASW results at levees. Based on a review of the existing literature, ERT and MASW were determined to be the most effective for assessing internal erosion and erodibility in levees.

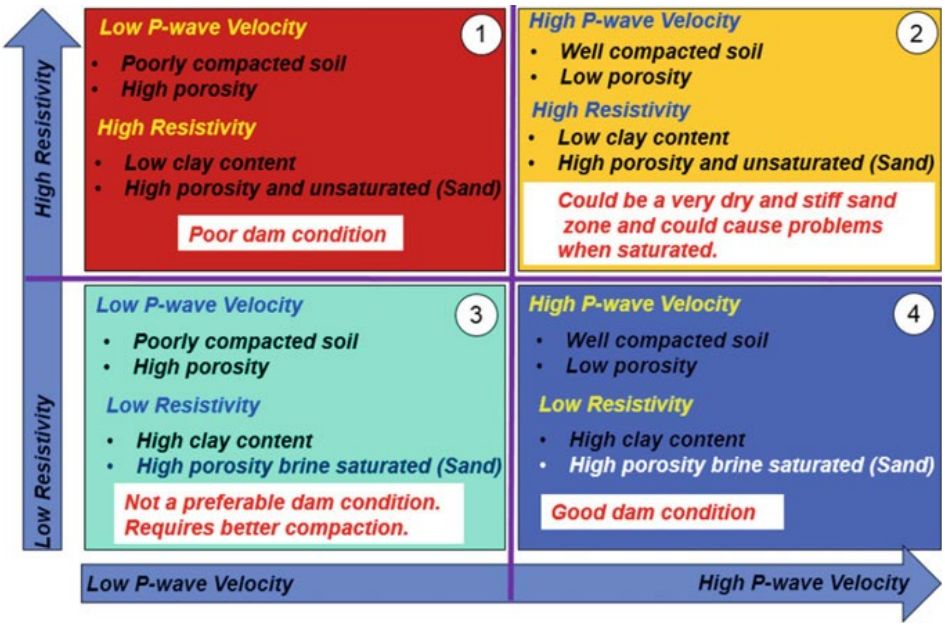

Figure 6 Conceptual design of the cross-plot analysis for the Francis Levee (Wodajo et al., 2019)

2.6 Soil Erosion Devices and Testing

2.6.1 Erosion Function Apparatus

There have been several methods developed to model erosion mechanisms in the laboratory and field in an effort to measure a soil's resistance to internal and surface erosion. The Erosion Function Apparatus (EFA) was developed by Briaud et al. in 1992 to predict the surface erosion rate of fine-grained soils to determine the scour depth at the end of a bridge's design life. The test is able to determine the relationship between the hydraulic shear stress at the soil-water interface and the soil's erosion rate which can be used to predict scour. The EFA was designed such that water circulates through a pipe containing a Shelby tube soil sample. The water flows across the soil sample surface to determine the amount of soil that erodes in a given time at different flow rates. Because the erosion rate is determined for different velocities and corresponding shear stresses, an erosion function can be developed and can be used to identify the critical shear stress, or the shear stress required to initiate erosion for that particular soil. The test can be used for any soil or core-able soft rock that can be sampled or placed within a Shelby tube. One of the benefits of the EFA is that the test can be performed on undisturbed samples that simulate actual field conditions. Figure 7 shows a schematic of the Erosion Function Apparatus.

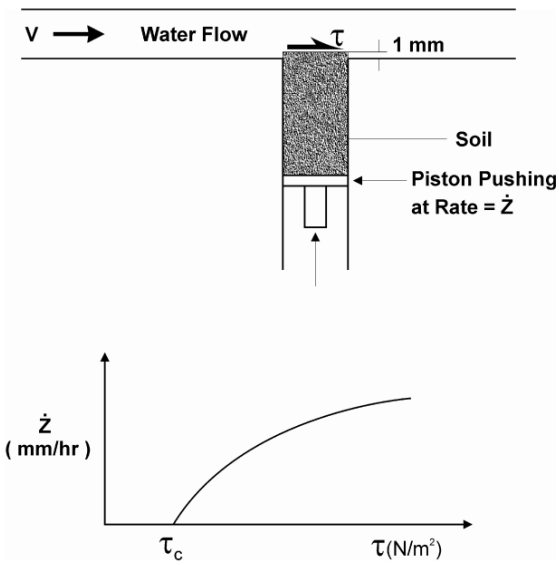

Figure 7 Schematic of the Erosion Function Apparatus (EFA) and corresponding measured erosion function (Briaud et al. 1999)

2.6.2 Jet Erosion Test

The Jet Erosion Test (JET) was designed by Hanson and Cook (2004) to study the scour erosion which may occur at a headcut or a free overfall (Wahl et al. 2010). This method uses a submerged hydraulic jet to produce scour erosion. The device development has been further expanded to include laboratory and field versions (Figure 8). This test estimates the critical shear stress needed to initiate erosion and the erosion rate to determine the erodibility parameters of the soil.

The Jet Erosion Test uses a jet of pressurized water to scour a soil sample to determine the critical shear stress and erosion rate. The test head during the test is commonly held constant during the test and the scour of the soil sample is measured over time during the experiment using a point gauge that passes through the nozzle. Because it is a water jet device, the shear stress at the nozzle exit can be directly calculated whereas many of the other erosion tests must use correlations or estimates in order to obtain the shear stresses applied to the soils.

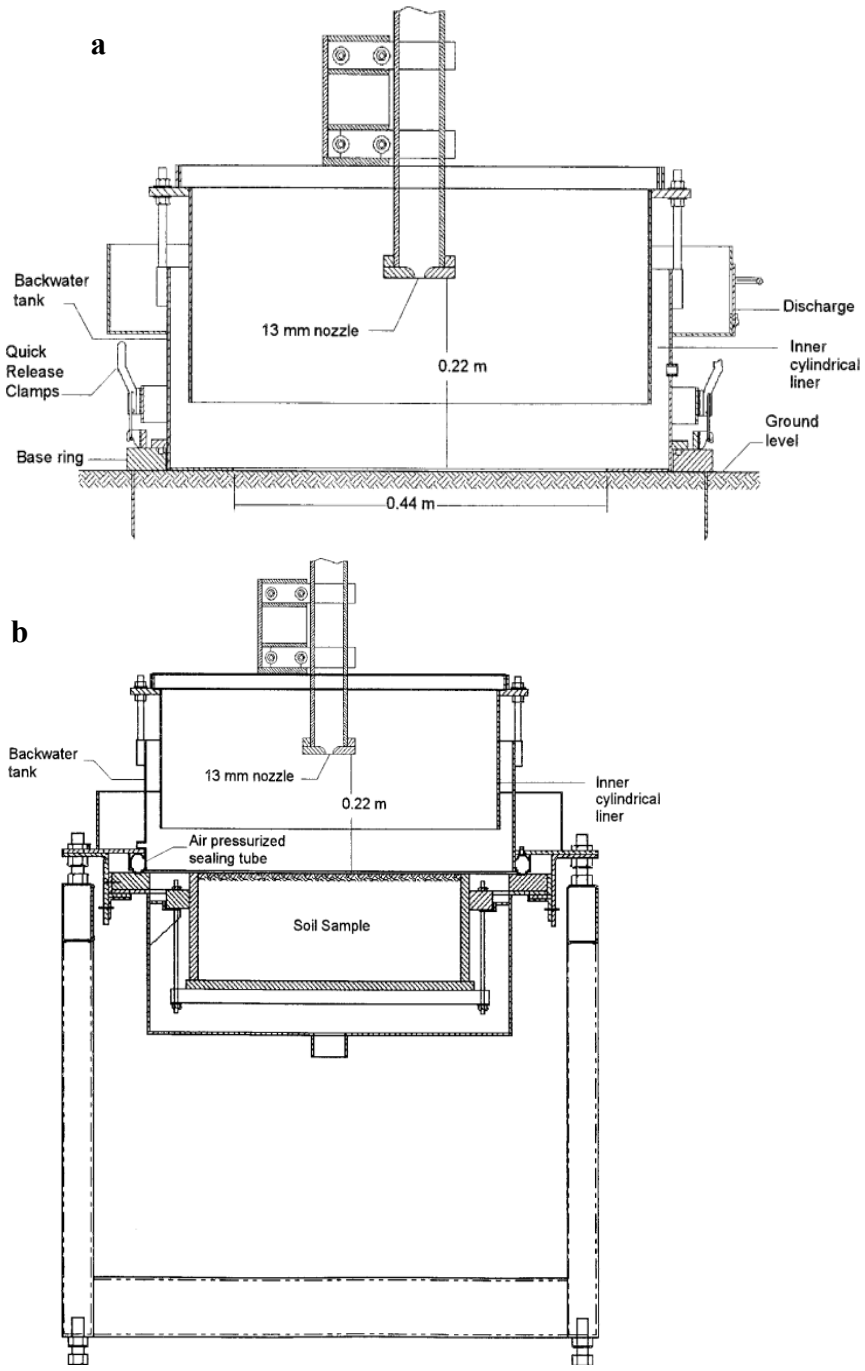

Figure 8 (a) Jet Erosion Test apparatus for field testing, and **(b)** Jet Erosion Test apparatus for laboratory testing (Hanson and Cook, 2004)

2.6.3 Hole Erosion Test (HET)

The most widely known device for testing internal erosion is the Hole Erosion Test (HET). This test was developed by Wan and Fell (2002) to study the erosion characteristics of soil in earthen embankment dams and levees, specifically the internal piping mechanisms. This method estimates the critical shear stress that is needed to initiate erosion and the associated erosion rate to determine the erodibility parameters of the soil. Figure 9 shows the original schematic of the Hole Erosion Test apparatus designed by Wan and Fell (2002). Note that more background for the HET is given here as this is the test method chosen for this study.

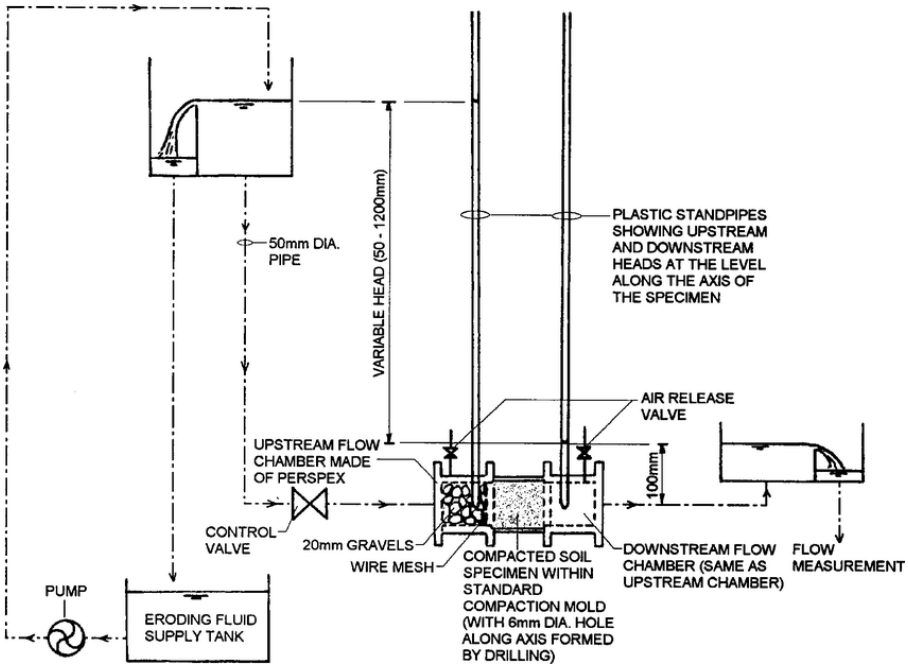

Figure 9 Hole erosion test (HET) apparatus from Wan and Fell (2002)

For the HET, the sample is prepared by using a standard proctor mold and compacting the sample. Then, a 6 mm-diameter hole is drilled in the center of the sample along the longitudinal axis to simulate a concentrated leak or pipe. The downstream head is then set to 100 mm. The flow rate measured during the test is used for the indirect measurement of the diameter of the preformed hole and the hydraulic shear stress, τ_t, can be calculated using the following equation:

$$\tau_t = \rho_w g s_t \frac{\varphi_t}{4} \tag{1}$$

where s_t = hydraulic gradient across the specimen at time t, and φ_t = diameter of the axial hole at time t. The rate of erosion can be found using:

$$\dot{\varepsilon}_t = \frac{\rho_d}{2} \frac{d\varphi_t}{dt} \tag{2}$$

And the diameter can then be found for laminar flow:

$$\varphi_t = \left(\frac{16 Q_t f_{Lt}}{\pi \rho_w g s_t}\right)^{1/3} \quad (3)$$

Or for turbulent flow:

$$\varphi_t = \left(\frac{64 {Q_t}^2 f_{Tt}}{\pi^2 \rho_w g s_t}\right)^{1/5} \quad (4)$$

where f_{Lt} and f_{Tt} are friction factors and are assumed to vary linearly with time between their initial and final values. When the rate of erosion is plotted against the hydraulic shear stress along the axial hole, the rising portion of the plot can be approximated by fitting a straight line which then has the slope equal to C_e.

The erodibility of a soil can be described in terms of behavior in two aspects: the rate of erosion at an applied known hydraulic shear stress and the ease of initiating erosion in a soil. The relationship between the rate of erosion and the applied hydraulic shear stress has been found to be linear (approximately) and can be expressed as

$$\dot{\varepsilon}_t = C_e(\tau_t - \tau_c) \quad (5)$$

where $\dot{\varepsilon}_t$ = rate of erosion per unit surface area of the slot/hole at time t (kg/s/m2); C_e= proportionality constant named by the writers as the coefficient of soil erosion (s/m); τ_t= hydraulic shear stress along the slot/hole at time t (N/m^2); τ_c= critical shear stress (N/m^2). The critical shear stress τ_c is found by extrapolating the rate of erosion versus hydraulic shear stress to zero. From this, the critical shear stress corresponds to the minimum head at which erosion is first initiated which is then defined as the initial shear stress, τ_o. The value C_e is a small number ranging from 10^{-1} to 10^{-6} and can therefore be expressed by the Erosion Rate Index (I) which ranges from 0 to 6:

$$I = -\log(C_e) \quad (6)$$

The HET was designed such that the Erosion rate index is classified into 6 categories as shown in Table 2.

Table 2 Erosion rate index classification for HET (Wan and Fell, 2004)

Group Number	Erosion rate index	Description
1	<2	Extremely rapid
2	2-3	Rapid
3	3-4	Moderately rapid
4	4-5	Moderately slow
5	5-6	Very slow
6	>6	Extremely slow

2.6.4 Hole Erosion Test Modifications and Developments

The HET apparatus has been modified and adapted several times since the original design by Wan and Fell (2002). These developments have aimed to address several issues and criticisms of the HET apparatus. One of the main factors is that during the HET, the sample cannot be viewed which means that the test is performed without knowing what is happening to the sample. Another issue, first explained by Luthi et al. (2011), is that the values of critical shear stress may be overestimated due to the hydraulic head difference, Δh, not accurately representing the total energy head loss. The argument made is that the sidewall pressure measurements are not accurate as the sudden expansion from the sample creates a flow recirculation and a drop in hydraulic head. Another issue is that the high velocity jet exit from the sample may be significantly greater than the upstream head measurement.

A modified version of the Hole Erosion Test apparatus (HET-P) was designed, incorporating a Pitot-static tube at the downstream side of the sample to measure the total energy head and the velocity head of the jet as it exits the sample to avoid the issues mentioned previously (Figure 10). With the Pitot-static tube incorporated, the HET-P did measure a more accurate head differential and the hydraulic shear stress values were significantly less compared to the HET.

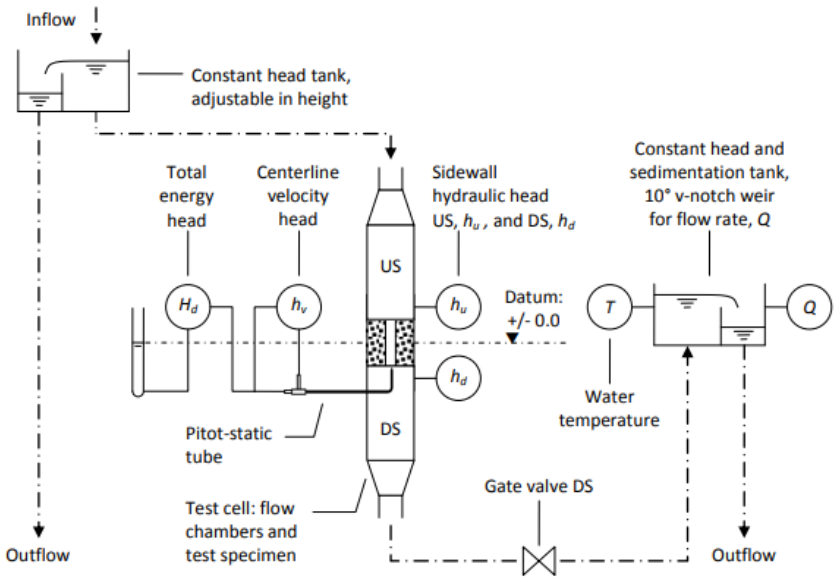

Figure 10 Modified Hole Erosion Test (Luthi, 2012)

2.7 Linking Geophysical Methods and Soil Erosion

Geophysical methods have also been used for estimation of surface soil erodibility (e.g., bridge scouring and levee overtopping). Fundamentally, the erodibility of a material can be represented by the relationship between the erosion rate (ż) in depth/time and the shear stress (τ) at the particle interface (National Academies of Sciences, 2019). Briaud (2008) introduced an erodibility categories classification system in the form of erosion rate versus velocity or erosion rate versus shear stress. This system is primarily based on extensive Erosion Function Apparatus (EFA) testing on a wide range of soil types. The erodibility category of a material is determined by plotting the erosion function of the material on the erosion category chart. Later work added USCS soil types to the erosion category chart (Figure 11). The width of each USCS soil type represents the zone that 90 percent of samples tested, for a given soil type, using EFA plotted on the erosion category chart (National Academies of Sciences (NAS), 2019). Although the erosion categories provide insight into the erodibility of a material, the erosion category is not adequate for design purposes (NAS, 2019).

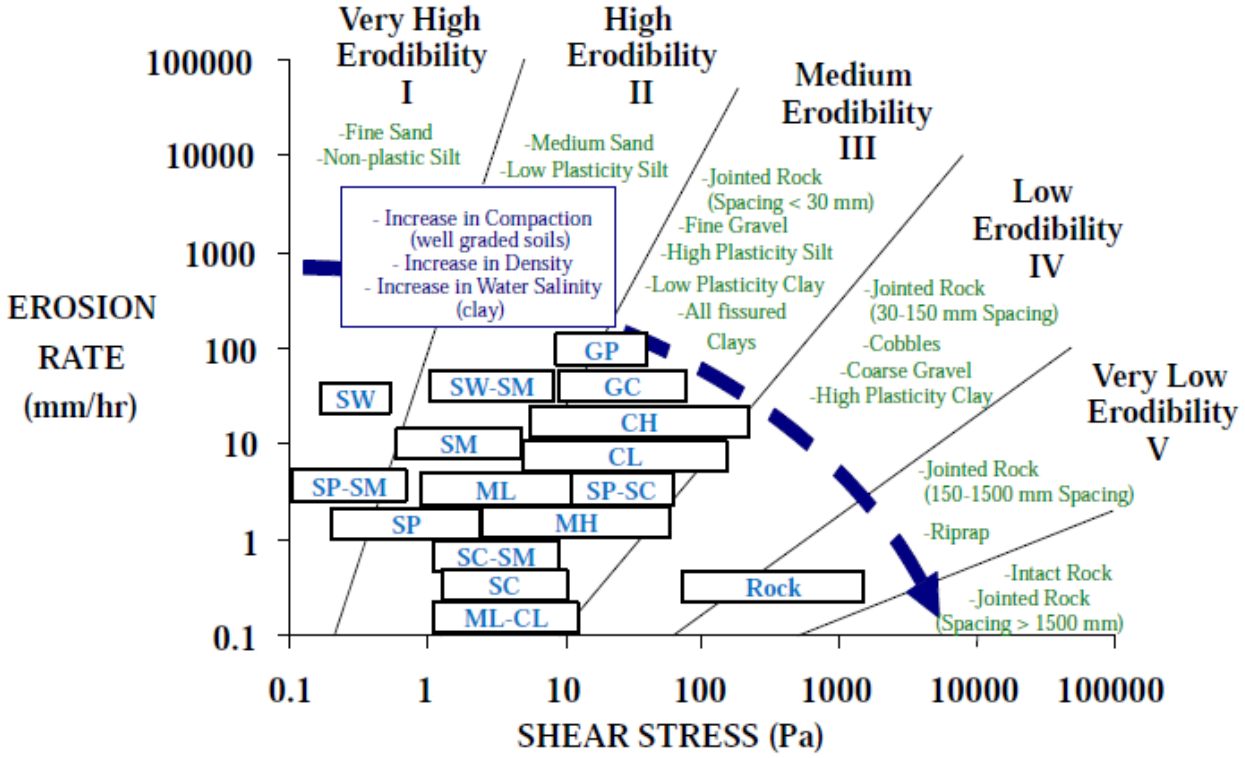

Figure 11 Erodibility Category Charts of Shear Stress (Pa) versus Erosion Rate (mm/hr) with USCS soil types (National Academies of Sciences, 2019)

Commonly measured soil properties that influence soil erodibility, as complied by NAS (2019), include plasticity index, liquidity index, unit weight, water content, undrained shear strength, fines content, soil gradation, median grain size, coefficient of uniformity, percent compaction of fills, soil swell potential and soil void ratio. Soil properties that influence erodibility also influence geophysical properties, such as ER and seismic velocities. For example, several factors influencing

both erodibility and ER of soils include unit weight, percent compaction of compacted soils, particle size distribution, median grain size, mineralogy, pore-water composition, and saturation level (Abu-Hassanein et al., 1996; Mofarraj Kouchaki et al., 2019; NAS, 2019; Rein et al., 2004; Samouëlian et al., 2005; Tucker-Kulesza et al., 2019).

Tucker-Kulesza et al. (2019) used 2-D ERT to estimate the erosion potential due to scouring of 15 bridge sites in Kansas. A 2-D ERT survey was completed at each site, and a continuously sampled boring was advanced. The collected samples were used for laboratory analysis, including erodibility classification using the Kansas State University-EFA and erosion categories (from Briaud, 2008), water content, percent fines, median grain size, and USCS soil classification. Using statistical analysis, Tucker-Kulesza et al. (2019) determined that field-measured ER values over 50 Ω-m had a 93 percent probability of classifying as high erodibility. According to Tucker-Kulesza et al. (2019), the samples collected may not be representative of saturated soils; however, the results have the potential to identify soils highly susceptible to scouring erosion on the near surface of levees.

While extensive research has been performed on the geophysical assessment of levees, less research has been applied directly to the assessment of zones of heavy internal erosion damage in levees. Additionally, much of the existing research assessing internal erosion damage with electrical and seismic methods utilizes limited transverse geophysical surveys. This study utilizes extensive perpendicular longitudinal and transverse DC ERT lines complemented by MASW and CCR surveys. The combination of geophysical methods applied to the project site provides further insight into the geophysical signature of internal erosion damage in levees. Geophysical assessment of internal erosion damage in levees offers the potential to more effectively detect and repair zones of internal erosion damage than conventional visual methods.

Laboratory estimates of soil erodibility and electrical resistivity were also measured and compared to create a relationship that can be used to estimate and predict erosion potential based on soil type and condition as determined by the field geophysical testing.

3 Methodological Approach

3.1 Background of the Project Site

The project site is located on the Crawford County Levee District (CCLD) levee segment, downstream of Van Buren, Arkansas, on the Arkansas River from levee stations (STA) 686+00 to 735+00 (Figure 12). The CCLD levee segment is part of the Van Buren Levee District No. 1/Crawford County Levee System. The city of Van Buren is responsible for the levee and floodwalls adjacent to the Arkansas River in Van Buren, AR, and the CCLD is responsible for the remaining earthen levee segment downstream of Van Buren (National Levee Database (NLD), 2020). The CCLD levee segment (referred to as the levee hereafter) consists of 19.7 miles of earthen levee on the left descending bank of the Arkansas River with an average height of 15 ft, crown width of 10 ft, and 1 Vertical: 3 Horizontal riverside and landside slopes (NLD, 2020). Construction began on the levee in 1947 and was completed in 1950, with a partial setback levee constructed from 1953 to 1954 (NLD, 2020). In 2009, the levee was certified by the Federal Emergency Management Agency (FEMA) to protect against the 100-year flood event following a levee certification study performed by Freese and Nichols, Inc. (NLD, 2020).

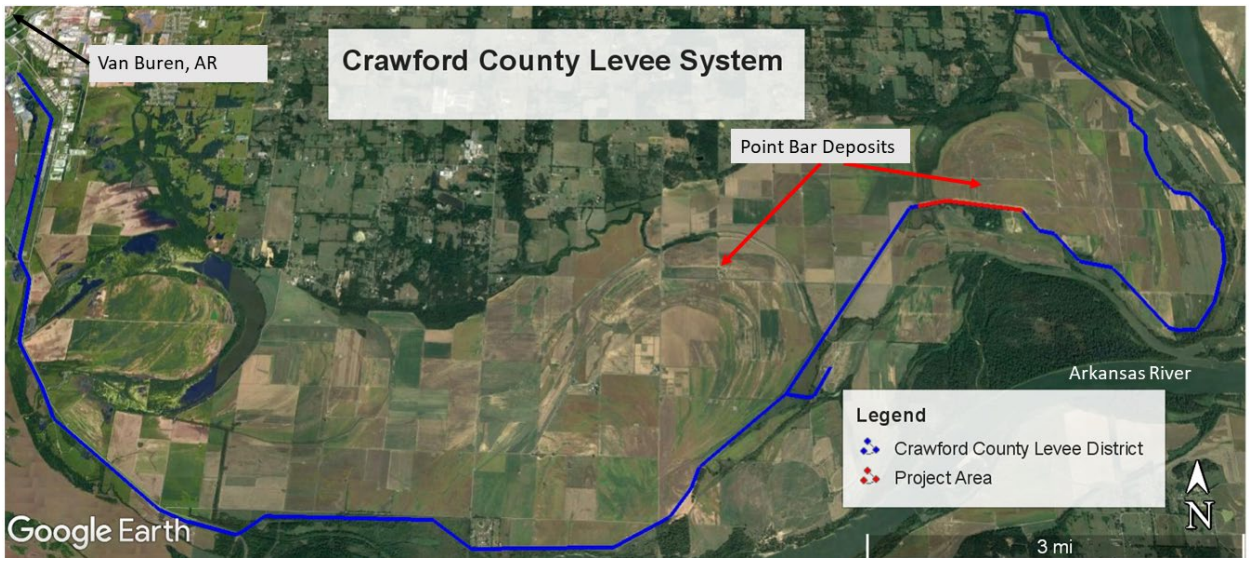

Figure 12 Project location (red) on the CCLD levee segment (blue) at coordinates of (35.399970, -94.178028)

The project site is located within the Arkansas River Valley, which is bound by the Boston Mountains to the north and the Ouachita Mountains to the south; in the Arkansas River Valley, discontinuous alluvial deposits consisting of flood-plain and terrace deposits overlying bedrock (Kresse et al., 2014). The groundwater in the alluvial deposits of the Arkansas River forms the Arkansas River Valley alluvial aquifer, which is an important water source for irrigation and municipal water supply (Kresse et al., 2015). These alluvial deposits underlie the CCLD levee segment and generally display a coarsening downward sequence with silts and clays at the surface, transitioning to sands and fine gravel at depth (Kresse et al., 2015). Kreese et al. (2015) investigated the lithology of the Arkansas River Alluvial aquifer downstream of Van Buren, AR,

including the project site location, finding that point bars deposits represented the most permeable deposits with the highest percent of sand found on the concave side of point bar deposits. Point bar deposits can easily be observed crossing the levee and the project site in satellite imagery (Figure 1). Point bars form through lateral accretion of coarse-grained sediments on the concave side (the inside bank) of a migrating meander, as a meander migrates abandoned point bar deposits are stacked laterally in deposits known as scroll bars, that are subsequently covered with overbank deposits (Bierman & Montgomery, 2014). Point bar deposits are characterized by an overall fining upwards and downstream in the deposits (Thomas et al., 1987). The surface expression of scroll bar deposits is characterized by a ridge and swale topography that is observable in both Light Detection and Ranging (LiDAR) imagery and in the distribution of vegetation (van de Lageweg et al., 2014). In ridge and swale topography, the ridges are formed by point bar deposits and the swales are depressions separating adjacent ridges. Swales are filled with fine-grained materials that may extend for meters into the subsurface and the distribution of ridges and swales is an important geological control of sand boils formation at levee sites (Strange et al., 2016).

Numerous historical boring logs exist for the CCLD levee segment that was advanced by the USACE during levee construction and design. Additionally, 28 borings were advanced through the levee crest by Freese and Nichols, Inc. during the 2009 levee certification. The levee certification study found that the soils in the levee body consist of mixtures of clay, silt, and sand (CL, ML, CL-ML, SC, and SM) with variable gravel content, and the foundation materials consist of silts, clays, and sands with increasing sand content with depth. The depth to bedrock at the site varies from 16.5 m to 18.6 m ft below the levee crest; however, only 7 of the 28 borings were advanced until bedrock was reached, with shale and sandstone bedrock encountered in these borings (USACE Little Rock District, personal communication, July 2021). Groundwater was encountered at 7 m to 12 m below the levee crest during the 2009 certification study drilling. The groundwater conditions at the site are uncertain; however, the Arkansas River Valley alluvial aquifer is generally unconfined with groundwater flowing toward the Arkansas River (Kresse et al., 2015).

The flooding on the Arkansas River from May to June of 2019 resulted in significant damage to five levees and breaches of three levees between Fort Smith, AR, and Little Rock, AR (Lewis & Trevisan, 2019). Locations in Kansas and Oklahoma within the Arkansas River Basin received over 20 inches of rain in May of 2019 alone, producing a peak flow with a 200-year recurrence interval for the Arkansas River near Van Buren, AR (USGS stream gage No. 07250550) (Lewis & Trevisan, 2019). On the CCLD levee segment, the 2019 flooding resulted in several areas of internal erosion damage, identified by sand boil activity and a slope stability failure (USACE Little Rock District, personal communication, July 2021). The levee is currently (as of December of 2022) active in the USACE Rehabilitation and Inspection Program (RIP), and repairs were recently completed, including the installation of a seepage berm and repair of two slope stability failures under Public Law (PL) 84-99.

The project area was selected to investigate a section of the levee that experienced a slope stability failure (35.399970, -94.178028) and extensive sand boil formation during the 2019 flooding. On the initial site visit on June 16, 2021, the slope stability failure (35.399970, -94.178028) (Figure 2c) that formed during the 2019 flooding had been repaired (this slide will be referred to as the 2019 slide hereafter); however, a second slope stability failure (35.400050, -94.178713) (Figure 2a) was present approximately 110m to the west of the 2019 slide (this slide will be referred to as the 2021 slide hereafter). It is unknown exactly when the 2021 slide initiated; the formation of the slide occurred between the 2019 flooding and the initial site visit on June 16, 2021. The project site is approximately 1530 meters in length, with geophysical surveys performed longitudinally along the levee crest and landside toe, and transverse to the levee. The project site extends approximately from CCLD STA 686+00 to STA 735+00, with an existing landside seepage berm present from STA 686+00 to STA 704+00 and a recently constructed landside seepage berm from STA 703+00 to STA 735+00 (Figure 13d). Notably, the construction of the new seepage berm was ongoing throughout much of the fieldwork, and the construction process must be considered when interpreting subsequent geophysical surveys in the construction area. The project site is divided based on the two main areas of geophysical testing, which will be referred to as the internal erosion area and the control area. The internal erosion area encompasses the area of the slope stability failures and heavy sand boil activity (Figure 13a,b,c). The control area is located at the western end of the new seepage berm, where no significant damage occurred during the 2019 flooding (Figure 13d).

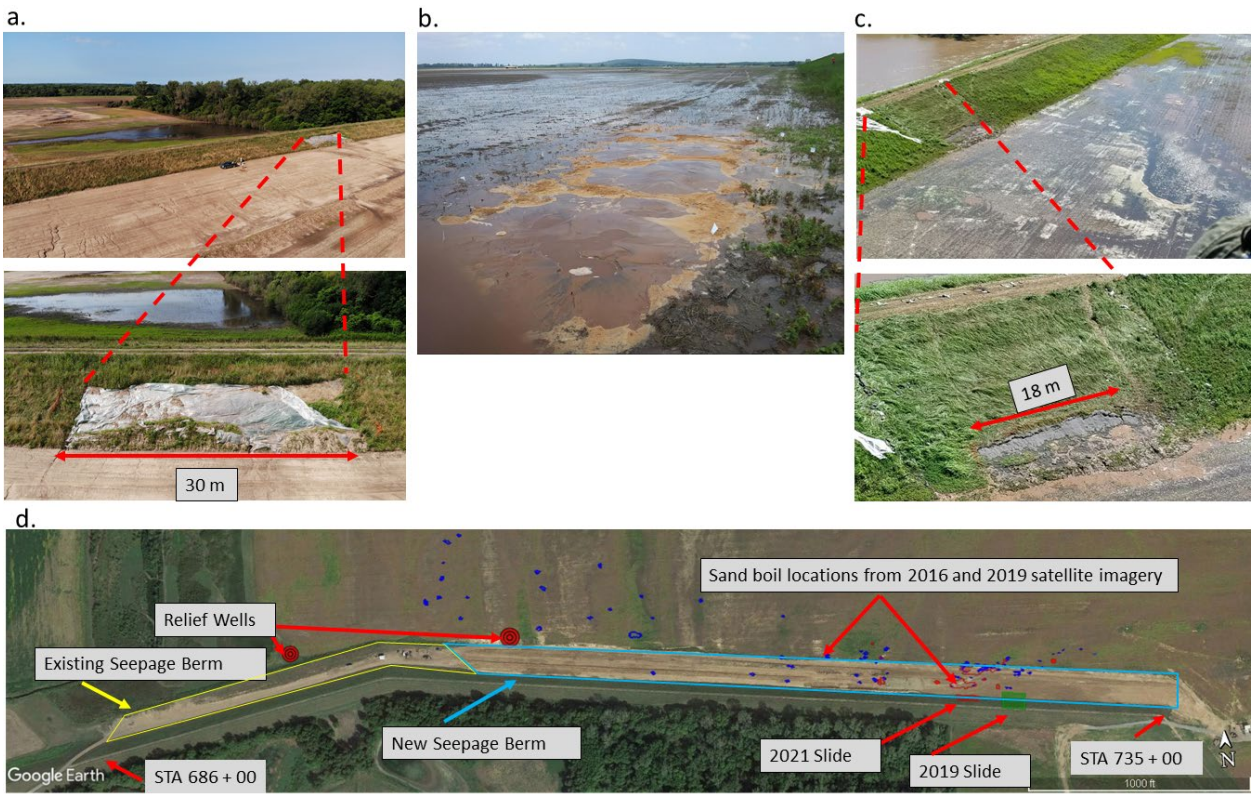

Figure 13 Project site on the CCLD levee segment showing a) the 2021 slide b) sand boils on the landside of the levee in June of 2019 during the flooding and near the 2021 slide (USACE Little Rock District, personal communication, July 2021) c) the 2019 slide (USACE Little Rock District, personal communication, July 2021) d) overview of the project site with sand boil, slide, relief well, and seepage berm locations identified on satellite imagery from 2021

On June 24, 2019, the Arkansas Forestry Commission identified a landslide (the 2019 slide) and sand boil activity at the project site (USACE Little Rock District, personal communication, July 2021). In the internal erosion area, the USACE observed numerous sand boils over 2.5 m in diameter and at distances of up to 30 m from the levee. Flood-fighting efforts included the placement of 0.3 m of gravel at the base of the 2019 slide for slope stabilization and to act as a filtered exit (Figure 14). The gravel placement on the 2019 slide successfully prevented any further slope displacement. It is unknown to what extent the gravel placed to stabilize the 2019 slide is present following the repair of the levee and seepage berm construction. The potential presence of this gravel must be considered when interpreting geophysical data collected in the 2019 slide area. The USACE attributed the 2019 slope failure to the increased height of the levee in the area and the presence of pervious foundation materials (USACE Little Rock District, personal communication, July 2021). The new seepage berm has a design width of 46 m with a 1.5 m thickness at the levee toe and thinning to 0.6 m away from the levee (USACE Little Rock District, personal communication, July 2021).

Figure 14 Placement of gravel at the base of the 2019 slide on June 25, 2019 (USACE, 2019)

3.2 Geophysical Testing

Geophysical surveys, including CCR, DC ERT, and MASW, were performed to assess internal erosion damage at the project site on the CCLD levee segment. The geophysical surveys were acquired from June 2021 to April 2022; surveys included CCR, DC ERT, and MASW along the levee crest and landside toe. Additionally, transverse DC ERT surveys were performed at select locations. The geophysical surveys are concentrated in two areas, including the internal erosion and control areas, as described in the preceding section (Figure 15). Geophysical testing outside the control and internal erosion areas included two transverse DC ERT lines, one landside longitudinal DC ERT line, and CCR lines along the entire crest and landside of the project area. The survey locations and data processing for each geophysical method are detailed in the following sections.

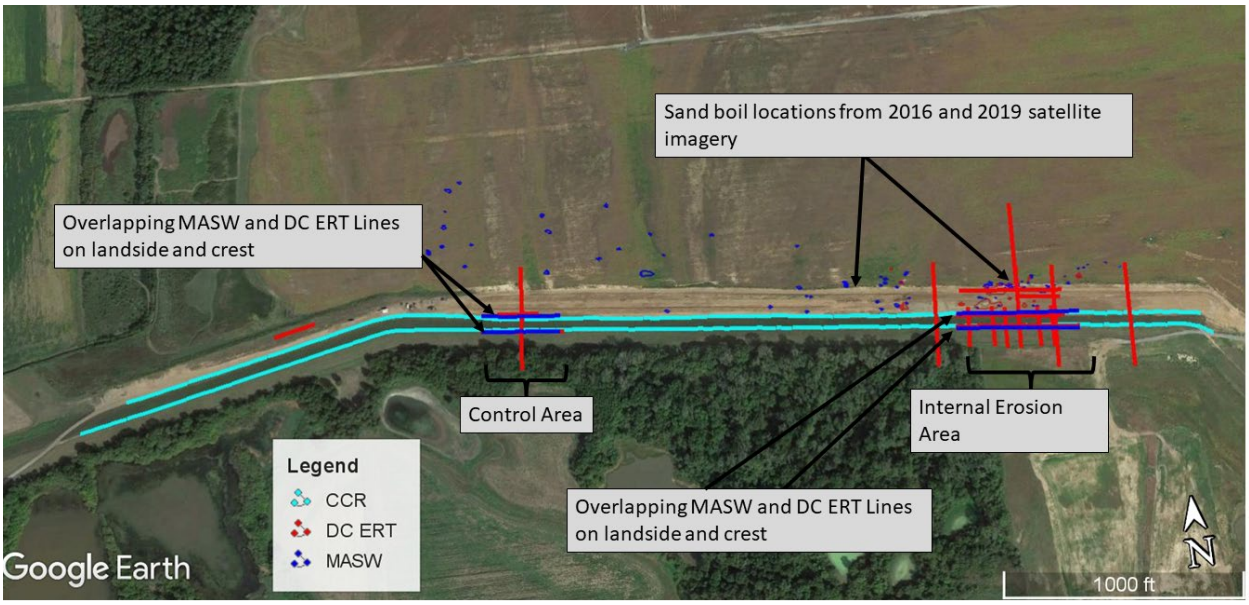

Figure 15 Overview of geophysical testing at the project site

3.2.1 Multichannel Analysis of Surface Waves (MASW)

Multichannel analysis of surface waves (MASW) using Rayleigh-type surface waves was performed at parallel crest and landslide lines in the internal erosion and control areas on September 24, 2021 (Figure 16). MASW Line A and Line C are 172.5 m long and are located on the landside toe and crest of the internal erosion area, respectively. MASW Line B and Line D are 115 m long and are located on the control area landside toe and crest, respectively.

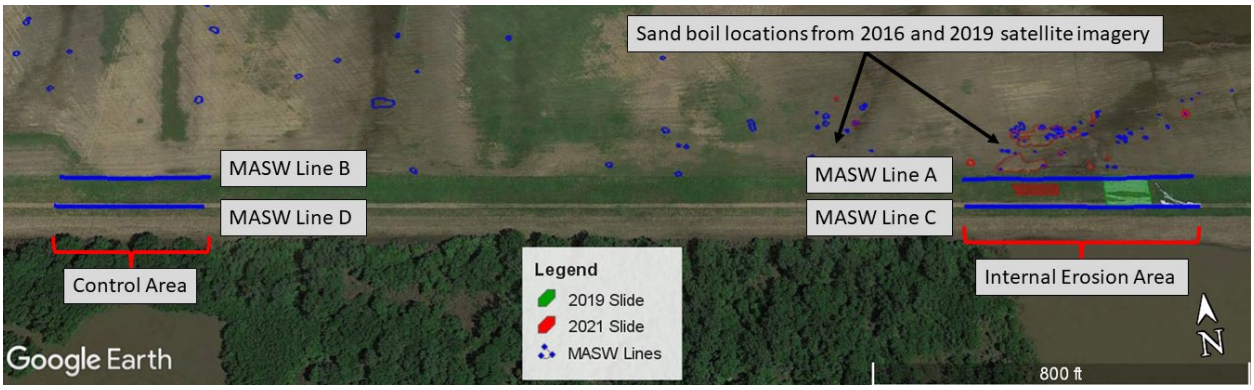

Figure 16 Layout of MASW surveys at the project site

The MASW data was acquired using a landstreamer system with 24, 4.5 Hz, vertical geophones, and a uniform geophone spacing of 1 m (Figure 17a). Seismic records were recorded using a Geometrics Geode seismograph. The landstreamer system relies on pressure coupling of geophones to the ground surface using weighted sleds, which allows the geophone array to be dragged along the survey line and significantly increases survey efficiency over staked arrays. Vertical blows from a 12 lb sledgehammer source were used to generate Rayleigh waves at multiple source offsets, including +10 m, +5m, +1m (i.e., off the far end (geophone 24) of the

array), the array midpoint, and -1m (i.e., off the near side (geophone 1) of the array) for each landstreamer setup. Three sledgehammer blows were stacked for each source location to increase the signal-to-noise ratio (Figure 17b). The landstreamer data acquisition process starts with the midpoint of the geophone array at the start of the survey line. The seismic data is then recorded for each source offset. The array is then dragged, shifting the midpoint of the array by a set interval, and the data acquisition process is repeated. This overall process is repeated until the survey line is covered. For this project, the midpoint of the geophone array was shifted by 11.5 m or half an array length between array setups. The location of the array midpoint for each landstreamer setup was recorded using a Trimble Geo 7x centimeter GPS. Fifteen landstreamer setups were required for the 172.5 m internal erosion area crest and landslide MASW lines, and ten landstreamer setups were required for the 115 m control area MASW lines (Figure 16). Horizontal to vertical spectral ratio (HVSR) tests were performed at one crest location and one landside location for use in the joint inversion of the Rayleigh wave data. Horizontal to vertical spectral ratio tests were performed with a minimum record length of 20 minutes using a Nanometrics Trillium Compact seismometer and the Nanometrics Centaur Digitizer.

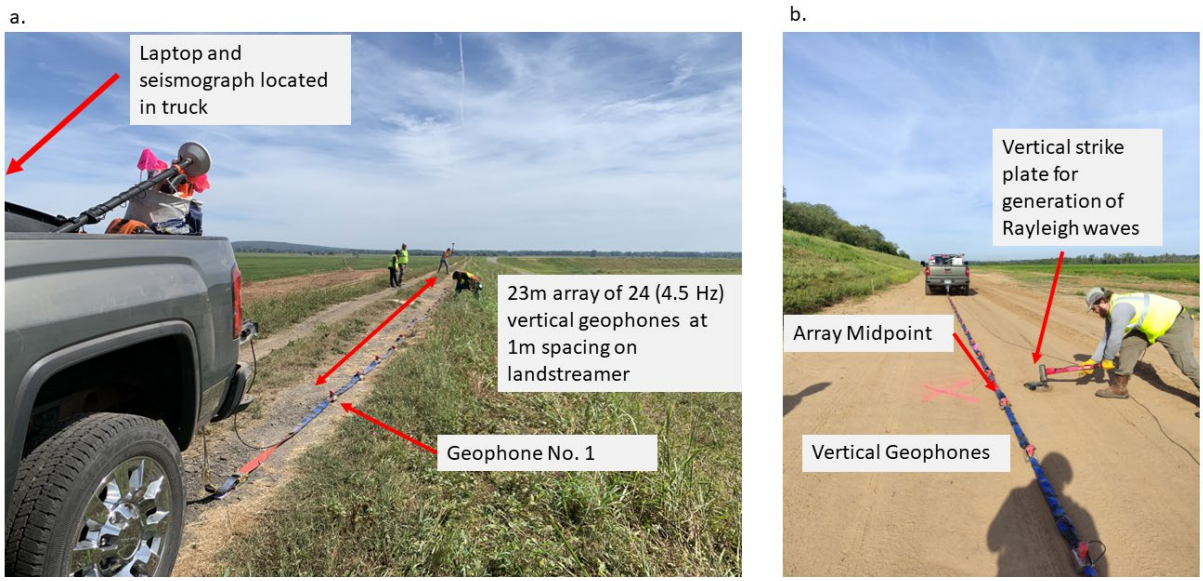

Figure 17 Landstreamer acquisition of Rayleigh type surface wave data at the project site a) landstreamer acquisition geometry b) mid-array shot point with vertical sledgehammer blows for Rayleigh wave generation

For each MASW setup, the experimental MASW data (i.e., the collected field data) was processed in MATLAB using the frequency domain beamformer method (FDBF) to transform the data from the time domain into the frequency domain for each source offset (Zywicki, 1999). The use of multiple source offsets aid in the identification of higher modes, identification of near-field and far-field effects and provides an estimate of the uncertainty in the dispersion data (Cox & Wood, 2011). The maximum spectral peak was automatically picked in the velocity-frequency spectra of each source offset for each frequency to reduce operator bias (Cox & Wood, 2011) (Figure 18a). The maximum spectral peak (i.e., the dispersion curve) for each offset was then combined to form a composite dispersion curve for each landstreamer setup. The composite dispersion curves were

divided into 100 frequency bins on a log distribution from 1 to 200 Hz to calculate the mean dispersion curve and associated standard deviation (Figure 18b). All MASW data for this site was inverted using only the fundamental mode. The composite dispersion curves for each setup were cut to remove higher modes, near-field effects, and noise; however, the normal scatter in the dispersion curves was left to preserve the uncertainty in the dispersion data (Cox & Wood, 2011). An example of the cutting process for Setup 3 on MASW Line A to isolate the fundamental mode is presented in Figures 18b and 18c. It can be observed in the -1 m source offset velocity spectra (Figure 18a) that the fundamental mode is followed from approximately 8 Hz to 75 Hz before jumping to a higher mode. Additionally, near field effects can be observed in the steep take off in the +1 m offset and -1 m source offset dispersion curves at low frequencies.

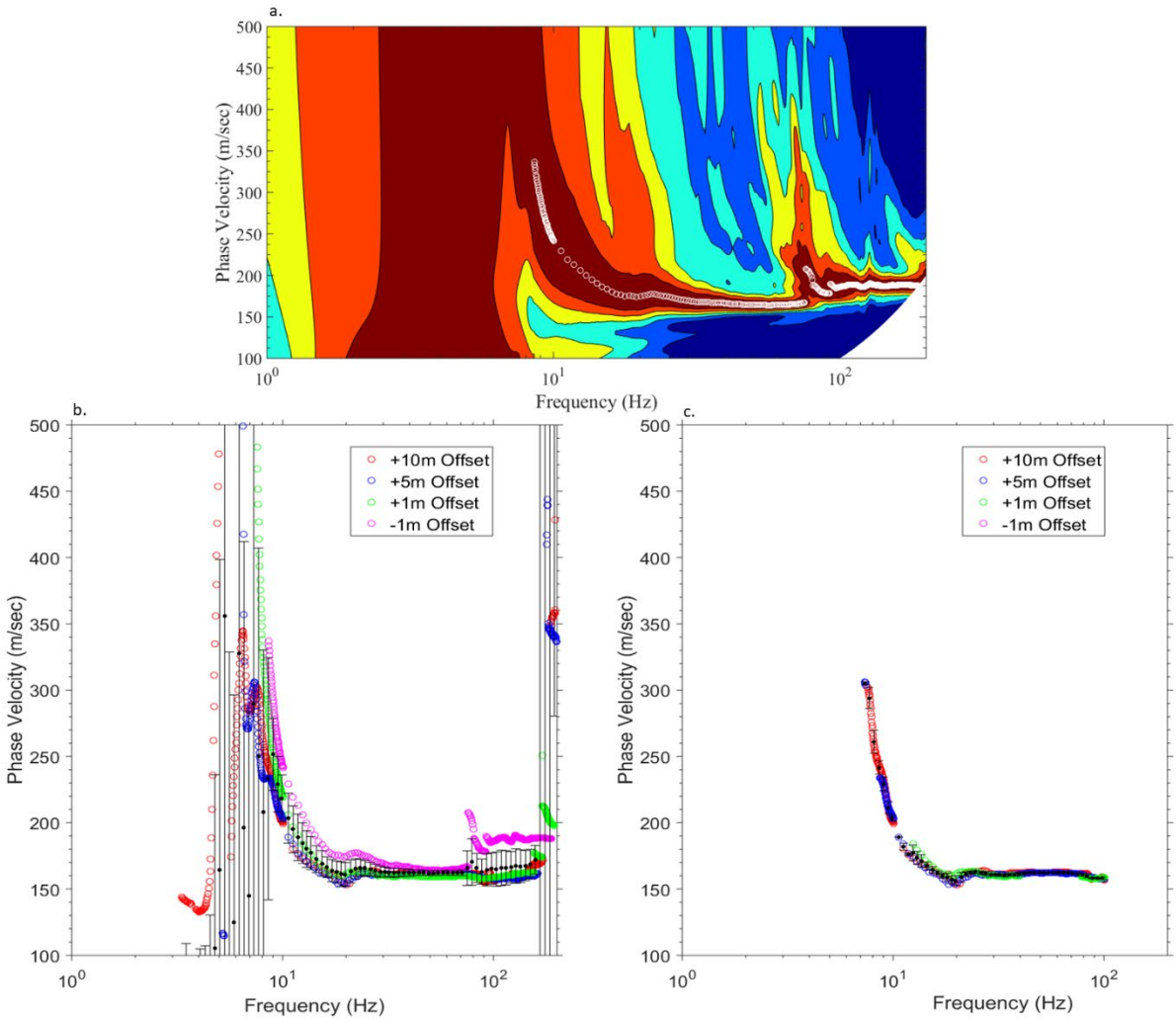

Figure 18 Composite dispersion curve cutting process for Setup 3 on MASW Line A a) automatic picking of the maximum spectral peak for each frequency for the -1 m source offset b) composite dispersion curve from multiple source offsets, with mean dispersion curve and associated standard deviation shown (for each frequency bin) c) final dispersion curve after the cutting process

After the dispersion curve cutting process was completed, the composite dispersion curves for each MASW setup were inverted in dinver within the Geopsy software package (Wathelet, 2008).

Dinver provides a graphical user interface for the inversion of surface wave data to estimate the 1-D Vs profile that resulted in the experimental dispersion curve. In dinver, multiple parameters are input to constrain the inversion, including ranges of Vs, Vp, layer thicknesses, and Poisson's ratio. A joint inversion of the MASW data and the frequency of the HVSR peaks was performed in Geopsy with weighting factors of 0.8 and 0.2, respectively. The joint inversion of MASW data and the HVSR peaks allowed for greater constraint of the inversions at depth, as there is limited low frequency content when using a sledgehammer source. A minimum of 100,000 models were searched using the neighborhood algorithm in Geopsy for the dispersion curve of each MASW setup. In the inversion process, Vs models are searched to minimize the misfit between the theoretical dispersion curve (i.e., the dispersion curve resulting from a Vs model) and the experimental dispersion curve. Multiple parameterizations (e.g., layer thickness, number of layers, and layer velocity ranges) were explored to fit the experimental dispersion data. A parameterization of 9 to 11 layers with increasing layer thickness with depth and Vs ranging from 75 m/s to 1000 m/s was determined to best fit the experimental dispersion data. Water level measurements at the B-23 piezometer located in the internal erosion area were used to guide the Vp parameterization. The quality of the fit between the theoretical and experimental dispersion curves was judged on both the value of the misfit parameter and by visual comparison with the experimental dispersion curve. Visual comparison between the theoretical and experimental dispersion curves is necessary as the misfit parameter is not a physically meaningful parameter, and low values do not directly correlate to a high quality fit (Griffiths et al., 2016; Rahimi et al., 2018). This comparison was made on the level of dispersion curves and the 1-D Vs profiles resulting from the inversion process. For example, profiles of Vs versus pseudo depth (approximated as wavelength/2 of the experimental dispersion data) were plotted to ensure that any low velocity zones (LVZ) in the resulting 1-D Vs profiles correlated to velocity inversions in the experimental dispersion curves. The 1-D Vs profile of each MASW setup was taken as the median Vs profile of the 1000 lowest misfit profiles (Figure 19). It can be observed that there is more uncertainty in the Vs profiles with depth; this is likely due to a loss resolution with depth and the limited low frequency content of the sledgehammer source. The individual 1-D Vs profiles from each MASW setup were combined into pseudo 2-D Vs cross-sections. The pseudo 2-D Vs cross-sections for each MASW line were produced using triangulation with linear interpolation between the 1-D Vs profiles in the Surfer 14 program from Golden Software.

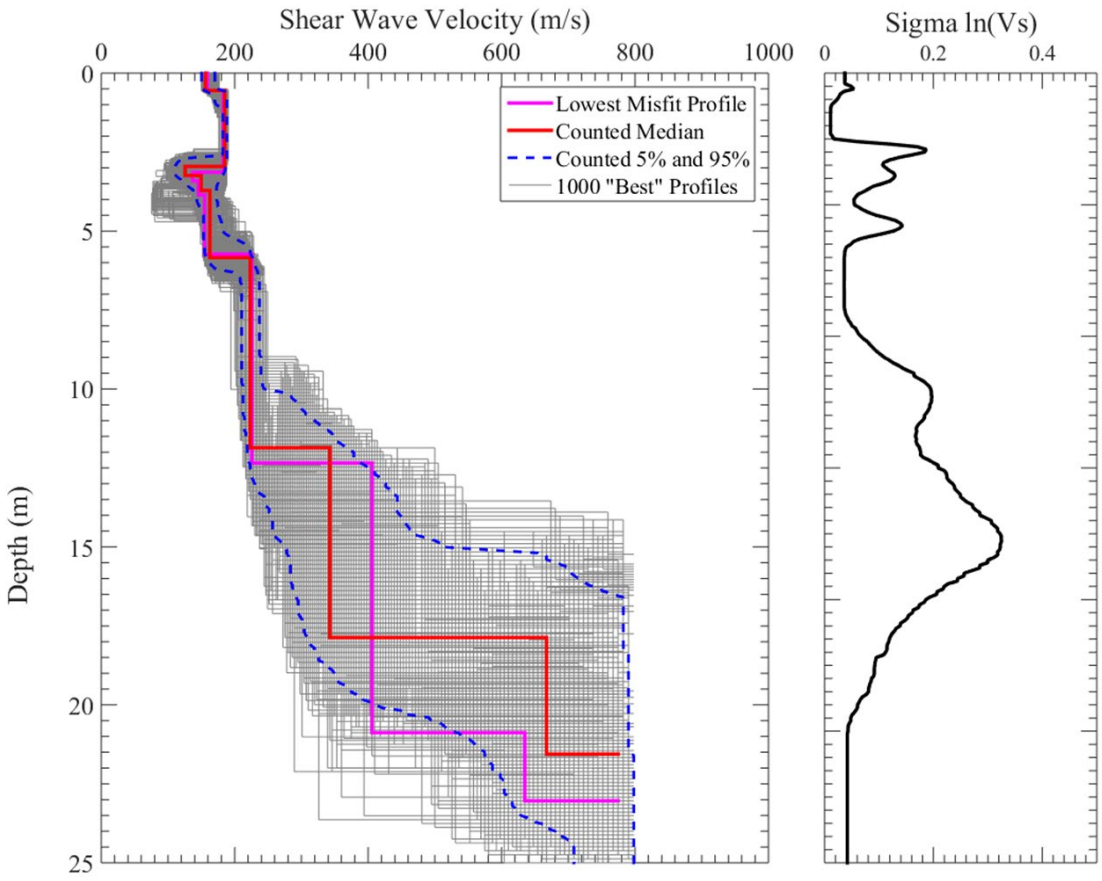

Figure 19 The 1000 lowest misfit profiles from the inversion process and standard deviation (blue) for MASW Line A Setup 3. The counted median shown in red is used as the 1-D Vs profile for each MASW setup

3.2.2 DC Electrical Resistivity Tomography

A total of 21 DC ERT surveys were performed at the project site from June 2021 to April 2022. Survey information for each DC ERT survey, including date, location, and array geometry, is presented in Table 3. All DC ERT lines were collected from riverside to landside for transverse lines (i.e., electrode 1 starts on the riverside of the levee) and from east to west for longitudinal line. Seven transverse DC ERT lines were surveyed in the internal erosion area, including VBL7, VBL7B, VBL8, VBL9, VBL12, VBL13, VBL15, and VBL19 (Figure 20). Additionally, six longitudinal lines were surveyed, including the crest line VBL5 and five landside lines. The longitudinal landside lines included lines near the levee toe on the seepage berm VBL1, VBL6, and VBL14, and lines at a distance from the levee, including VBL2 and VBL16 (Figure 20). Line VBL6 was located to overlap with VBL1 and VBL6 and allow for observation of temporal changes at the survey location. Two additional DC ERT lines, VBL17 and VBL18, were collected to the east and west of the internal erosion area, respectively (Figure 20). VBL17 and VBL18 were collected along transverse sections without significant sand boil activity.

A total of four DC ERT surveys were performed in the control area, including two overlapping transverse lines, VBL11 and VBL11B, a longitudinal crest line, VBL10, and a longitudinal

landside line, VBL3 (Figure 21). VBL11B was located as an extension of VBL11 and for observation of temporal changes in the control area. An additional longitudinal landside DC ERT line (VBL4) was collected approximately 210 m west of the control area on the outside edge of the existing seepage berm, as measured along the levee crest.

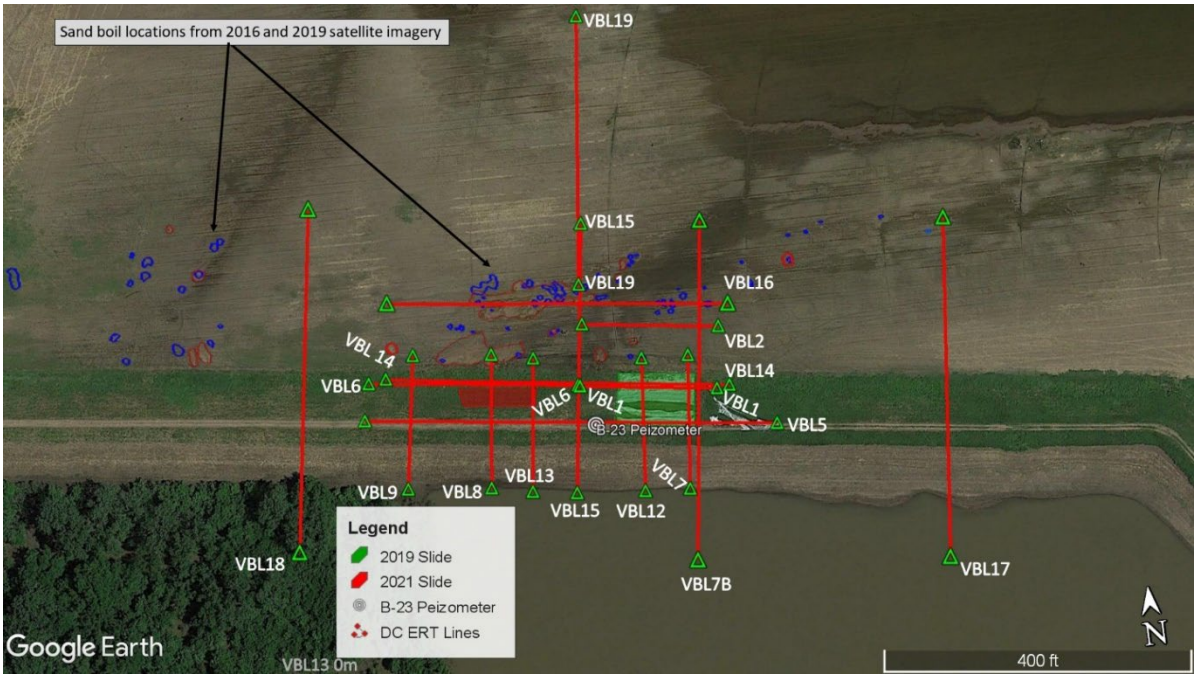

Figure 20 Internal Erosion area DC ERT Lines

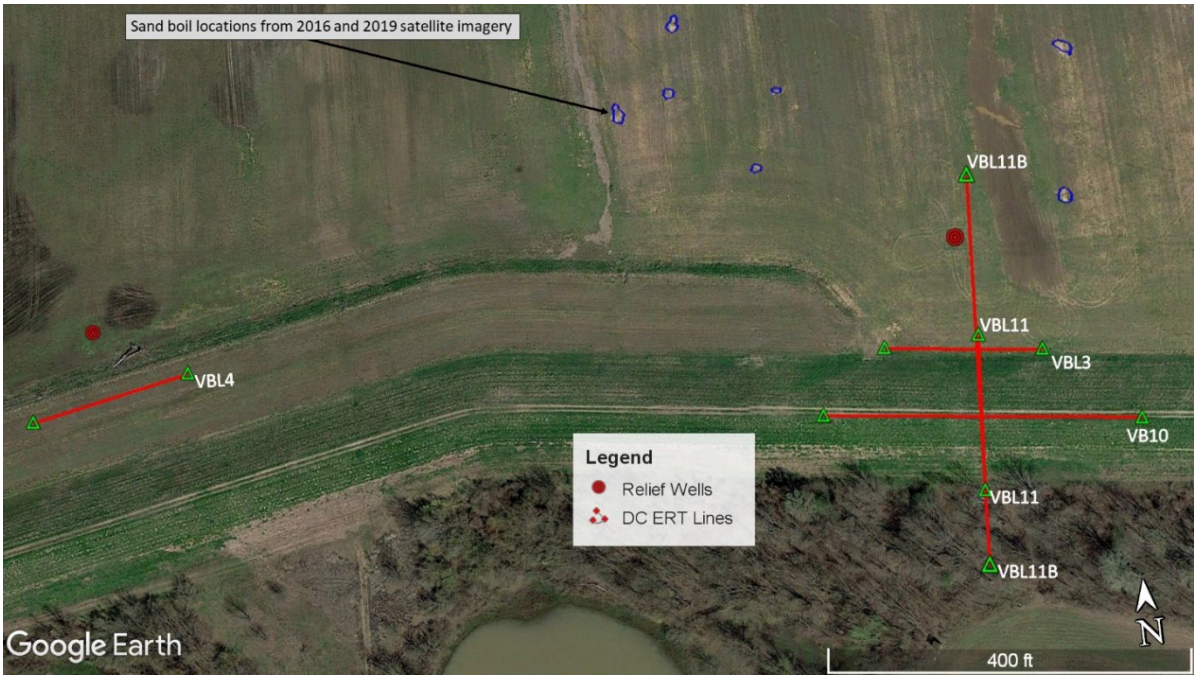

Figure 21 Control area DC ERT lines

Table 3 DC ERT survey geometry

Line ID	Location	Survey Length (m)	Electrode Spacing (m)	Line Orientation	Date Collected and Day No.
Internal Erosion Area DC ERT Lines					
VBL7	Internal Erosion Area	55	1	Transverse	7/15/2021 – Day 2
VBL7B	Internal Erosion Area	137.5	2.5	Transverse	1/11/2022 – Day 6
VBL8	Internal Erosion Area	55	1	Transverse	7/15/2021 – Day 2
VBL9	Internal Erosion Area	55	1	Transverse	7/15/2021 – Day 2
VBL12	Internal Erosion Area	55	1	Transverse	12/1/2021 – Day 5
VBL13	Internal Erosion Area	55	1	Transverse	12/1/2021 – Day 5
VBL15	Internal Erosion Area	110	2	Transverse	12/1/2021 – Day 5
VBL19	Internal Erosion Area	110	2	Transverse	4/8/2022 – Day 8
Landside					
VBL1	Internal Erosion Area	55	1	Longitudinal	6/23/2021 – Day 1
VBL2	Internal Erosion Area	55	1	Longitudinal	6/23/2021 – Day 1
VBL6	Internal Erosion Area	83	1	Longitudinal	7/15/2021 – Day 2
VBL14	Internal Erosion Area	138	2	Longitudinal	12/1/2021 – Day 5
VBL16	Internal Erosion Area	137.5	2.5	Longitudinal	1/28/2022 – Day 7
Crest					
VBL5	Internal Erosion Area	165	3	Longitudinal	6/23/2021 – Day 1
Control Area DC ERT Lines					
VBL11	Control Area	55	1	Transverse	9/1/2021 – Day 3
VBL11B	Control Area	137.5	2.5	Transverse	1/28/2022 – Day 7
Crest					
VBL10	Control Area	110	2	Longitudinal	9/24/2021 – Day 4
Landside					
VBL3	Control Area	55	1	Longitudinal	6/23/2021 – Day 1
DC ERT Lines Outside of Control and Internal Erosion Areas					
VBL17	68 m East of Internal Erosion Area	137.5	2.5	Transverse	1/28/2022 – Day 7
VBL18	25 m West of Internal Erosion Area	137.5	2.5	Transverse	1/28/2022 – Day 7
Landside					
VBL4	210 m West of Control Area	55	1	Longitudinal	6/23/2021 – Day 1

All DC ERT surveys were performed using the AGI Supersting R8/IP Wifi resistivity meter with 56 stainless steel electrodes. The AGI Supersting R8/IP system is an eight-channel electrical resistivity system that can perform automated ER measurements using multiple array types. A combination of the D-D and the strong gradient array was used for this research, which combines the high horizontal resolution of the D-D array and the greater data coverage and high signal-to-noise ratio of the strong gradient array (Sean, 2019). Electrode spacings of 1 m, 2 m, 2.5 m, and 3 m were used for this research (Table 3). For the transverse DC ERT lines, the relative location of the electrodes was surveyed using a total station, and the GPS location of the line ends was surveyed using a Trimble Geo 7x centimeter GPS (Figure 22a, b). For the longitudinal surveys in low relief areas, the electrode elevations and positions were surveyed with the Trimble Geo 7x centimeter GPS (Figure 22c).

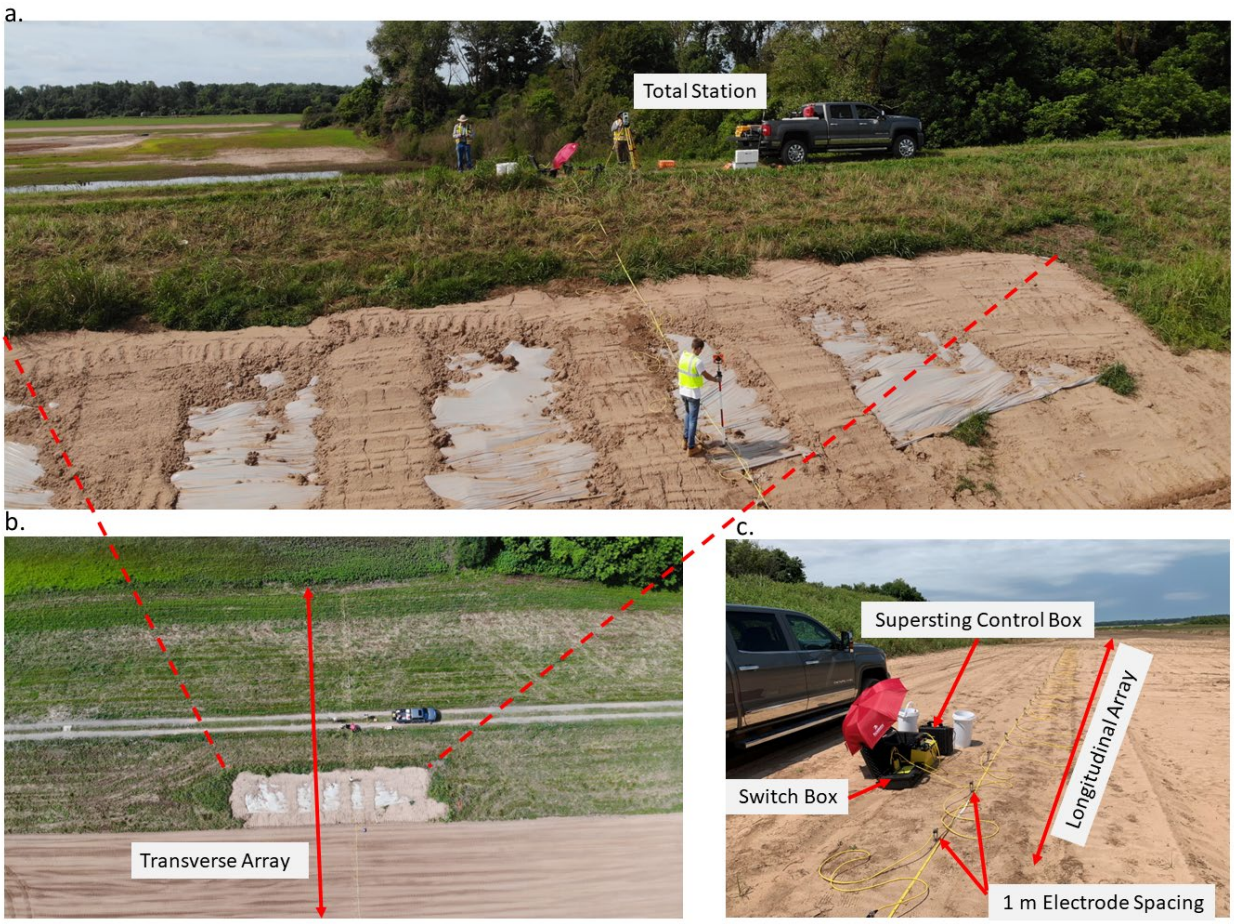

Figure 22 DC ERT field acquisition a) transverse line across 2021 slide (VBL8) with electrode locations being surveyed in by total station b) transverse line across the new seepage berm and levee c) Supersting and switch box at a longitudinal line with 1 m electrode spacing

All ERT Data were processed using the EarthImager 2D (EarthImager) software program from AGI. EarthImager uses an iterative inversion process to solve for the subsurface distribution of ER, resulting in the modeled apparent resistivity distribution. The default parameters for surface

data processing in EarthImager were used with slight modifications. Forward modeling of the apparent resistivity data used a finite element method model with a Cholesky decomposition forward solver and Dirichlet boundary conditions. Additionally, two mesh divisions, a thickness incremental of 1.1 and a depth factor of 1.1, were used in the forward modeling. Prior to inversion, the surveyed topography for each line was imported into EarthImager for inclusion in the inversion. A smooth model inversion process was used for all inversions with a maximum of 8 iterations, a horizontal-to-vertical roughness factor of 0.5, a smoothness factor of 10, a damping factor of 10, and suppression of noisy data. After the initial inversion, poorly fit data was removed using the data misfit histogram tool in EarthImager to remove data with greater than 10 percent relative misfit. The inversion process was then repeated, and further poorly fitting data was removed if the Root Mean Squared Error (RMSE) between the modeled and measured apparent resistivity data was greater than 5 percent. All DC ERT data was high quality, and the final inversion of all DC ERT lines had less than 5 percent RMSE. For each DC ERT line, the effect of inversion settings (e.g., smoothness and damping factors) on high or low ER anomalous features in the inverted ER profiles was explored. The anomalous features were found to have low sensitivity to modification of inversion parameters. The final inverted ER profiles from EarthImager were exported to Sufer 14 from Golden Software to plot the inverted ER profiles using triangulation with linear interpolation.

3.2.3 Capacitively Coupled Resistivity

Capacitively Coupled Resistivity surveys were performed along the levee crest and landside of the project area on September 21, 2021(Figure 15). The CCR surveying was performed using the Geometrics OhmMapper TR5 system and a 5 m dipole length for both the transmitter and receivers (Figure 23). In the OhmMapper TR5 system, five receivers form five dipoles that are separated from the transmitter using various lengths of non-conductive rope, and apparent resistivity measurements are performed using the DD array (Figure 23). As the rope length between the receivers and the transmitter increases, the depth of investigation increases. A pseudo section of apparent resistivity measurements is constructed by dragging the OhmMapper TR5 system with multiple rope lengths across the survey line. The crest line CCR survey used rope lengths of 2.5 m and 5 m, and the landside line used rope lengths of 2.5 m, 7.5 m, and 15 m. For each survey, the OhmMapper system was towed at vehicle idling speeds, and the GPS location of the tow vehicle was continuously measured using the Trimble Geo 7x centimeter GPS (Figure 23). The GPS location and apparent resistivity measurements were recorded with the OhmLog software program from Geometrics during surveying.

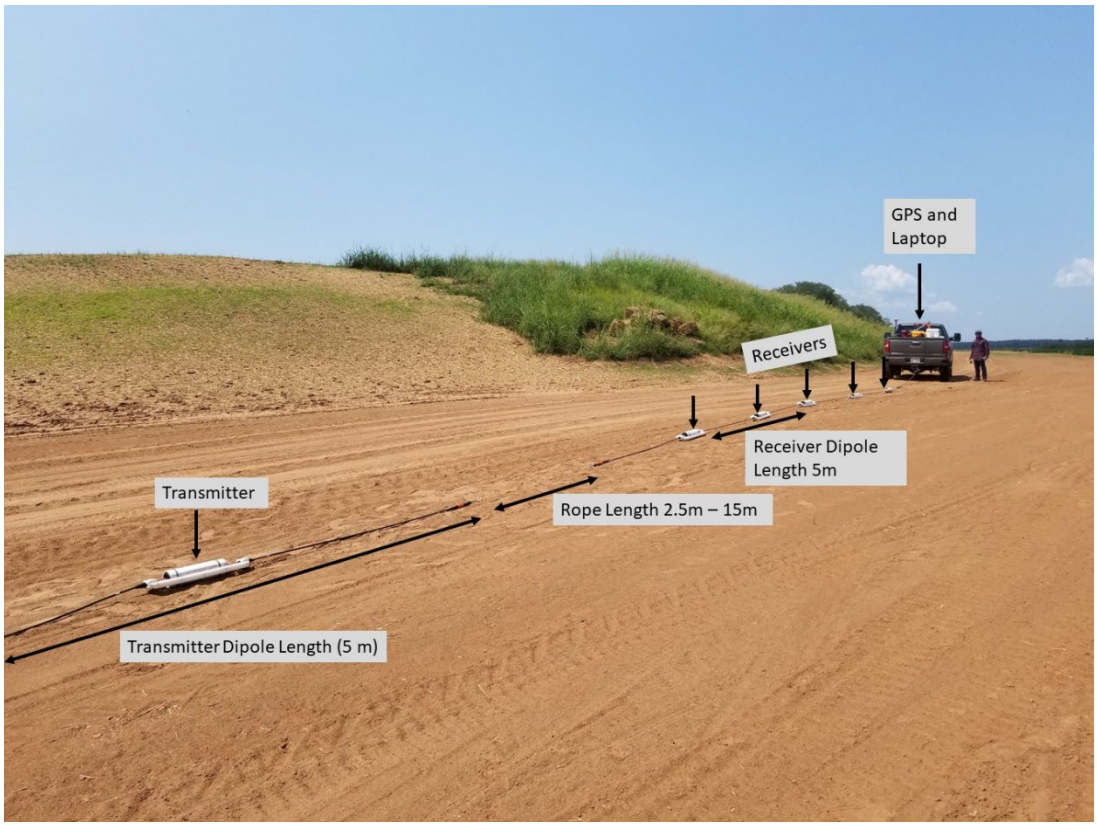

Figure 23 Acquisition of ER data on the levee landside with the Geometrics Ohm-Mapper TR5 system

The apparent resistivity and GPS data recorded by OhmLog were first processed in the OhmImager software from Geometrics to correct the location of apparent resistivity measurements and combine the apparent resistivity data at common locations (i.e., combining the data measured at a given location for each rope length). The data were then exported to the MagMap software from Geometrics to convert GPS data to UTM format and remove dropouts and spikes in the apparent resistivity data. The apparent resistivity profiles were then exported to EarthImager for inversion following the same procedures described for the DC ERT data. The data were overall much lower quality for the CCR surveys, and, where possible higher misfit data was removed, and inversions were repeated until RMSE values of less than 10 percent were achieved. However, for noisier sections of the CCR surveys, RMSE values of the final inversions of approximately 20 percent or less were considered adequate to avoid removing significant amounts of data. The final inverted ER profiles from EarthImager were exported to Sufer 14 from Golden Software to plot the inverted ER profiles using triangulation with linear interpolation.

3.3 Laboratory Testing

The soils tested in the laboratory were selected to cover a range of soil types with different properties. Using benchmark samples, the research team was able to systematically control one set of properties while varying others. This allowed for the influences of different properties on erodibility and resistivity to be singled out and better defined. In total, six different benchmark

soils were created using red art clay (a manufactured natural low plasticity pottery clay), sand (play sand from a home improvement store), kaolin (a manufactured natural pottery clay), and bentonite clay (a manufactured natural clay from Wyoming). The soils were commercially available and were consistent in properties from batch to batch which allowed for tight control and consistency in the benchmark samples created. The composition for these six benchmark samples along with their geotechnical properties can be seen in Table 4.

Table 4 Composition and properties for the benchmark samples used in the laboratory study

Designation	**Soil Composition (%)**				**Soil Classification**	**Atterberg limits**			**Standard Proctor Compaction**	
	Play Sand	Red Art Clay	Bentonite	Kaolin	USCS	LL	PL	PI	Optimum Moisture content (%)	Maximum Dry Density (kg/m^3)
SC-1	70	30	-	-	SC	23	12	11	9.5	2120
SC-2	70	25	5	-	SC	24	10	14	9.6	2128
SC-3	70	15	15	-	SC	61	18	43	11.5	1902
SC-4	70	10	20	-	SC	57	13	44	12.8	1875
SC-5/CL-1	50	50	-	-	SC/CL	26	13	13	10.4	2060
SM-1	70	-	-	30	SM	26	15	11	10.2	1972

USCS – Unified Soil Classification System, LL – Liquid Limit, PL – Plastic Limit, PI – Plasticity Index

The geotechnical properties were determined for each benchmark sample and the soils were classified according to the Unified Soil Classification System (USCS). Liquid limit, plastic limit and plasticity index were determined according to ASTM D4318, and optimum water content and maximum dry density were determined according to ASTM D698. The majority of the soils tested were classified as Clayey sand, SC, except for one soil which was classified as Silty sand, SM. These soils were selected based on the soils previously tested using other HET setups and because they spanned a range of properties that represented common soil types found in levees. The benchmark samples with the soil compositions as described above, created a baseline or control group, and allowed the researchers to vary certain properties/parameters in an effort to link erodibility to non-destructive test methods such as electrical resistivity. For example, moisture content could be varied while keeping density constant, or plasticity index (PI) could be varied (by changing soil composition) while keeping moisture content and density constant, and density could be varied while moisture content remained constant.

In this study, the influence of the PI, dry density, and moisture content was examined using three groups of tests. One of the main difficulties in singling out properties is that many soil properties are dependent on one another, meaning if you change moisture content you also may change density or if you change the plasticity index the optimum moisture and maximum dry density typically change. Therefore, it was important to define the moisture-density relationships for the benchmark samples so that reasonable target values could be chosen and so these conditions could be systematically singled out. Figure 24 presents the compaction curves for the benchmark soils obtained using standard energy.

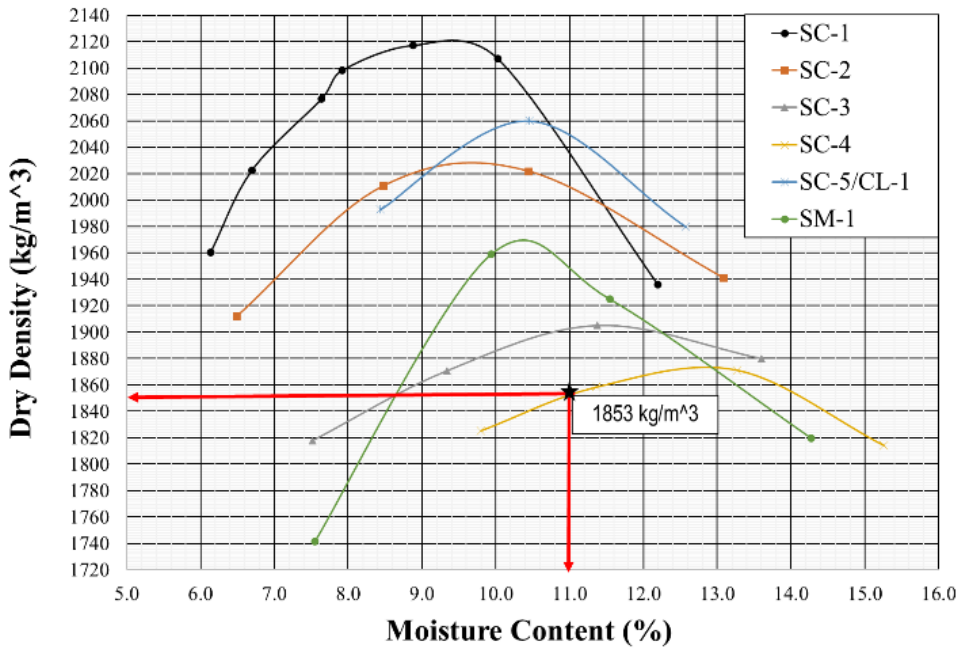

Figure 24 Moisture-density curves using standard energy for each benchmark soil with an example common density and water content point shown

To investigate the influence of the plasticity index, tests were carried out on all of the benchmark samples at the same density and moisture content. The star represents the common density (1850 kg/m^3) and water content (11 percent) that could be obtained for all samples. To obtain this point for the different benchmark samples during the tests, the energy used for compaction was varied to obtain a target density based on a measured mass and sample volume required. While there was some natural experimental variation in the points obtained, the densities tested were within a very narrow range that can be considered constant.

Examining the influence of dry density required keeping the plasticity index and moisture content constant for the tests. This was achieved by performing all tests with the soil designated SC-3, at its optimum moisture content of 11.50 percent. The different dry density were achieved by varying the number of blows used to compact the soil in the Proctor mold for each HET. The standard Proctor hammer was used for all soils compacted in this study. The number of blows used were 25, 22, and 19 (Figure 25). For the resistivity tests, the total dry mass and mass of water needed to achieve the densities obtained in the HET were calculated and the soil was compacted to the target volume.

For the moisture content influence study, the density and plasticity index were held constant. The soil designated as SC-3 was used again, but a density that could be achieved for at least three different water contents was needed. The density obtained with 19 blows was chosen as the target and a horizontal line was drawn across the compaction curve to determine the range of water contents possible (Figure 26). Three water contents were selected (9.30, 11.50 and 13.90 percent) at a density of 1873.00 kg/m^3.

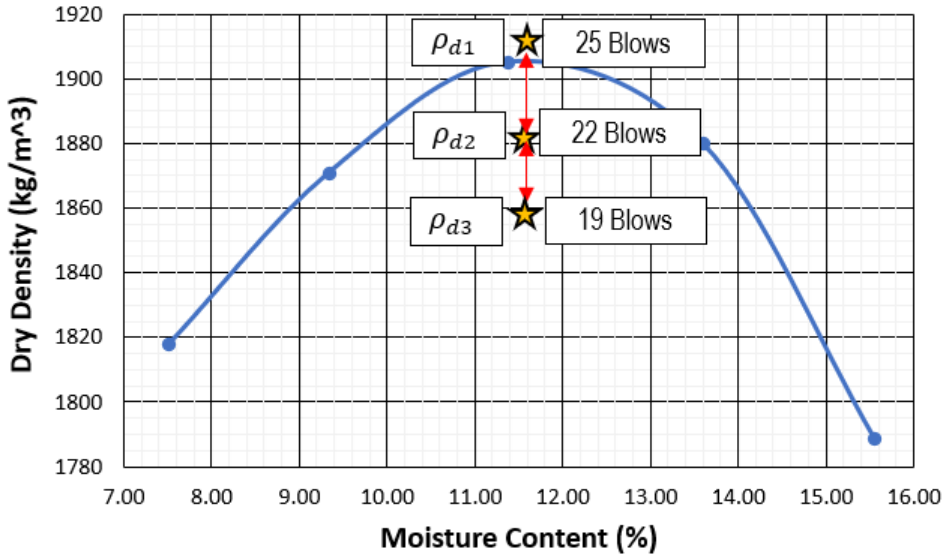

Figure 25 Number of blows used to achieve different densities while holding moisture content and plasticity index constant

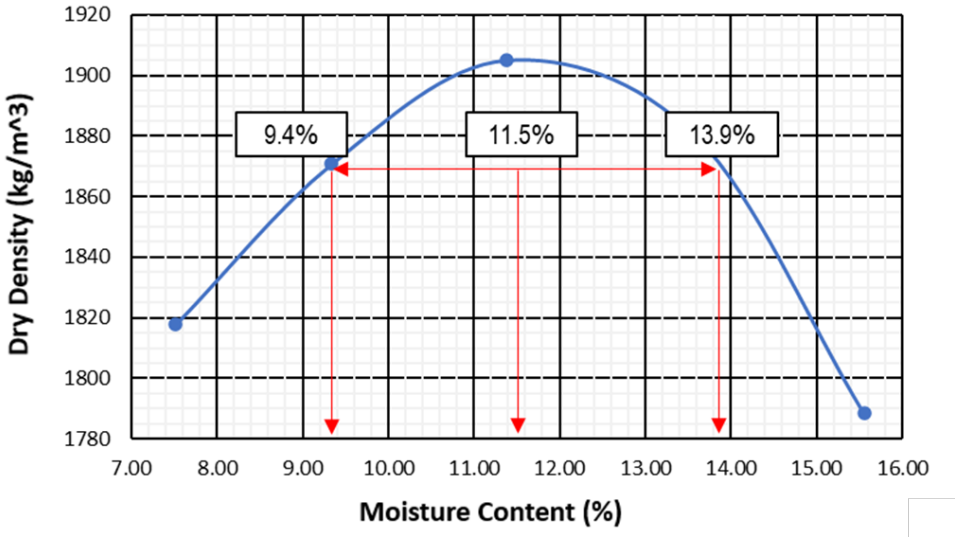

Figure 26 Target moisture contents used while holding dry density and plasticity index constant

3.3.1 Laboratory Electrical Resistivity Testing

The electrical resistivity (ER) of soil is commonly measured in the laboratory using a four-electrode method; two electrodes inject the current, called the current electrodes, and two electrodes to record the potential difference, called the potential electrodes. This method is commonly performed using a soil resistivity box as shown in Figure 27. For soil contained in a box, the following equation shows the relationship between resistivity and resistance for the Wenner four electrode method:

$$\rho = R \times \frac{A}{L} \tag{7}$$

where ρ = resistivity in Ohm-cm, R = resistance in Ohm, A = cross sectional area of the container perpendicular to the current flow in cm^2, and L = distance between electrodes in cm. The same system used by Kouchaki et al. (2019) consisting of a Nilsson Resistance Meter Model 400 in a 4-electrode array with an M.C. Miller Large Soil Box was used to measure the ER of the soil specimens. The cross-sectional area and length of these boxes are specifically chosen so that the measured value is the resistance for the soil. Figure 27 shows a schematic of the resistivity soil box setup used in this study.

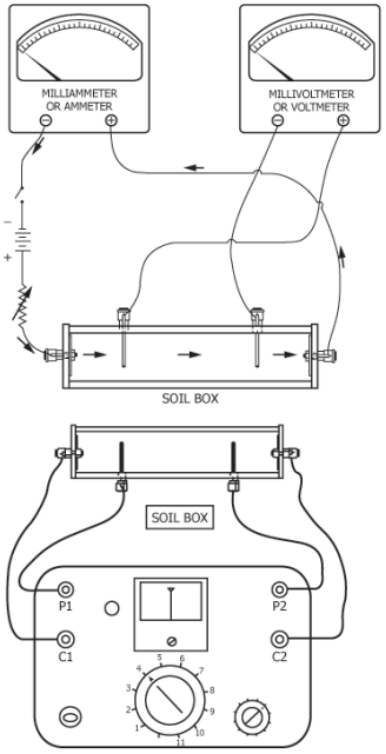

Figure 27 Schematic of soil resistivity box used in the study (ASTM G57-20)

To obtain the target conditions for the ER tests, the dry mass of soil was calculated, measured out, mixed with the calculated target amount of water, and then compacted to fill the volume of the soil box to achieve the target density. Initially the soil and water were weighed on a scale with an accuracy of 0.01 g. These were then mixed uniformly and placed in a container for a period of 24 hours at a controlled temperature and humidity to bring the soil to equilibrium and ensure that the moisture content was uniform throughout.

Prior to the test, the soil was weighed again to ensure that the water content was met, then the soil was placed in the box and compacted to the required density. The temperature also influences the measurement of resistivity, so it was taken in three different locations to obtain an average. The

average temperature for the tests ranged from 21.3 to 21.6ºC. According to ASTM G57-20, any temperatures over 21ºC should be corrected to 15.5 ºC using:

$$\rho_{15.5} = \rho_T \left(\frac{24.5 + T}{40}\right) \quad (8)$$

The same samples tested in the HET were tested in the ER box to obtain a relationship between erodibility and resistivity. One issue encountered was that the density in the soil box was typically lower than the density in the compaction mold used in the HET. Only so much energy could be used when compacting the soil in the ER box and it was difficult to achieve the higher density values representing 22 or more blows. The values obtained are presented herein, but it is recommended for future research to consider conducting the ER tests on compacted cylindrical specimens that can be compacted using the standard Proctor hammer.

3.3.2 Laboratory Hole Erosion Testing

3.3.2.1 UARK HET Development

To measure the soil erosion rate index (ERI), a Hole Erosion Test (HET) system was developed at the University of Arkansas (UARK). The design is similar to the original HET presented by Wan and Fell (2002), but several modifications were made to overcome some issues with other existing devices.

The UARK HET system consists of an upstream flow tube which is connected to a water source on the upstream side. One major modification of this device is that a water supply was used to control pressure head and flow rate as opposed to controlling the elevation of a tank mounted on the wall. More discussion of the water supply and flow valves are given below. The flow pipes are schedule 80 PVC clear pipe, 24 inches in length and 4 inches internal diameter. The downstream flow pipe is identical to the upstream pipe and is much longer than most other existing HET devices. This longer downstream pipe was incorporated to reduce the turbulence and back flow that occurs as the water exits the smaller diameter hole in the soil sample. This turbulence can lead to disturbances and inaccuracies in the differential pressure measurements. The UARK HET device is shown in Figure 28.

The downstream flow pipe is connected to a collection basin with two separate basins. The first basin is the collection basin for the water exiting the downstream flow tank. This basin has a constant pressure head to allow the pressure in the HET system to stay constant before the test has been initiated. Once the test has been initiated, the water overflows into the second basin. This basin contains a v-notch weir that is used to determine the flowrate during the test. A submersible diaphragm connected to a pressure sensor was placed such that the water level in the v-notch weir could be digitally recorded during the test.

The sample is contained within a standard proctor mold which is fastened to the upstream and downstream pipe flanges by four all-thread bolts and nuts. The sample is placed between the two

flow tanks and secured by tightening these bolts such that no leak is present which would be serious as the pressure differential would be incorrect during the test. To record the upstream head pressure, differential pressure, and the flowrate, a NPX MPX5010 sensor was used with a 1408FS USB acquisition card. A program was also written in Agilent Vee to show the data in real time and record the data in a spreadsheet.

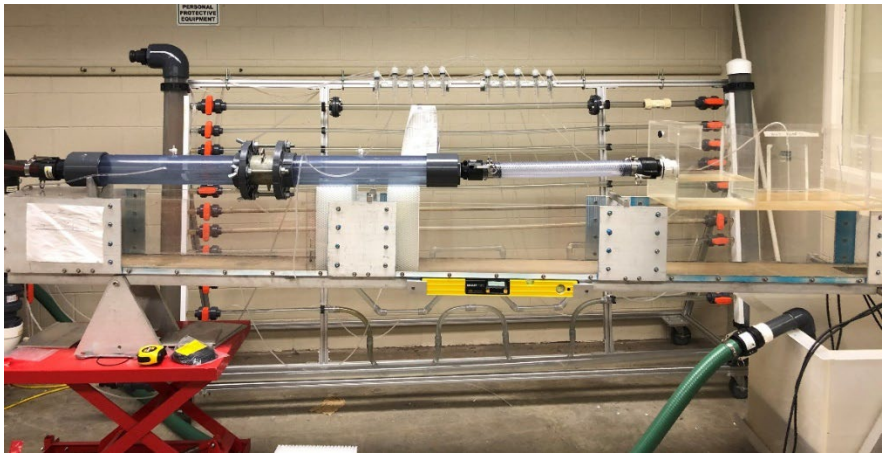

Figure 28 UARK HET device

As discussed, a water supply was used to control pressure head and flow rate as opposed to using an elevated tank mounted to the wall. Using a pump system overcame limitations of other systems that could not test high strength soils as the pressure required to test such materials was not possible unless the facility had very high ceilings. The first iteration of the UARK HET used the setup shown in Figure 29 and consisted of a dual pump system with a large water tank attached such that the water can be recycled during the test.

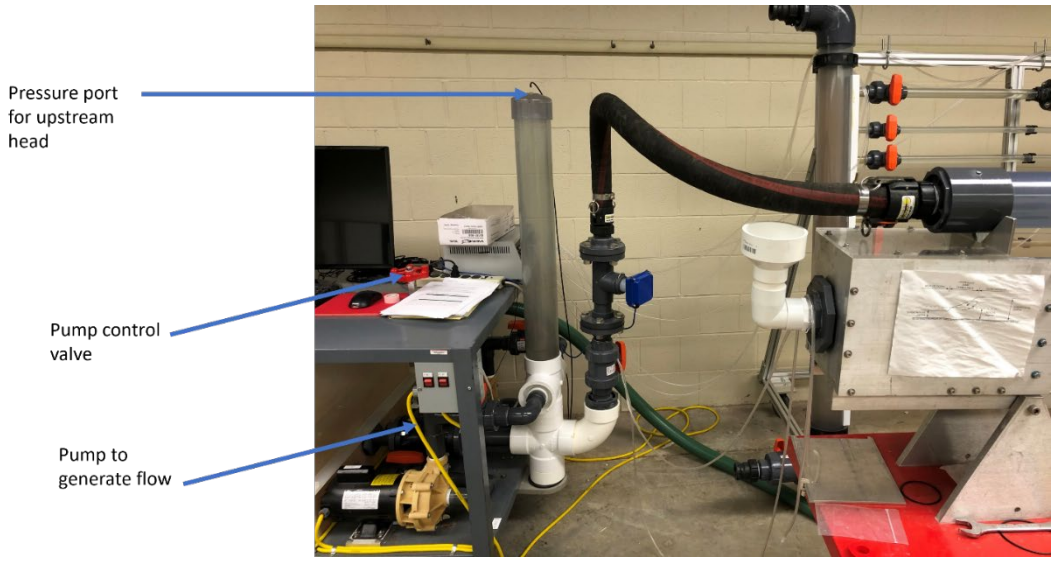

Figure 29 Pump system used in the first iteration of the UARK HET

This pump system produce pressures up to 20 psi (which equals about 50 ft in terms of head pressure) and was able to pump enough water to maintain this pressure even for soils with high erodibility which would result in large, eroded diameters in the sample. The pump system, as shown in Figure 29, consisted of two pumps that fed into one pipe with a pressure port connected to a transducer to measure the pressure in the system before reaching the HET system. Between the pipe and the pressure port, a pump control valve was placed to control the upstream pressure head. The system functioned well, however, there were a few issues with this setup. The main issue was the pressure from the pump was not stable. As the test continued, the pressure from the pump would fluctuate without changing the position of the gate valve. This was an issue that could not be overlooked as constant pressure is vital when performing a HET.

The second issue that was experienced when using the pump and reusing water for this test was the turbidity of the water. This was an issue because one of the main goals was to incorporate a submersible camera to the downstream flow tank to record the sample and the erosion of the sample during the test to obtain a more accurate method of determining the erosion characteristics of the HET. Reusing water in this test was particularly problematic when testing soils with higher clay contents as the clay particles stay suspended in the water. The amount of water used for a test also exceeded the amount of water that the tank could hold making it impossible to use a constant supply of clean water in this setup. Several different filters were tested but none of the options solved the turbidity problem. Additionally, because of the sporadic performance of the pump it was concluded that it was not feasible to continue with the development of this particular setup.

The second iteration of the UARK HET had to be a system that could keep the flowrate and head pressure constant but also provide “clean” water so that a submersible camera could record the sample from the downstream flow tank. The solution to these issues was to connect the upstream flow tank directly to a hose that connects to the water supply line for the laboratory. This allowed for fresh water to pass through the system at a consistent flow rate and pressure. A gate valve was added between the spout and the upstream flow tank to control the flow. This setup is shown in Figure 30 and ended up being the final iteration of the UARK HET.

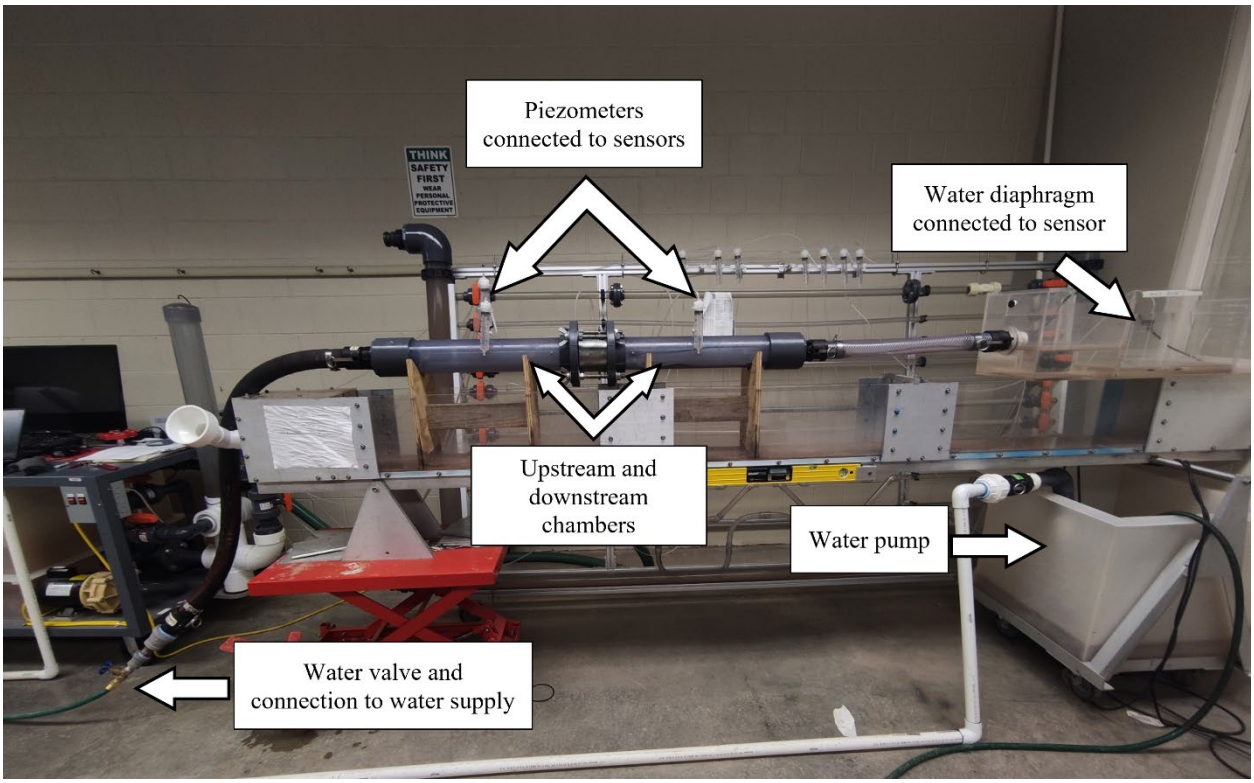

Figure 30 Second and final iteration of the UARK HET showing the water supply and valve used to control pressure head and flow rate in the system

3.3.2.2 UARK HET Camera System Development

In the existing HET devices, the diameter of the hole is only known at the very beginning of the test and at the very end once the sample is removed from the system. This can be an issue if the sample starts to slowly erode before the system setup is able to detect an increase in flowrate and leads to an incorrect hole diameter at the start of erosion. It is also an issue at the end of a test because even though the system may be shut down, the water does not stop flowing immediately and some erosion could be measured by the operator that is not captured in the flow data recorded. Additionally, the use of calipers to measure the hole size before and after the test is very user dependent and it is difficult to obtain accurate estimates when the hole is not symmetrical.

The test setup proposed introduced the use of a submersible camera inserted in the downstream flow-tank to accurately measure the hole diameter at each interval of pressure along with a reference calibration sheet at the downstream side of the sample to provide scale. The reference calibration sheet was needed because the focal length had to be varied to obtain a clear picture. The reference sheet contained a number of lines with known dimensions that could provide scale regardless of the placement of the camera or focus settings. At the completion of the test, the images are analyzed using an image processing tool to determine the exact diameter and shape of the hole based on the dimensions of the reference lines in the same image.

The camera used is a NTS300 Pro Auto-Focus Inspection Camera which includes an illuminated lens and 9.8 feet of probe length. To keep the camera stable and centered in the downstream pipe, a holder was developed. A 3D printed cylinder was used to encase the lens and four pieces of flexible plastic wire were used for support to keep the lens centered in the flow pipe. The addition of the camera system made it possible to get an accurate measurement of the eroded hole before, during, and after the test and is not as subjective as current methods. Figure 31 shows the camera with holder and the reference calibration sheet with lines of known length to provide scale and dimensions in the images.

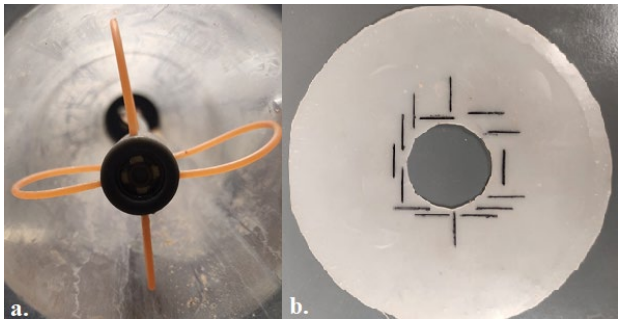

Figure 31 (a) Camera and holder positioned within pipe, and (b) calibration reference sheet used to obtain dimensions within each image regardless of camera placement

For this test to be as accurate as possible, the effects of placing the camera and the cord inside the flow-pipe must be negligible. There was concern that the camera may create more turbulence and increase the amount of erosion on the downstream side of the sample and that it could also lead to greater head loss in the system. To test the effects of the location of the camera, a Plaster of Paris sample with a PVC pipe used for the central hole was placed in the system. The camera was then placed at several distances from the sample in the downstream flow pipe and the differential pressure was recorded. During the test, the flow rate was kept at a constant level to accurately determine if the differential pressure was affected by the location of the camera. Table 5 shows the results of this test.

Table 5 Differential pressure measurements for camera locations measured from differential pressure sensor

	Flow (L/min)						
Location	0.23 (psi)	0.5 (psi)	1.00 (psi)	2.00 (psi)	3.00 (psi)	4.00 (psi)	6.00 (psi)
9 inches to the left of sensor	1.69	2.28	3.14	4.36	5.35	6.18	7.85
4.5 inches to the left of sensor	1.66	2.25	3.14	4.38	5.31	6.17	7.78
At sensor	1.68	2.26	3.11	4.38	5.33	6.22	7.88
4.5 inches to the right of sensor	1.67	2.25	3.12	4.36	5.34	6.2	7.94

As indicated by the results in Table 5, the measured differential pressure remains relatively unaffected by the location of the camera for the range of flow rates tested. The differences observed are due to noise in the sensor system as opposed to any influence in the camera.

3.3.2.3 HET Testing

The test preparation consists of preparing the soil sample and the apparatus for testing. The sample preparation starts by mixing the soil and water to the target conditions before testing to allow the soil to be fully hydrated. The soil is then placed in a sealed plastic bag and stored in a closed container for 24 hours before being compacted according to the target energy requirements. Initial water content and density were recorded to corroborate compliance with the targeted values. Once the soil was compacted, a 6.00 mm diameter hole was drilled along the center of the soil sample to simulate tunnel erosion using a drill. Subsequently, the initial hole diameter was measured using a Vernier caliper. This value ranged from 5.95 mm to 6.00 mm for all tests.

To prepare the system for testing, the pipes, O-rings, and flanges should be cleaned to avoid soil contamination and any leaks during testing. Once clean, vacuum grease can be applied to the O-rings and they can be placed in the flanges. The calibration disc is then slightly greased and placed in the downstream tank flange. The sample, with a 6.35 mm hole drilled, can then be inserted between the flanges and secured using the four bolts and the pressure tubes can be connected. The HET system is leveled using a vertical displacement table and digital level and the computer data acquisition and monitor can be turned on and initialized. Before the start of a test, the system can be zeroed with the water level in the downstream tank as close to the bottom of the v-notch weir as possible.

The system is filled with water by filling both sides simultaneously. When the two sides are full and the downstream tank is at the required water level, the program can be started, and the first differential pressure can be obtained. The initial flow rates corresponded to no more than 0.10 L/min and the differential pressure to 30.00 mm in terms of water column. If the initial differential pressure was not sufficient to produce erosion, which is indicated by a change in flow rate, the pressure was increased using the gate value at intervals of at least 140.00 mm. Once erosion was initiated, the flow valve was opened gradually to try and keep the differential pressure constant.

For the soils tested in this investigation, the differential pressure values that initiated erosion ranged from 70 to 2800.00 mm H_2O, with test times ranging from 20 minutes to 1 hour or until the highest possible flow rate was reached. After each increase in differential pressure, a photograph was taken using the camera to observe whether there was an increase in diameter. This differs from the traditional test method where only one pressure head is used once erosion has begun. Obtaining data and multiple eroding pressures was explored in this study to determine the feasibility of measuring an erosion function similar to the EFA as opposed to one single index value. In each test performed, the water temperature was also taken, which ranged from 17.50 to 23.00 ºC.

Once the test was completed, the mold with the sample was removed and the final diameter was measured using a Vernier caliper, in addition to determining the final length of the soil sample. The ImageJ program was then used to corroborate that the initial and final diameters were like

those measured with the Vernier caliper; if not, then the new diameters determined with the software were used. For the determination of the ERI and the applied shear stress values, a Microsoft Excel template was developed to automate and facilitate the calculations.

4 Results/ Findings

4.1 Capacitively Coupled Resistivity Surveys and Review of Project Site Geology

Capacitively Coupled Resistivity surveys were performed across the levee crest and landside for the full project site (Figure 32). The CCR profiles provide continuous assessment of changing subsurface conditions across the entire project site and allow for the location of potential internal erosion areas that require further geophysical testing. The CCR profiles of the levee crest and landside and historical boring logs of the project site are presented in Figures 32 and 33, respectively. The CCR profiles and historical boring logs are aligned with black and white United States Geological Survey (USGS) aerial imagery of the project site during a high-water event in March of 2001. This imagery was selected to highlight saturated low-lying areas on the levee landside and highlight the ridge and swale topography of the project site. Overall, the CCR data was of lower quality than the DC ERT data; however, the CCR profiles provide valuable insight into the overall geology of the project site and allow for the targeting of further geophysical testing. Due to a malfunctioning receiver, only four receivers were used with the Ohm-Mapper TR5 system for the crest line and the first 750 meters of the landside line, leading to a decreased depth of investigation for those survey segments.

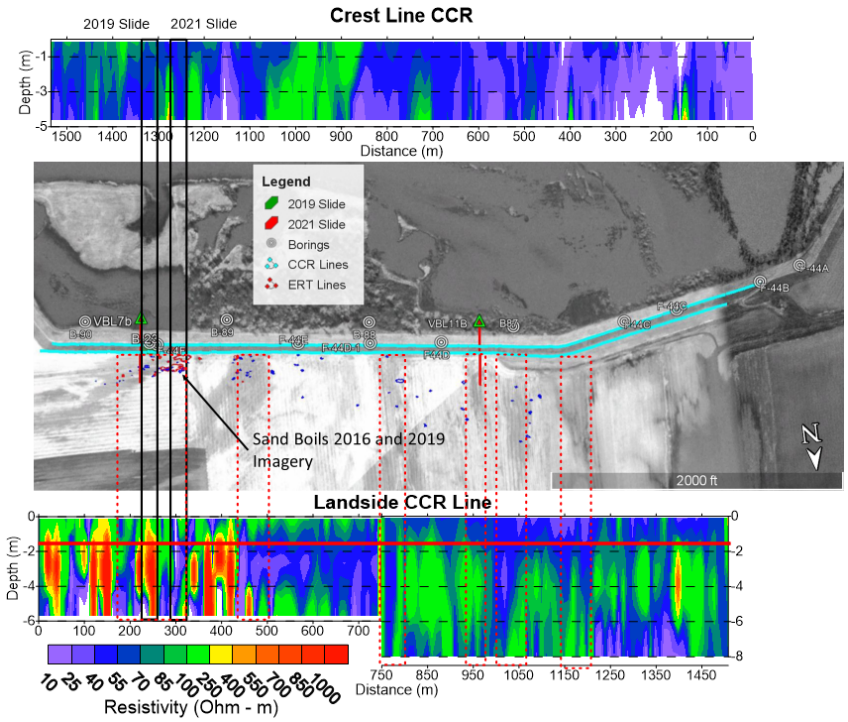

Figure 32 Crest and landside CCR lines aligned with USGS aerial imagery from March 2001

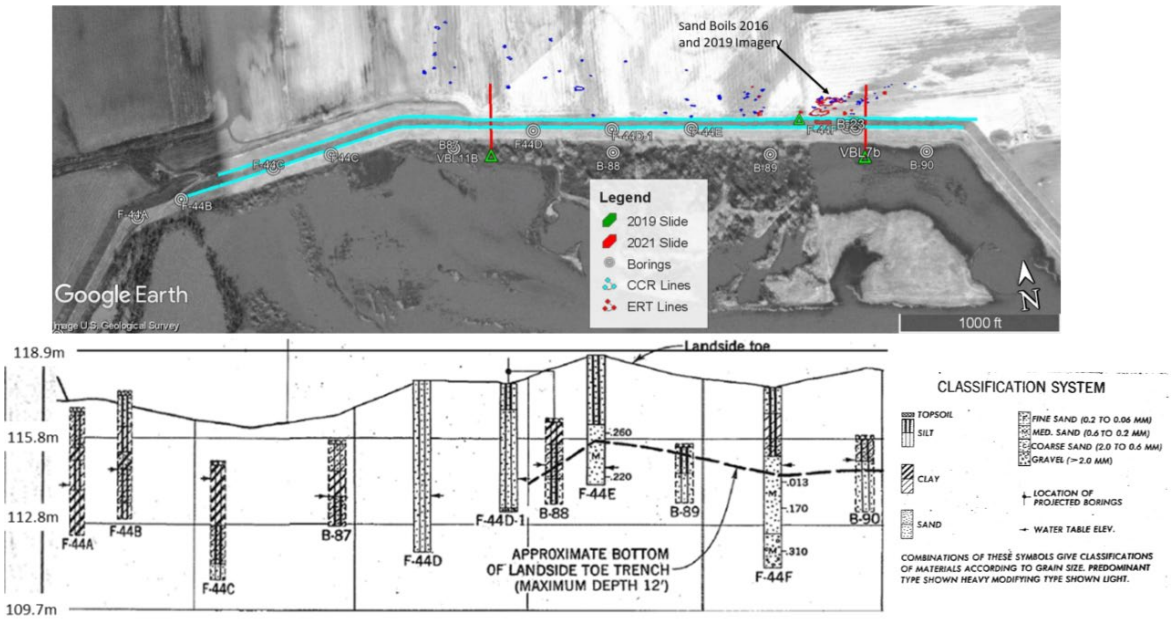

Figure 33 Historical boring logs aligned with USGS aerial imagery from March 2001

The DC ERT and CCR profiles were compared with boring logs to develop a relationship between ER and soil type. In general, sandy soils are associated with ER greater than 70 ohm-m, and silty and clayey soils with ER less than 70 Ohm-m. The thickness and material type of the seepage berm must be considered when interpreting landside geophysical surveys. The seepage berm is approximately 1.5 m thick at the interface between the seepage berm and levee, and the seepage berm material classified as Poorly Graded Sand (SP). The seepage berm material is 20 percent medium-grained sand, 80 percent fined-grained sand, and 1 percent finer than the number 200 sieve; however, it is uncertain if the sample is fully representative of the seepage berm material. In the first 430m of the landside CCR line, high ER anomalies of over 1000 ohm-m are present, separated by lower ER soils (Figure 32). At the location of the 2019 slide, there is a high ER anomaly in the landside CCR line and a low ER anomaly at the 2021 slide adjacent to a high ER anomaly. It can be observed in the internal erosion area that the 2021 slide and heavy sand boil activity are located along the western margin of a darker saturated area from approximately 175 to 310 m along the landside CCR line (Figure 32). This area is interpreted as a clay-filled swale in the ridge and swale topography of the point bar deposits that cross underneath the project site. Additional features in the landside CCR that are interpreted to be clay-filled swales are identified in Figure 32. In the first 430 m of the landside CCR line, there is minimal to non-existent conductive top stratum present (material less than 70 ohm-m) outside of the interpreted swale areas. The amount of conductive top stratum present can be estimated by looking below the estimated bottom of the newly constructed and existing seepage berm (indicated by a red line in Figure 32). Moving toward the control area, the thickness and continuity of the conductive top stratum increase. Additionally, it can be observed that in the internal erosion area, the point bar deposits are at a shallow angle with respect to the levee and that moving west towards the control

area, the deposits are approximately perpendicular to the levee (Figure 32, Figure 33). Notably, the orientation of point bar deposits with respect to levees is a significant geological control on under seepage and sand boil formation during high water events. When the point bar deposits (with ridge and swale topography) cross levees at an acute angle, as in the internal erosion area (Figure 32), seepage in high permeability ridges is concentrated along the edge of clay-filled swales leading to sand boil formation (Kolb, 1975). In areas where point bar deposits are nearly perpendicular to levees, such as in the control area, sand boil formation is still typically along clay-filled swales; however, sand boil locations are less concentrated and more randomized when point bar deposits are nearly perpendicular to levee alignments (Kolb, 1975).

The CCR crestline survey has a depth of investigation of 4.75 m and does not extend to the levee foundation materials. In general, the high ER anomalies in CCR crestline correspond to high ER anomalies in the landside line and areas of thin or non-existent conductive top stratum (Figure 32). High ER anomalies are present in the crestline between the 2019 and 2021 slides and to the west of the 2021 slide. A high ER interval is present in the crest line from 1060 m to 800 m without co-located high ER anomalies in the landside line, which is potentially due to differences in borrow pit materials. The borrow pits for the levee are located directly on the riverside of the levee and should generally consist of similar materials to those observed on the landside CCR line; however, from approximately 1250 to 700 m along the CCR lines, the borrow pits are not located directly adjacent to the levee. Moving to the west from 880 m along the crestline, the levee materials become more conductive, which may be attributed to increasing clay content of borrow pit material moving towards the west (Figure 32, Figure 33).

The historical USACE boring logs from the design and construction of the levee are aligned with the March 2001 USGS aerial imagery in Figure 33. The primary soil type is shown in bold, and secondary soil types are shown in non-bold, with dots representing sands, angled lines representing clays, and vertical lines representing silts. Moving to the west along the levee, it can be observed that the silt and clay content of the borings increases; this is consistent with the expected decrease in sand content when moving toward the outside (convex) side of point bar deposits (Kresse et al., 2015). Additionally, the increased clay content moving west along the levee can be attributed to a clay-filled channel plug that intersects the levee at 1375 m along the landside CCR line (Figure 20, Figure 1).

The CCR surveys successfully identified subsurface conditions that are susceptible to the formation of sand boils and subsequent internal erosion damage, such as the continuity and thickness of conductive top stratum across the landside of the project site. Additionally, the landside CCR line resolved high ER anomalies in the vicinity of the 2019 and 2021 slides in the internal erosion area. A combination of preliminary CCR surveying, review of aerial/satellite imagery, and review of historical boring logs was effective in selecting locations for more in-depth geophysical assessment of internal erosion damage at the project site. While the location of internal erosion damage at the project site was apparent before CCR surveying, for levee reaches without

apparent internal erosion damage CCR surveys can be rapidly acquired to locate potential zones of internal erosion damage for further geophysical testing.

4.2 Research on the Internal Erosion Area

4.2.1 Internal Erosion Area

The most extensive geophysical testing was performed in the internal erosion area and adjacent areas to assess the internal erosion damage in the area. Ground-truthing of the geophysical data was performed with boring logs and satellite and aerial imagery to locate levee distress features (i.e., sand boils and slope stability failures). The geophysical testing in the internal erosion area included longitudinal crest and landside DC ERT Lines, transverse DC ERT lines, and crest and landside MASW lines. First, the DC ERT results are discussed, followed by a comparison of co-located DC ERT and MASW lines and then a temporal comparison of co-located DC ERT lines. The DC ERT lines in the internal erosion area are presented in three figures, including longitudinal lines (Figure 34), all internal erosion area transverse lines (Figure 34), and long transverse lines, including VBL17 and VBL18 adjacent to the internal erosion area (Figure 35). All figures are oriented facing towards the levee landside (i.e., in longitudinal figures, the crest line is located at the top of the figure, and for transverse line figures, the furthest east line is located at the top of the figure). Annotations to DC ERT profiles include sand boil locations (from satellite imagery), slide locations (from satellite imagery and field visits), high ER anomalies (red dashed lines), low ER anomalies of interest (white dashed lines), and groundwater elevation measured from the B-23 piezometer (when measured). High ER anomalies were identified and given an identification number for all DC ERT lines at the project site. High ER anomalies (ER greater than 70 ohm-m) were identified as anomalous zones of high ER within low ER materials (e.g., high ER zones within the levee body or below the seepage berm) or surface zones of high ER that correspond to sand boil locations or that are located above zones of conductive top stratum thinning.

The same classification of soil type applied to the CCR lines was applied to the DC ERT lines, with ER values greater than 70 ohm-m corresponding to sandy soils and ER values less than 70 ohm-m corresponding to silts and clays. Comparing B-23 to VBL5, it can be observed that the transition from silts in the levee body and foundation to sands is correctly located using this approximate soil type classification based on ER (Figure 34). In B-23, the raw standard penetration test (SPT) n-values and the USCS soil classifications are provided on the left and right sides of the boring log, respectively. The elevation of the sand unit (higher ER material) in VBL5 (Figure 34a) below the levee is variable and increases in elevation below the 2019 and 2021 slides and below the location of high ER anomaly E2.

In the internal erosion area crest line VBL5 (Figure 34a), high ER anomaly E1 is present between the 2019 and 2021 slides and coincides with anomaly E4 in the seepage berm ERT lines VBL1 and VBL6 (Figure 34b). Anomaly E4 extends below the estimated extent of the seepage berm (elevation 117 m) and into the 2019 slide area. Additionally, the location and elevation range of anomaly E4 is consistent with anomaly E16 on transverse line VBL12 (Figure 35c) and E18 on

transverse line VBL15 (Figure 35d). Below anomaly E4 in VBL1 (Figure 35b), a thinning of the more conductive unit at 45 m (elevation of 111 to 115 m) is present, which may be due to internal erosion damage resulting from the formation of E4 (Figure 34b).

A second high ER anomaly, E2, in crest line VBL5 (Figure 34a) is present within the levee body. Anomaly E2 aligns with high ER anomaly E23 in transverse line VBL9 (Figure 35g), which spans horizontally through most of the levee body. No levee distress features are present in satellite imagery at the location where E2/E23 would exit the landside slope, and the feature may be a construction defect due to borrow pit variability. However, there is an increase in elevation in the higher ER unit at the location of E2 on the crest line VBL5 (Figure 34a) and the transverse line VBL9 (Figure 35g) at 48 m, corresponding to the location of the landside toe prior to seepage berm construction. The upward flow of high ER materials observed in VBL5 and VBL9 at the location of the landside toe prior to seepage berm construction may be a zone of internal erosion damage to the conductive top stratum resulting in the upward flow of aquifer sands.

In addition to anomaly E4 in Figure 334b, two additional high ER anomalies, E3 and E5, were identified in landside lines VBL1/VBL6 (Figure 34b) along the edge of the seepage berm closest to the levee. Anomaly E3 on VBL1 (Figure 34b) is located within the horizontal extent of the 2019 slope failure and corresponds to anomalies E10 and E13 in transverse lines VBL7B (Figure 35a) and VBL7 (Figure 35b), respectively. However, these anomalies (E3, E10, and E13) are fully within the extent of the seepage berm and are interpreted to be due to the seepage berm construction and the slope failure repair process. Similarly, anomaly E5 on VBL6 (Figure 34b) within the 2021 slide area is attributed to seepage berm construction and repair of the 2021 slope failure. In the google earth satellite imagery from October 2021 of the project site, it can be observed that the seepage berm construction involved mounding of borrow pit material along the interface of the seepage berm and landside toe; this is likely the cause of the high ER anomalies observed at the interface of the landside toe and seepage berm including anomalies E10(VBL7B) (Figure 35), E13(VBL7) (Figure 35b), E21(VBL13) (Figure 35e), and E22(VBL8) (Figure 35f). The increased ER of anomalies E16 on VBL12 (Figure 35c) and E18 on VBL15 (Figure 35d) compared to surrounding transverse lines is potentially due to the gravel placed on the 2019 slide during flood-fighting efforts. A comparison of suspected zones of internal erosion damage in both longitudinal and transverse DC ERT lines was valuable for interpreting the cause of a given high ER anomaly.

No anomalies were identified in longitudinal line VBL2 (Figure 34c), and the transition from conductive materials to sandy materials occurs at 113 m to 114 m. The estimated seepage berm thickness at VBL2 is 0.6 m, with an estimated conductive top stratum thickness of 2 m. VBL2 is located between areas of heavy sand boil activity at the landside toe (prior to seepage berm construction) and near VBL16. At 20 m along VBL2, there is an increase in conductive top stratum thickness that coincides with the edge of the interpreted swale area.

Line VBL16, in Figure 34d, is the farthest north landside longitudinal line acquired and is located along areas of heavy sand boil activity. At the time of data acquisition, VBL16 was located beyond

the extent of seepage berm construction and included the high ER anomalies E6, E7, and E8. The locations of anomalies E6, E7, and E8 can be observed to directly correspond to the locations of sand boils in Google Earth satellite imagery of the project site from March 2016 and June 2019. Anomalies E6 and E7 coincide with sand boil locations, and below these anomalies thinning of the conductive top stratum and upward flow of high ER materials can be observed. These anomalies are interpreted as zones of internal erosion damage to the conductive top stratum and subsequent upward flow of aquifer sands. Between anomalies E6 and E7, a low ER zone is delineated; this zone corresponds to a saturated area in the 2019 Google Earth imagery and is interpreted to be a clay-filled swale. The location of E8 correlates to an area of extensive sand boil activity, and deposits of sand boil ejecta and high ER material can be observed flowing to the surface through the conductive top stratum. The larger extent of sand boils delineated from satellite and aerial imagery compared to anomaly E8 is attributed to deposits of sand boil ejecta that have been reworked in agricultural processes. For anomalies E7 and E8, determining locations of internal erosion damage using visual methods alone would be problematic. For example, the location of internal erosion damage at E8 is obscured by overlapping deposits of sand boil ejecta from multiple sand boils, and ERT allows for the location of the internal erosion zone forming the sand boils. To the west of anomaly E8, a second low ER zone is delineated that is interpreted as a second clay-filled swale. Notably, sand boil activity within these interpreted swale zones is limited, and sand boils are primarily present along the eastern and western edge of the first interpreted swale area from 22-53 m. For example, VBL13 (Figure 35e) in the interpreted swale area does not have any upward flow of high ER materials at the landside toe prior to seepage berm construction. While in the surrounding transverse lines VBL15 (Figure 35d) and VBL8 (Figure 35f), located at the margins of the swale area, an upward flow of high ER materials can be observed at the former landside toe location. Additionally, the 2019 and 2021 slides formed on the eastern and western edge of the interpreted swale area (22-53 m on VBL16), respectively. The rapid horizontal change in hydraulic conductivity at the interface of a swale creates a blocked exit condition, leading to increased hydraulic pressure and sand boil formation (Kelley et al., 2019).

As discussed in Chapter 4.2, the orientation of point bar deposits with respect to the levee is a significant geological control on the location and severity of sand boil formation and subsequent internal erosion damage (Kolb, 1975). In the satellite imagery of the internal erosion area, it can be observed that sand boil formation is concentrated along the eastern and western edges of the interpreted swale area in the high permeability ridge deposits. Additionally, the presence of borrow pits directly adjacent to the riverside slope of the internal erosion area levee likely contributes to the internal erosion issues. The borrow pits expose aquifer sands leading to the initiation of seepage and high hydraulic gradients across the levee during high-water events. The borrow pit removal of the riverside conductive top stratum is apparent in the transverse ERT lines (Figure 35) of the internal erosion area. Another potential contributing factor to the internal erosion and slope stability issues in the internal erosion area is the levee being constructed with silt. Silt soils are susceptible to collapse and loss of shear strength when wetted. Internal erosion damage at the

landside toe, in combination with saturation and subsequent collapse and loss of shear strength in the silt levee soils, is likely responsible for the 2019 and 2021 slope stability failures.

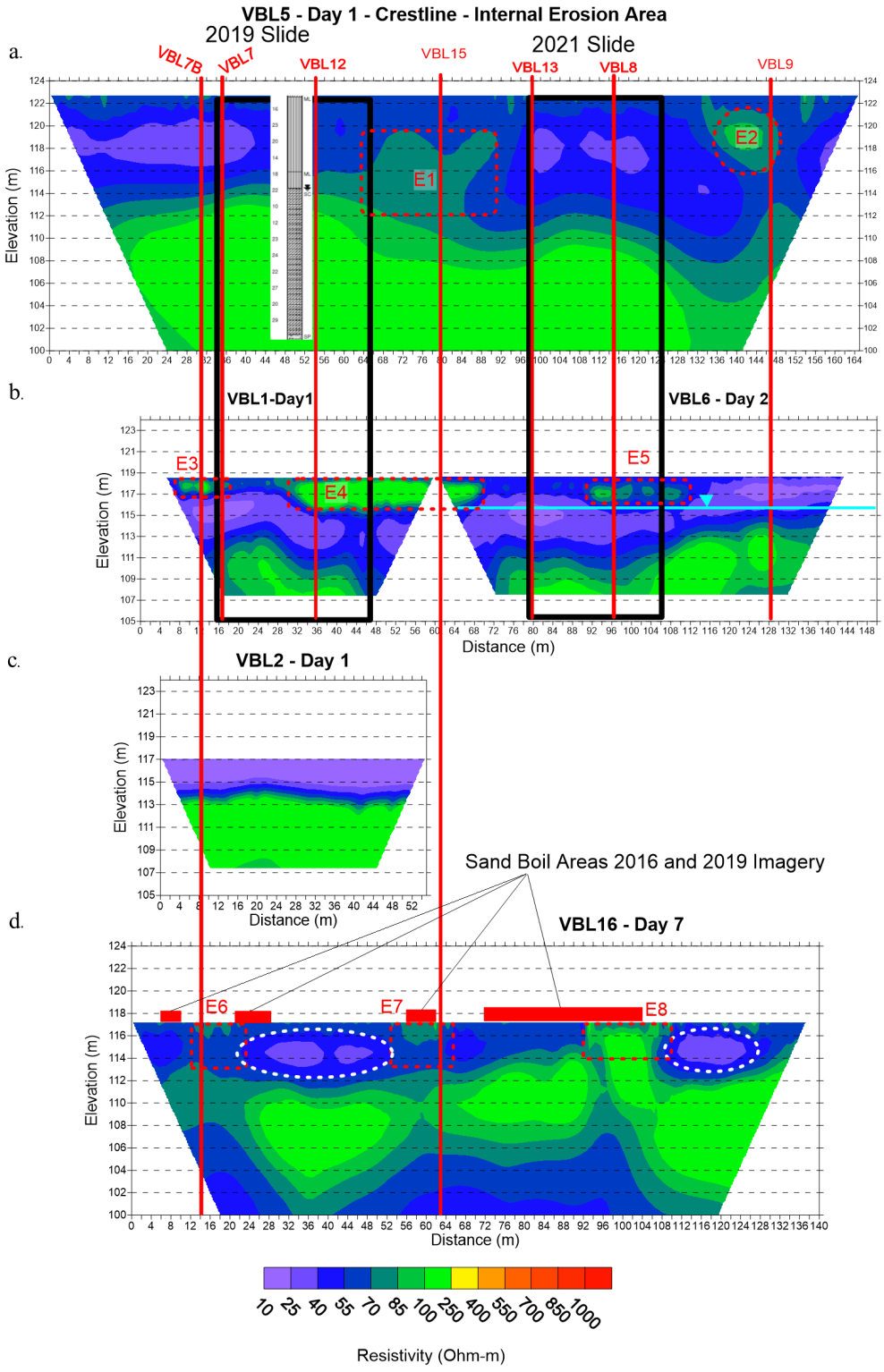

Figure 34 Internal erosion area longitudinal DC ERT lines, a)VBL5, b)VBL1/VBL6, c)VBL2, and d) VBL16

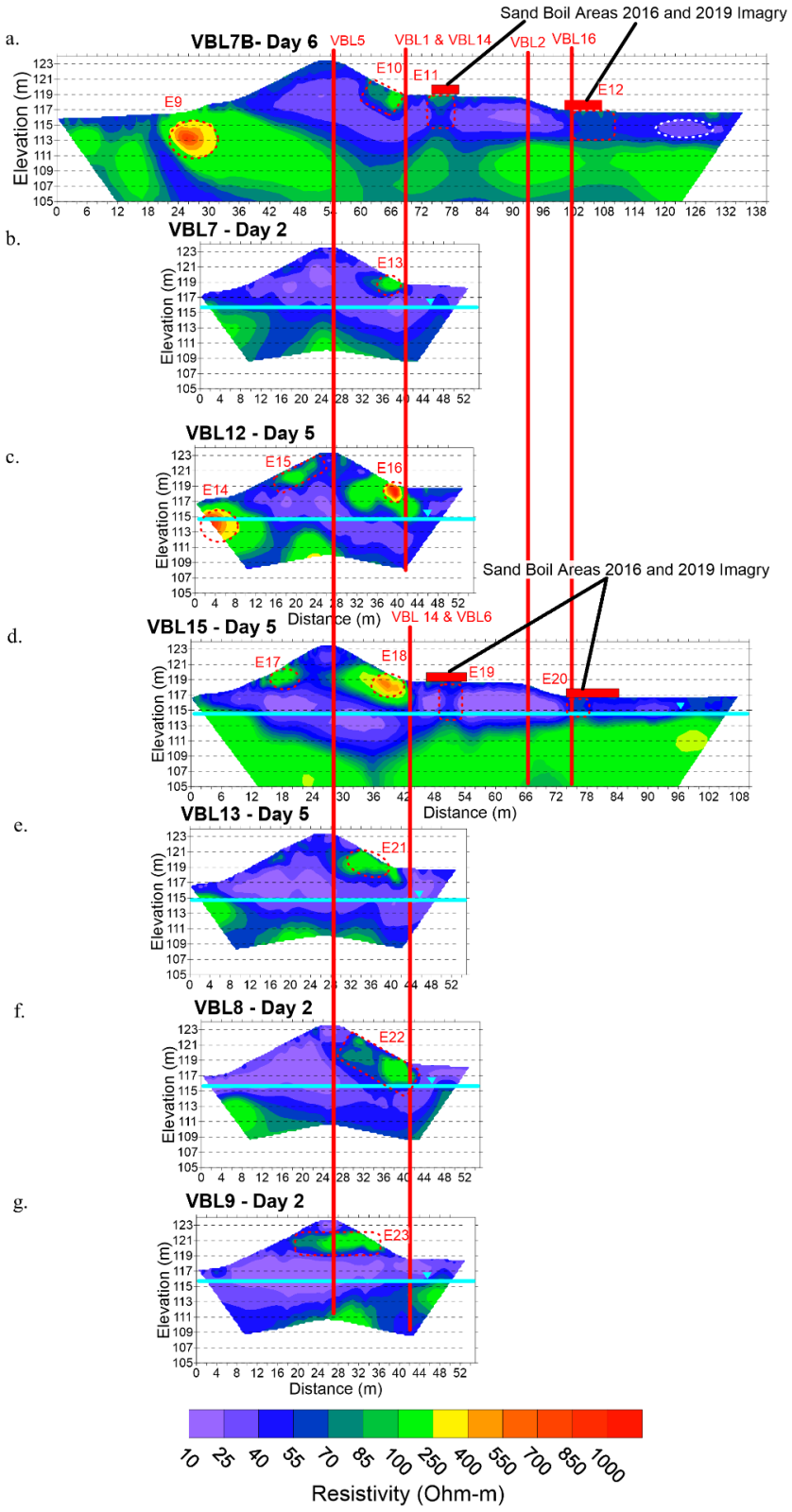

Figure 35 Internal Erosion area transverse DC ERT lines, a) VBL7B, b) VBL7, c) VBL12, d) VBL15, e) VBL13, f) VBL8, g) VBL9

Extended transverse ERT lines using 2 to 2.5 m electrode spacing were collected to evaluate the internal erosion damage further landward of the levee and are shown in Figure 36. Transverse ERT lines VBL7B (Figure 36b) and VBL15 (Figure 36c) were acquired in the internal erosion area and crossed all longitudinal lines. Transverse lines VBL17 (Figure 36a) and VBL18 (Figure 36d) were acquired adjacent to the internal erosion area to serve as control lines where no sand boil activity is evident. As discussed in Section 4.1, there is increased clay content in levee foundation materials and conductive top stratum thickness in the western region of the project site. Therefore, transverse lines VBL17 and VB18 may offer better control lines (i.e., similar geological conditions without internal erosion damage apparent) than the control area DC ERT Lines.

In Figure 36b, transverse line VBL7B is located on the western edge of the 2019 slide and across two areas of sand boil activity, including at the levee toe (prior to seepage berm construction) and along VBL16 (see Figure 16 map). On the riverside false berm of VBL7B, high ER anomaly E9 is present with an ER of 860 ohm-m and with high ER materials reaching the surface. A similar high ER anomaly, E14, is present in the riverside berm of VBL12 (Figure 35c) with an ER of 950 ohm-m. Anomalies E9 and E14 are potentially due to gravel deposits, as a gravel interval was encountered in the bottom of boring F-44F. Additionally, the exposure of aquifer sands due to borrow pit excavation is apparent on the riverside of VBL7B (Figure 36b).

On the landside of VBL7B (Figure 36b), anomaly E11 is present, corresponding to sand boil activity at the base of the 2019 slide. At anomaly E11, both thinning of the top stratum and upward flow of high ER materials are present. It can be observed that if the landslide slope is extended to the base of the seepage berm at an elevation of 117 m, the location of the original landside toe coincides with the area of upward flow in the sand unit at E11. Moreover, the flow of high ER materials upward in E11 aligns with the upward flow of high ER materials at the landside toe of the levee prior to seepage berm construction in VBL7 (Figure 35b), VBL15(E19) (Figure 35c), VBL8 (Figure 35f), and VBL9 (Figure 35g). Anomaly E11 is interpreted to be showing damage to the top stratum, and subsequent piping erosion and flow of aquifer sands to sand boils at the base of the 2019 slide.

Landward of the seepage berm on VBL7B (Figure 36b), anomaly E12 is present and located near sand boils (a sand boil is located 3.5 m west of E12), with minor thinning of the conductive top stratum; however, there is no increase in the elevation of the higher ER material below the anomaly. With transverse line VBL7B alone, it would be difficult to determine if anomaly E12 is a zone of internal erosion damage; However, the location of E12 corresponds to E6 on VBL16 (Figure 34d), which is interpreted to be a zone of internal erosion damage. Collecting perpendicular ERT lines allows for further verification of suspected zones of internal erosion damage. At 118 m along VBL7B, a low ER anomaly is delineated that corresponds to the interpreted swale area that crosses through the internal erosion area.

In Figure 24c transverse line VBL15 is located between the 2019 and 2021 slides with an extension line, VBL19, extending the line by 85 m. High ER anomaly E17 is located on the riverside slope of VBL15 and is similar in extent to E15 on VBL12 (Figure 35c). The cause of these riverside

slope anomalies is unknown; however, they may be due to differences in borrow pit material. High ER anomaly E18 is located on the landside slope of VBL15 (Figure 35d) and coincides with anomaly E4 in landside line VBL6 (Figure 34b). Additionally, landside slope anomalies E16 and E18 on VBL12 (Figure 35c) and VBL15 (Figure 35d), respectively, coincide with anomaly E4 on landside line VBL1/VBL6 (Figure 34b). These anomalies extend below the estimated seepage berm depth and are interpreted as zones of internal erosion damage. Anomalies E19 and E20 on VBL15 (Figure 36c) coincide with sand boil locations, with thinning of the conductive top stratum present and an increase in the elevation of the higher ER unit below the anomalies. These anomalies are interpreted to be zones of internal erosion damage with anomalies E19 and E20, corresponding to the former landside toe and E7 on VBL16 (Figure 34d), respectively. Anomalies E25 and E26 on VBL19 (Figure 36c) have high ER material at the surface and thinning of the top stratum present; however, there is no evidence of sand boil activity or upward flow of the sand unit upwards in the ERT profile at these locations. Additional testing, such as the advancement of soil borings or acquisition of longitudinal geophysical lines through the anomalies, would be required to assess if E25 and E26 are due to internal erosion damage.

Transverse lines VBL17 (Figure 36a) and VBL18 (Figure 36d) were acquired to provide control lines adjacent to the internal erosion area along lines without levee distress features apparent. Line VBL17 is located 100 m east of VBL7B (Figure 36b) in an area with minimal sand boils. A minor high ER anomaly, E24, is present in the landside slope of VBL17 that is attributed to seepage berm construction. On the landside of VBL17, the top stratum thickness is greater than 3 m, and no zones of internal erosion damage were identified. The better performance of the levee at VBL17 can likely be attributed to the prominent ridge deposit crossing the levee at this location and a greater riverside and landside top stratum thickness.

Transverse line VBL18 (Figure 36d) is located 44 m west of VBL9 (Figure 35g) in an area with minimal sand boil activity. On the riverside of VBL18 (Figure 36d), the conductive top stratum is minimally present, and high ER anomaly E27 that connects with the sand unit is present in the riverside false berm. Anomaly E27 is located within the riverside false berm and is attributed to high ER borrow pit materials. High ER anomaly E29 is located at the landside toe prior to seepage berm construction with no top stratum present and upward flow of the sand unit below the anomaly. Anomaly E29 is interpreted as internal erosion damage with minor sand boil activity visible at the former landside toe. Acquisition of longitudinal lines across E29 would be useful for further verifying that the anomaly results from internal erosion damage. The landside top stratum on VBL18, where present, is approximately 3 m thick; however, the top stratum is non-existent at E30 and E31, with high ER materials present at the surface. With VBL18 alone, it is unclear if anomalies E30 and E31 are the result of internal erosion damage to the top stratum or if the anomalies are due to alternating ridge and swale deposits without a conductive top stratum.

The better levee performance at the location of VBL17 (Figure 36a) may be attributed to the point bar ridge deposit underneath the levee at this location. While in the internal erosion area, a swale

deposit in the levee foundation is concentrating sand boil formation and subsequent internal erosion damage at the levee landside toe adjacent to the swale.

The uncertainty in our interpretation of zones of internal erosion damage based on the DC ERT surveys must be considered. The primary sources of uncertainty in our interpretations include the resolution of the DC ERT method, assumptions of 2-D subsurface geometry (i.e., neglecting the effects of 3-D subsurface features and the influence of off axis features on our interpretations), assessment of internal erosion damage at a single site, and a lack of ground-truthing of observed anomalies. The resolution of DC ERT surveys decreases with depth; however, the interpreted zones of internal erosion damage were relatively shallow and loss of resolution with depth is not likely of concern for the project site. In addition to loss of resolution with depth, the width of horizontal influence on a DC ERT survey line increases with depth, which may result in greater horizontal smearing of the resulting ER profiles at depth. Accordingly, due to loss of resolution and greater horizontal width of influence with depth for DC ERT surveys, there is greater uncertainty in interpretation of zones of internal erosion damage at depth (e.g., assessment of internal erosion damage below the levee foundation in longitudinal crest lines or transverse lines).

Assessment of the 3-D internal erosion process with 2-D ERT surveys introduces additional uncertainty into our assessment of zones of internal erosion damage. While the acquisition of perpendicular DC ERT lines provides some insight into the 3-D geometry of observed anomalies, the 2-D surveys operate under the assumption that the subsurface is only variable in two dimensions, without considering the influence of off axis features. For example, in VBL16 (Figure 34d), anomalies E6, E7, and E8 were interpreted to be zones of internal erosion damage. However, it can be observed that the thinning of the conductive top stratum and upward flow of high ER materials is less prominent in anomalies E6 and E7, than in anomaly E8 and these anomalies may be the result of off axis zones of internal erosion damage. Once suspected zones of internal erosion damage are identified in initial DC ERT surveys, multiple parallel lines with reduced electrode spacing could be acquired to reduce the uncertainty in the location of interpreted zones of internal erosion damage (e.g., see Kelley et al., 2019). Alternatively, 3-D DC ERT surveys could be performed to reduce the uncertainty in locating and defining zones of internal erosion damage.

A lack of ground truthing of suspected zones of internal erosion damage represents a significant uncertainty in our interpretations. As discussed above, higher resolution parallel ERT surveys could be performed across interpreted zones of internal erosion damage to target test pits or borings for ground-truthing of the observed anomalies. Test pits advanced during a low water period would likely provide better visualization than borings of the interpreted zones of internal erosion damage. Ground-truthing would help reduce the uncertainty in our interpretations of internal erosion damage zones and verify that the interpreted thinning of the conductive top stratum and upward flow of high ER soils are present. Additionally, similar applications of DC ERT surveying to other sites and subsequent ground-truthing to assess internal erosion damage, would provide further insight into the uncertainty of assessments based on DC ERT surveys.

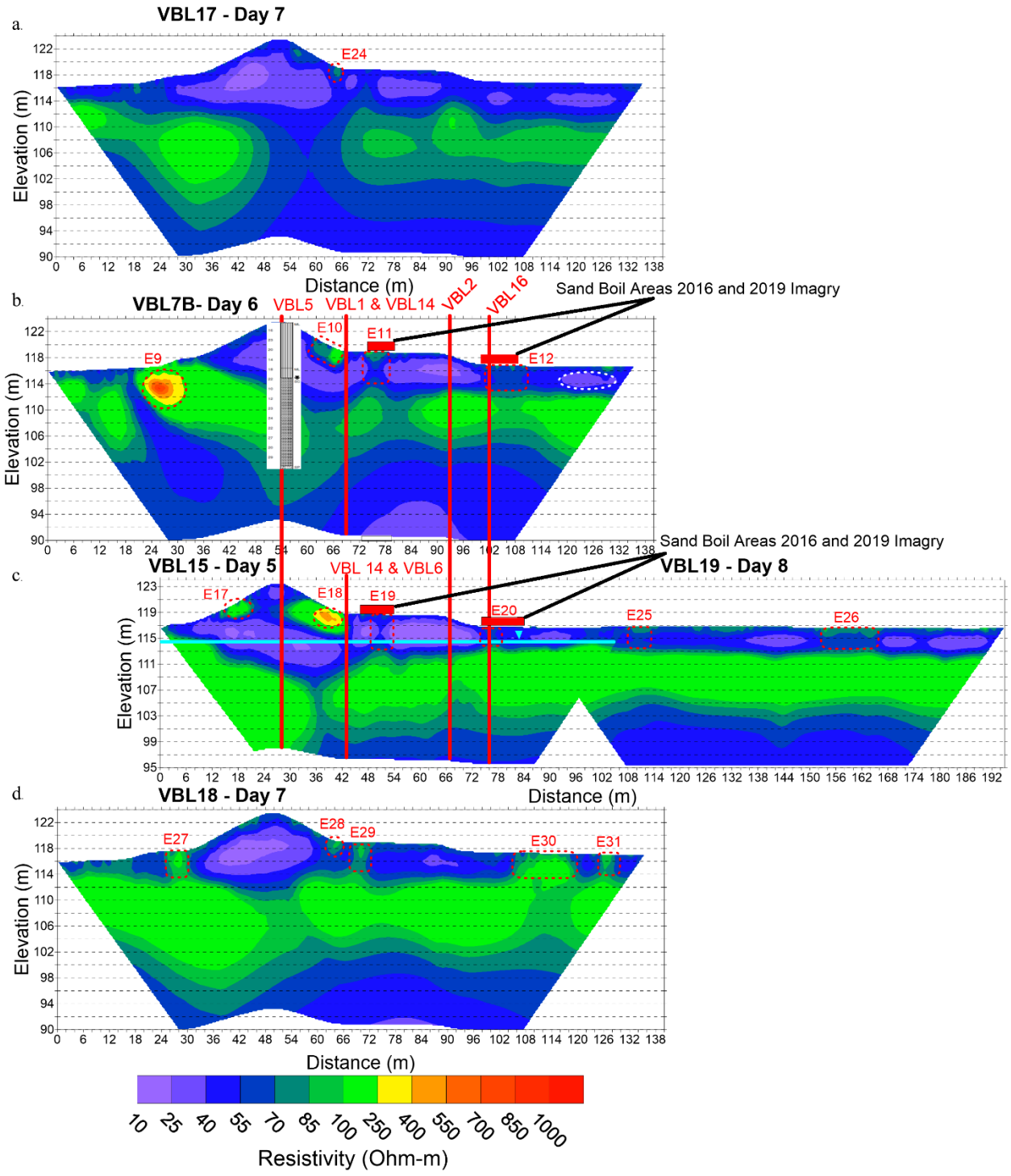

Figure 36 Extended transverse lines in the internal erosion area and surrounding areas, a) VBL17, b) VBL7B, c) VBL15, d) VBL18

4.3.2 Temporal Comparison of Internal Erosion Area DC ERT Lines

The subsurface ER of soils changes naturally with changing soil saturation, soil and groundwater temperature, and groundwater ionic concentration (Rein et al., 2004). Of the factors above, changing soil saturation (due to fluctuating groundwater levels and in the vadose zone) and changing soil and groundwater temperatures (in the near-surface) were considered when interpreting temporal changes in ER. To understand if these changes are influencing the results of the study, a repeat seasonal DC ERT survey was acquired to evaluate high ER anomalies and suspected zones of internal erosion damage in the internal erosion and control areas. In the internal erosion area, a repeat ERT survey of VBL1/VBL6 was performed with VBL14 on the levee landside. In the control area, a repeat (and extended) survey of transverse line VBL11 was performed with VBL11B.

The groundwater elevation as measured in the B-23 piezometer (when measured), cumulative precipitation from the USGS precipitation gauge at the James W. Trimble Lock and Dam near Van Buren, AR, during the project duration, and the date of each field day are plotted in Figure 37. Line VBL1, VBL6, and VBL14 were collected on days one, two, and five, respectively. The groundwater elevation decreased by 1 m from day two to day five, which is consistent with observations of standing water present on days one and two on the riverside of the internal erosion area and not on day five (Figure 37). There was increased precipitation between day one and day two and between day two and day five. Lines VBL1/VBL6 and VBL14 were acquired in the dry summer and wet winter seasons, respectively. Additionally, when considering the temporal changes in the near-surface ER, the effects of surface temperatures and the seepage berm construction process must be considered (e.g., the compaction and hydration of seepage berm materials).

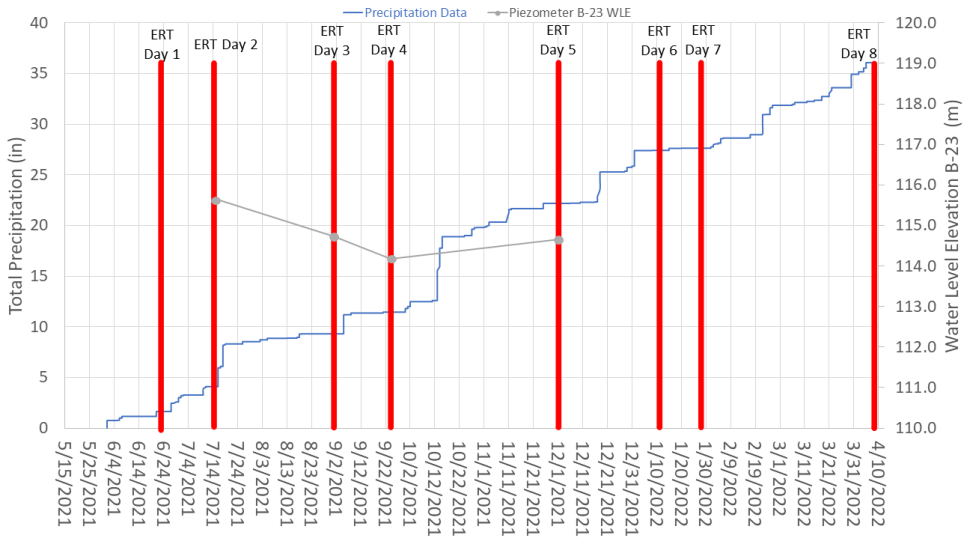

Figure 37 Precipitation data from the USGS precipitation gauge at the James W. Trimble Lock and Dam (AR River at James W. Trimble L&D Nr Van Buren, AR, n.d.) and measured water level elevations from the B-23 piezometer. The date of each field day is shown with a red bar labeled with the day of testing number as specified in Table 2. The CCR data were acquired on September 21, 2022, under similar conditions to VBL10 (collected on ERT Day 4).

In Figure 38, the overlapping lines VBL1/VBL6 and VBL14 (where repeat seasonal DC ERT surveys were performed), and the associated percent difference in ER between VBL1/VBL6 (Figure 39a) and VBL14 (Figure 38b and c) are presented. In Figure 38a and b, the high ER anomalies in VBL1/VBL6 and VBL14 are delineated with dashed and solid red lines, respectively. Figure 38c is a zoomed in version of Figure 38b to match the area surveyed in Figure 38a. As previously discussed, anomalies E3 and E5 were attributed to seepage berm construction, and E4 was interpreted to be the result of internal erosion damage (Figure 38a, b, c). In landside line VBL14, high ER anomaly E32 is present with a similar lateral extent and a larger vertical extent than E4. As can be observed in Figure 35, anomaly E32 coincides with anomalies E16 in VBL12 (Figure 35c) and E18 in VBL15 (Figure 35d). Additionally, the increased depth of the eastern edge of E32 in VBL14 (Figure 38b and c) is consistent with E16 on transverse line VBL12 (Figure 35c). Anomalies E4 and E32 extend well below the seepage berm extent and are interpreted as internal erosion damage related to the 2019 slope failure.

In Figure 38d, the resistivity difference between VBL1/VBL6 and VBL14 indicate the shallow anomalies E3, E4, and E5 in VBL1/VBL6 are primarily decreasing in ER from the dry season to the wet season. Additionally, these high ER anomalies show a greater decrease in ER than in surrounding areas, with a decrease in ER of up to 67 percent. This is likely due to increased precipitation and saturation levels in the vadose zone prior to the acquisition of VBL14 and the higher permeability of anomalies. Below the base of the seepage berm (estimated at 117 m), ER primarily remained stable or increased from VBL1/VBL6 to VBL14, with zones of increasing ER concentrated between elevations of 117 m to 113 m. The increase in ER is attributed to decreasing water level elevation between the collection of VBL1/VBL6 and VBL14 (decreasing from 115.7m to 114.7m between the surveys). Additionally, the VBL1/VBL6 survey utilized a 1 m electrode spacing and the VBL14 surveys utilized a 2 m electrode spacing; accordingly, resolution differences between the surveys may have a role in the observed changes in ER.

The acquisition of repeat seasonal ERT surveys allows observation of how suspected zones of internal erosion damage respond to changing subsurface conditions. For example, in Figure 38d, in the eastern zone of anomaly E32, increases in ER of up to 235 percent were observed between acquisition of VBL1/VBL6 and VBL14. The greater increase in ER in the lower eastern end of E32 may be due to the lowering of groundwater levels and less capillary fringe in a zone of internal erosion damage than surrounding fine-grained soils. The temporal response of anomaly E4/E32 further supports the presence of a zone of internal erosion damage leading to the sand boils present at the landside toe near the 2019 slide. However, with the water level elevation measured at 114.7 m on the levee crest on the day VBL14 was acquired, the ER in anomaly E32 is increasing below the groundwater level elevation. The increasing ER of anomaly E32 below the groundwater elevation may be the result of a higher permeability (and relatively free draining) internal erosion damage zone locally lowering groundwater elevations. Advancement of a test pit at the location of anomaly E4/E32, would reduce the uncertainties associated with resolution differences between the surveys and verify the interpreted zone of internal erosion damage.

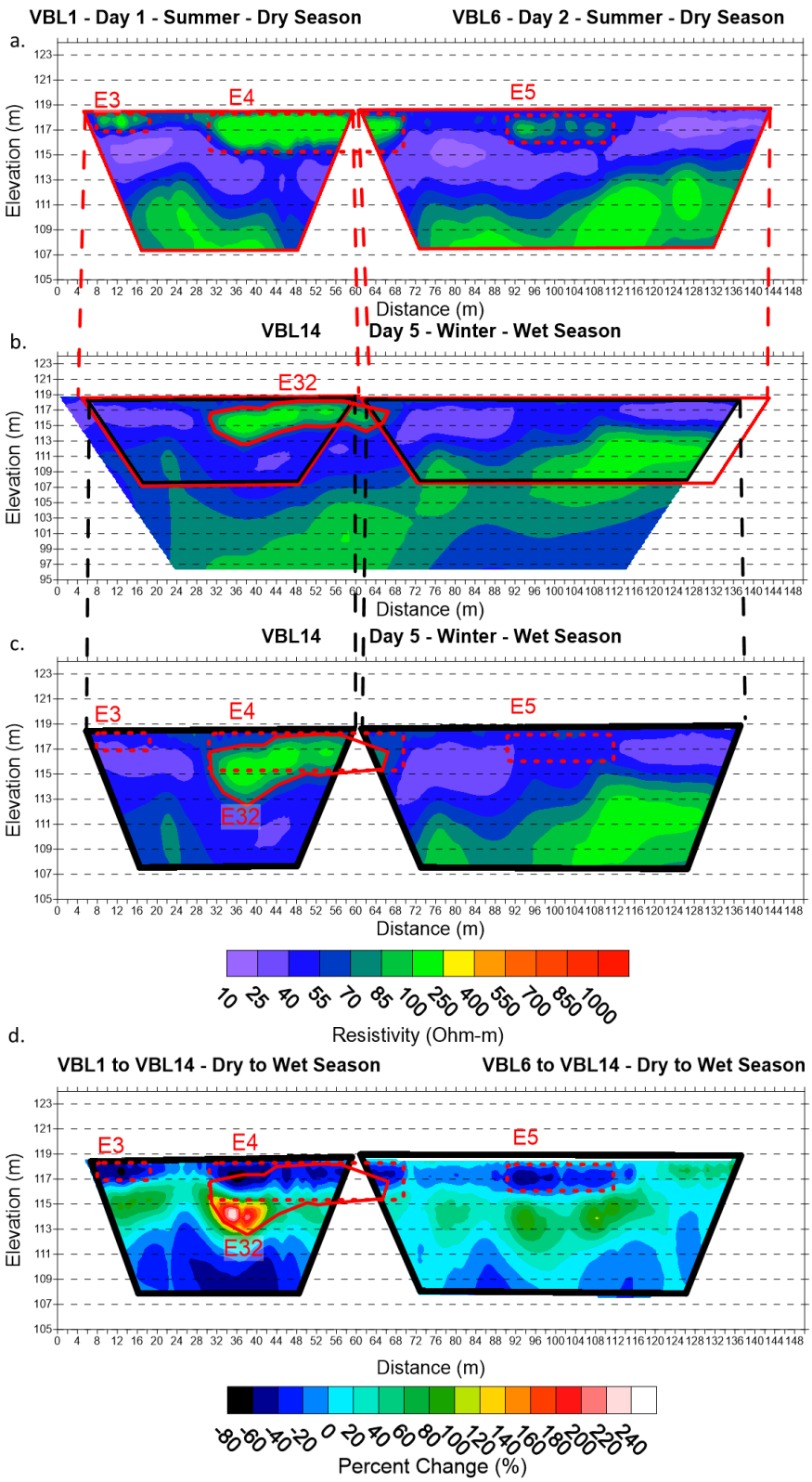

Figure 38 Temporal comparison of VBL1/VBL6 and VBL14, a) VBL1/VBL6, b) VBL14, c) zoomed in extent of VBL14 overlap with VBL1/VBL6 d) percent change from VBL1/VBL6 (dry season) to VBL14 (wet season)

4.3.3 Internal Erosion Area Co-located MASW and DC ERT Lines

Co-located MASW and DC ERT lines were collected along the landside and levee crest of the internal erosion area and are presented in Figures 39 and 40, respectively. For the co-located MASW and DC ERT lines, annotations include the 2019 and 2021 slide locations, the groundwater elevation were measured, high ER anomalies (annotated with red dashed lines), and low Vs anomalies (annotated with white dashed lines). MASW Line A (top) and DC ERT line VBL14 (bottom) are co-located along the landside of the internal erosion area and are presented along with satellite imagery (middle) in Figure 39. In general, there was difficulty in discerning the stratigraphy based on the Vs profiles alone. Boring B-23 is aligned with MASW Line A for comparison of Vs and stratigraphy. The transition from the seepage berm material (extending to an elevation of approximately 117m) and the silt top stratum material to sandy soils approximately coincides with the 180 m/s Vs contour. In MASW Line A, a velocity inversion and low Vs anomaly S1 are present from 0 to 16 m at an elevation of 115 m to 113 m. The cause of low velocity anomaly S1 is uncertain, with the anomaly outside the extent of any ERT testing. Additionally, low velocity zone S2, which coincides with high ER anomaly E32 in VBL14, is present between the 2019 and 2021 slides. As previously discussed, anomaly E32 is interpreted as a zone of internal erosion damage related to the 2019 slope failure. The presence of co-located low Vs anomaly S2 and high ER anomaly E32 further supports that internal erosion damage is present at this location. Additionally, transverse lines VBL12 (Figure 35c) and VBL15 (Figure 35d) cross low Vs anomaly S2 with corresponding high ER anomalies, E16 and E18, respectively.

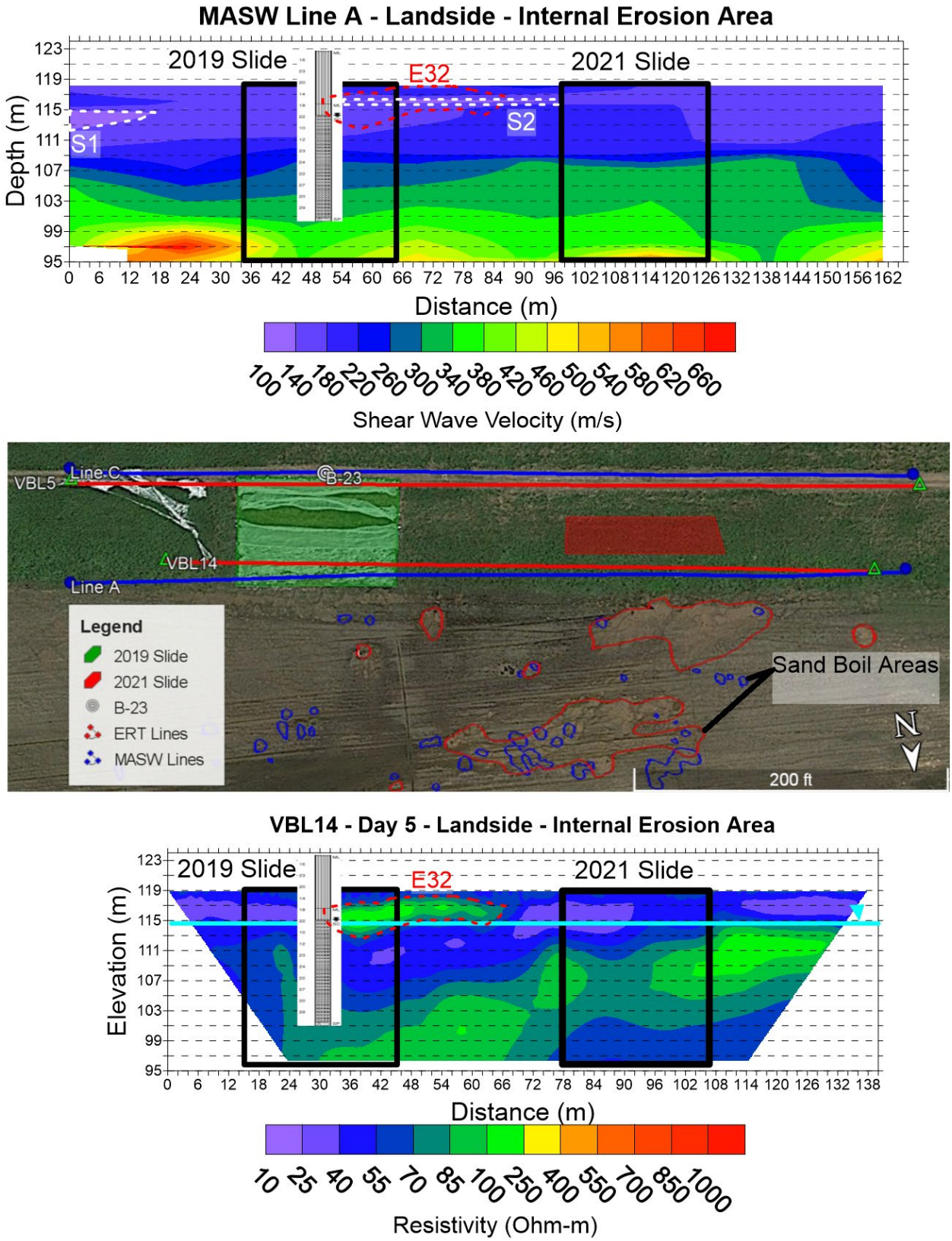

Figure 39 Comparison of co-located internal erosion area DC ERT and MASW landside lines

In Figure 40, MASW Line C (top) and DC ERT line VBL5 (bottom) are co-located along the crest of the internal erosion area along with an aerial image of the area (middle). In MASW Line C, a low Vs layer is present at the levee crest extending to a depth of approximately 2.5 meters below the levee crest. The low Vs of the levee crest may be the result of desiccation cracking of the crest under dry summer conditions. Additionally, a velocity inversion and low Vs anomaly, S3, is present in MASW Line C from 0 to 112 meters at an elevation of 115 to 119 meters. Low Vs anomaly S3 is located at the approximate elevation of the levee foundation (estimated to be 117 meters) and crosses the 2019 and 2021 slide areas and high ER anomaly E1 (Figure 32).

Looking back at VBL5 (Figure 34a), high ER anomaly E1 coincides with anomaly E4 in the longitudinal seepage berm ERT lines VBL1/VBL6 (Figure 34b) which was interpreted as a zone of internal erosion damage. In Figure 40, the location of low Vs anomaly S3 coincides with low ER materials of the levee foundation present in the transverse ERT lines (Figure 35), that are attributed to the conductive top stratum of the point bar deposits. In Figure 40, at 80 m along the MASW Line C Vs profile, there is an increase in the elevation of low Vs anomaly S3 that coincides with the interpreted swale area (i.e., the saturated area in Figure 40). The internal erosion damage apparent to the west of the interpreted swale area and in the upward movement of high ER materials in transverse lines VBL8 and VBL9 (Figure 35f and g) was not resolved in the MASW Line C Vs profile (Figure 40). Additionally, zones of internal erosion damage were not resolved below anomaly S3 or in the levee foundation. In both the DC ERT lines and MASW Lines, the geophysical signature of internal erosion damage (i.e., increased ER and decreased Vs) was more readily resolved along the levee landside. In the backwards erosion piping process, piping erosion propagates from the levee landside to the riverside; therefore, internal erosion damage that is more readily resolvable using geophysical methods may be more likely to be present on the landside of the levee. While the MASW surveys provided additional insight into the stratigraphy of the internal erosion areas, no zones of internal erosion damage were identified that were not already identified in the DC ERT lines.

Sources of uncertainty in our interpretation of zones of internal erosion damage based on the MASW surveys must be considered. Some sources of uncertainty in our interpretations for the MASW surveys include the resolution of the MASW method, a lack of ground-truthing of the geophysical surveys, and application of the method to a single site. The horizontal resolution for MASW surveys is generally taken as 10-50 percent of the array length, which is equal to 2.4 meters for this study. However, this depends significantly on the impedance between various materials in the subsurface. The vertical resolution for MASW surveys is generally taken as twice the receiver spacing, which is equal to 2 meters for this study. Additionally, the resolution of the MASW method decreases with depth resulting in greater uncertainty in the resulting Vs profiles at depth (Foti et al., 2015). For this study, the MASW landstreamer setups were spaced at 11.5 meters apart, which significantly reduces the working resolution of the 2-D Vs profiles. Decreasing the spacing of landstreamer setups would increase the resolution of the resulting 2-D Vs profiles and decrease

the uncertainty of the location and depth of interpreted zones of internal erosion damage. As previously discussed, the lack of ground-truthing of geophysical data was a significant source of uncertainty for assessment of internal erosion damage, for both the MASW and DC ERT surveys. Targeting of test pits and further application of the methods of this study, as described in Section 4.3.1, would reduce the uncertainty in our interpretations of zones of internal erosion damage.

The results of a combination of CCR, DC ERT, and MASW geophysical surveying support that internal erosion damage can be assessed using geophysical methods. However, further geophysical testing at the project site, ground-truthing of interpreted zones of internal erosion damage, and application of the methods of this study to other project sites is needed to understand the uncertainties associated with geophysical assessment of internal erosion damage in levees and the applicability of these results to other sites. The use of preliminary CCR surveys in combination with a review of satellite and aerial imagery and historical boring logs was valuable for targeting further geophysical testing. The CCR method provides a rapid and continuous assessment of subsurface conditions to identify potential areas of internal erosion damage for further geophysical surveying. A combination of transverse and longitudinal DC ERT lines was valuable in identifying potential zones of internal erosion damage. Potential zones of internal erosion damage in the DC ERT lines were characterized by high ER, thinning of the conductive top stratum, upward flow of high ER soils, and typically sand boils present at the surface in satellite imagery. Often perpendicular DC ERT lines across a suspected zone of internal erosion damage were required to support that a given high ER anomaly potentially resulted from internal erosion damage. DC ERT surveying identified zones of potential internal erosion damage that would not be correctly located with visual methods alone due to surficial agricultural processes and overlapping deposits of sand boil ejecta (e.g., internal erosion damage along VBL16). Repeat DC ERT surveys provided further information on suspected zones of internal erosion damage by allowing observation of the anomaly response to seasonal changes. Repeat DC ERT surveys provided further support of potential internal erosion damage on the landside toe of the internal erosion area. The MASW lines provided further support of potential internal erosion damage at the toe line of the levee; however, MASW surveying was unsuccessful in identifying any zones of internal erosion damage not already identified in the DC ERT lines. The use of transverse and longitudinal DC ERT surveys for assessment of internal erosion damage in levees is recommended over MASW based on the results in the internal erosion area. The DC ERT surveys were more effective for detailed mapping and assessment of internal erosion damage and the processing of ERT data is less complex and time intensive than processing of MASW data. However, decreasing the spacing of MASW landstreamer setups should be considered for future studies to obtain higher resolution 2-D Vs profiles. If limited time and resources are available to assess internal erosion damage at a given site, an initial review of aerial imagery followed by acquisition of targeted perpendicular longitudinal landside and extended transverse DC ERT lines is recommended.

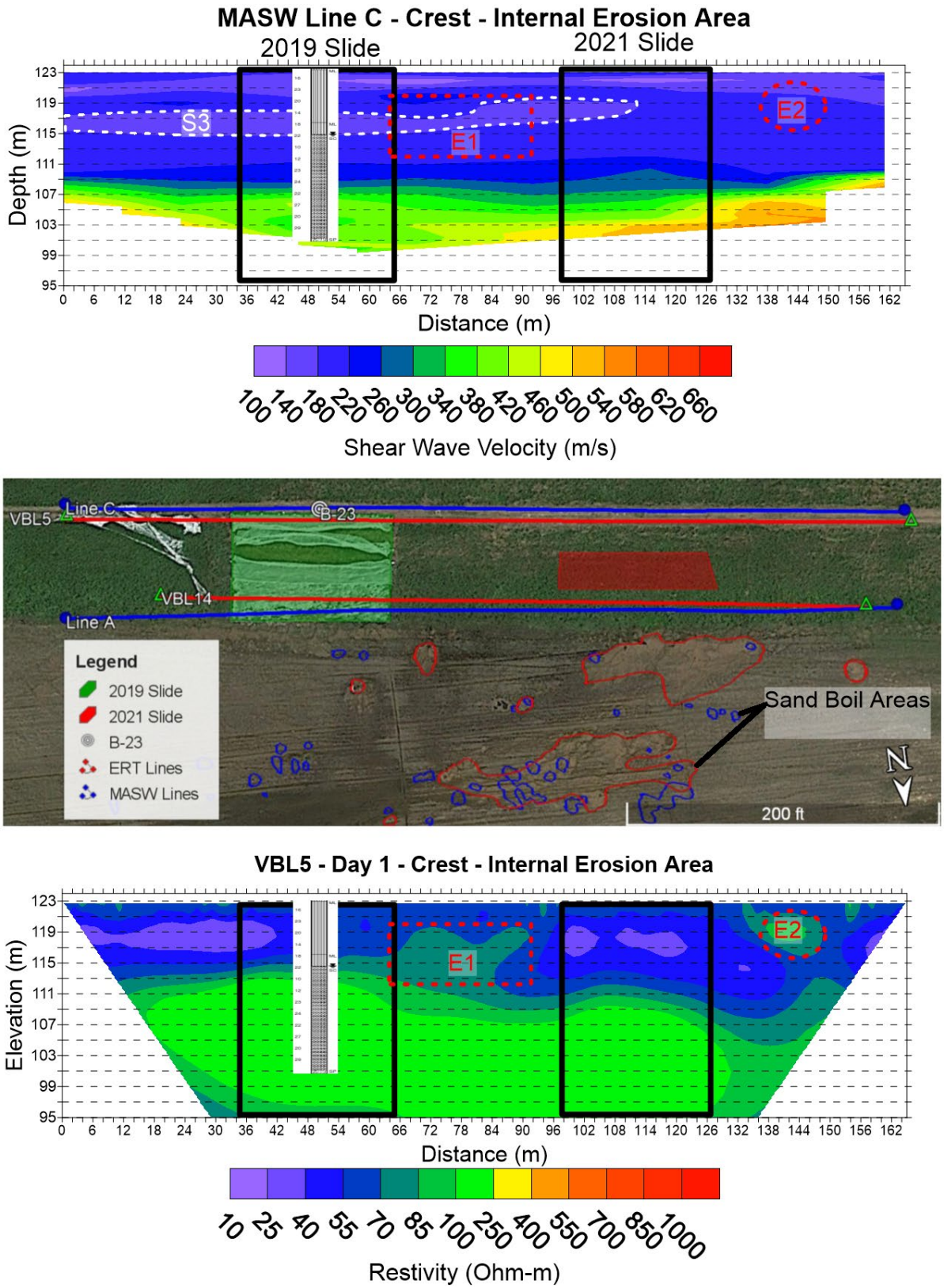

Figure 40 Comparison of co-located internal erosion area DC ERT and MASW crest lines

4.4 Research on the Control Area

4.4.1 Control Area

The control area was selected along a levee section without significant levee distress features associated with internal erosion damage (e.g., heavy sand boil activity and slope stability failures) or significant damage during the 2019 flooding for comparison with the internal erosion area (Figure 15). Two relief wells are present in the western section of the project site, including one in the control area, located at approximately 115 m along and 5 m to the west of transverse DC ERT Line VBL11B (Figure 21). It is unclear if these relief wells are functional as they have not been addressed in inspection reports or during the 2009 levee certification study of the Van Buren Levee District No. 1/Crawford County Levee District. The geophysical testing in the internal erosion area included longitudinal crest and landside DC ERT lines, transverse DC ERT lines, and crest and landside MASW lines. First, the DC ERT results will be discussed, followed by a discussion of co-located DC ERT lines and MASW lines and a comparison of the internal erosion area and control area lines. The DC ERT lines in the control area are presented in Figure 41. Longitudinal line VBL4, located to the west of the internal erosion area on the existing seepage berm, is presented in the appendices (Appendix A-4). All control area figures are aligned from east to west for longitudinal lines and south to north for transverse lines (i.e., from riverside to land side). The control area DC ERT lines were annotated in the same manner and using the same criteria for anomalies as the internal erosion area. The same classification of soil type based on ER applied to the internal erosion was applied to the control area, with ER values greater than 70 ohm-m corresponding to sandy soils and ER values less than 70 ohm-m corresponding to silts and clays.

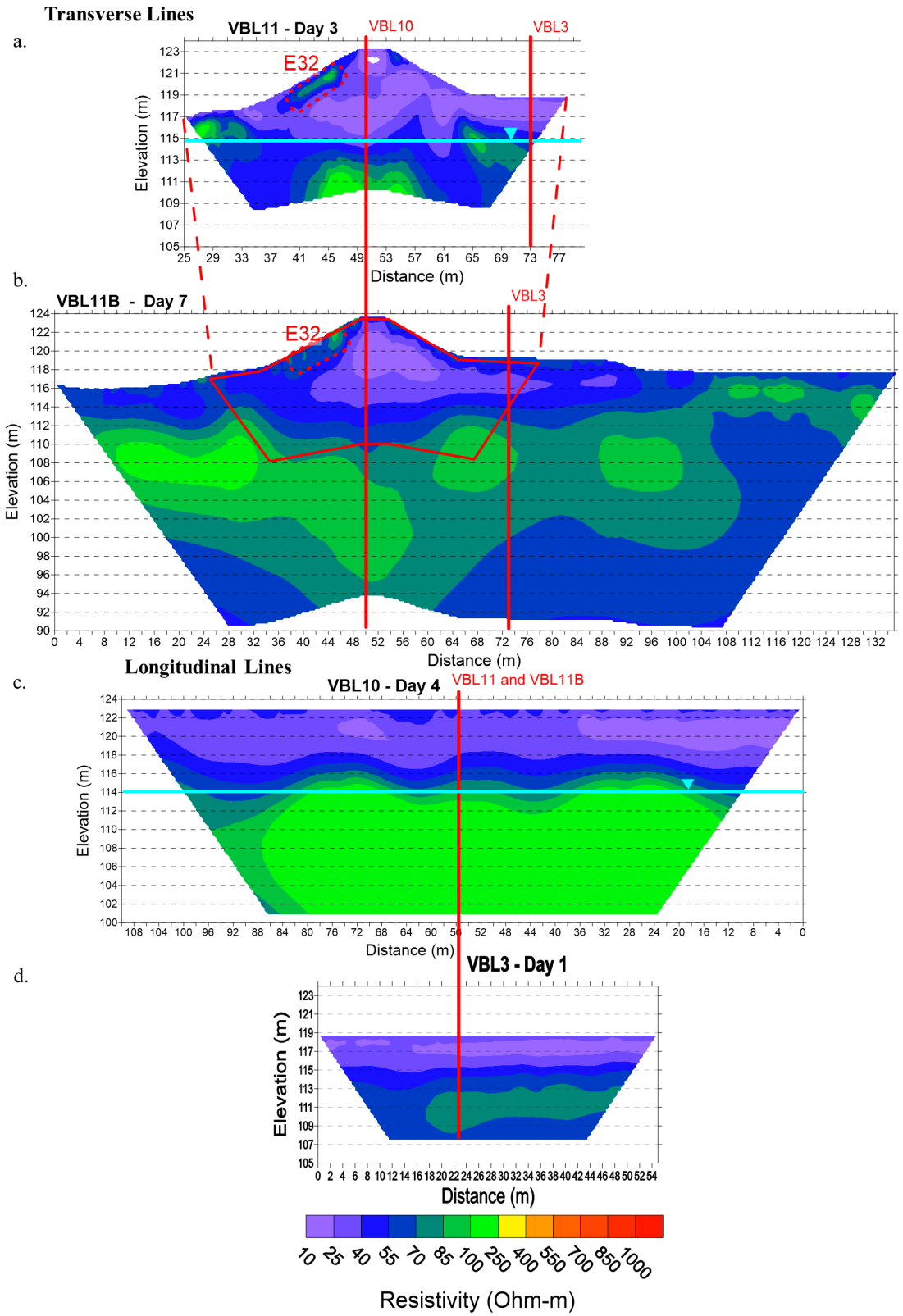

Figure 41 Transverse and longitudinal control area DC ERT lines, a) VBL11, b) VBL11b shown with overlap of VBL11, c) VBL10, and d) VBL3

Partially overlapping DC ERT lines VBL11 (Figure 41a) and VBL11B (41b) were collected to assess temporal change in ER in the control area. Additionally, VBL11B was collected as an extension of VBL11 for comparison with the extended internal erosion area transverse lines. No levee distress features related to internal erosion damage were observed along VBL11 or VBL11B in a review of satellite imagery or the USACE assessment of the 2019 flood damage. High ER anomaly E32 on the riverside slope is present in both VBL11 and VBL11B; The cause of high ER anomaly E32 is uncertain, and the anomaly is likely due to differences in borrow pit material. Notably, no upwelling of high ER soils or thinning of the conductive top stratum is present on the landside toe of VBL11 or VBL11B, as was observed in interpreted areas of internal erosion damage (e.g., E11 located at the landside toe of VBL7B in Figure 35a) in the internal erosion area.

In Figure 41, no high ER anomalies were observed in longitudinal DC ERT lines VBL10 (Figure 41c) or VBL3 (Figure 41d) located on the crest and landside toe of the control area, respectively. In crest line VBL10, the slight undulation of the contact between low ER materials and high ER materials is present, which could be interpreted as areas of upwelling high ER material; however, there is no corresponding upwelling of high ER material in perpendicular lines VBL11 or VBL11B. The undulations in the contact between the low ER materials and high ER materials in VBL10 may be due to the ridge and swale topography of the point bar deposits. For example, the increased thickness of low ER materials at 90 m on VBL10 corresponds well to an area interpreted as a clay-filled trough in the landside CCR data at 950 m (Figure 32).

In Figure 42, a comparison of longitudinal toe line VBL3 (bottom) of the control area with the internal erosion area longitudinal toe lines VBL1/VBL6 (top) is presented. The conductive top stratum is more continuous in the control area. Additionally, there is no thinning of the conductive top stratum present in VBL3, as was observed in areas of interpreted internal erosion damage in VBL1/VBL6 at high ER anomaly E4.

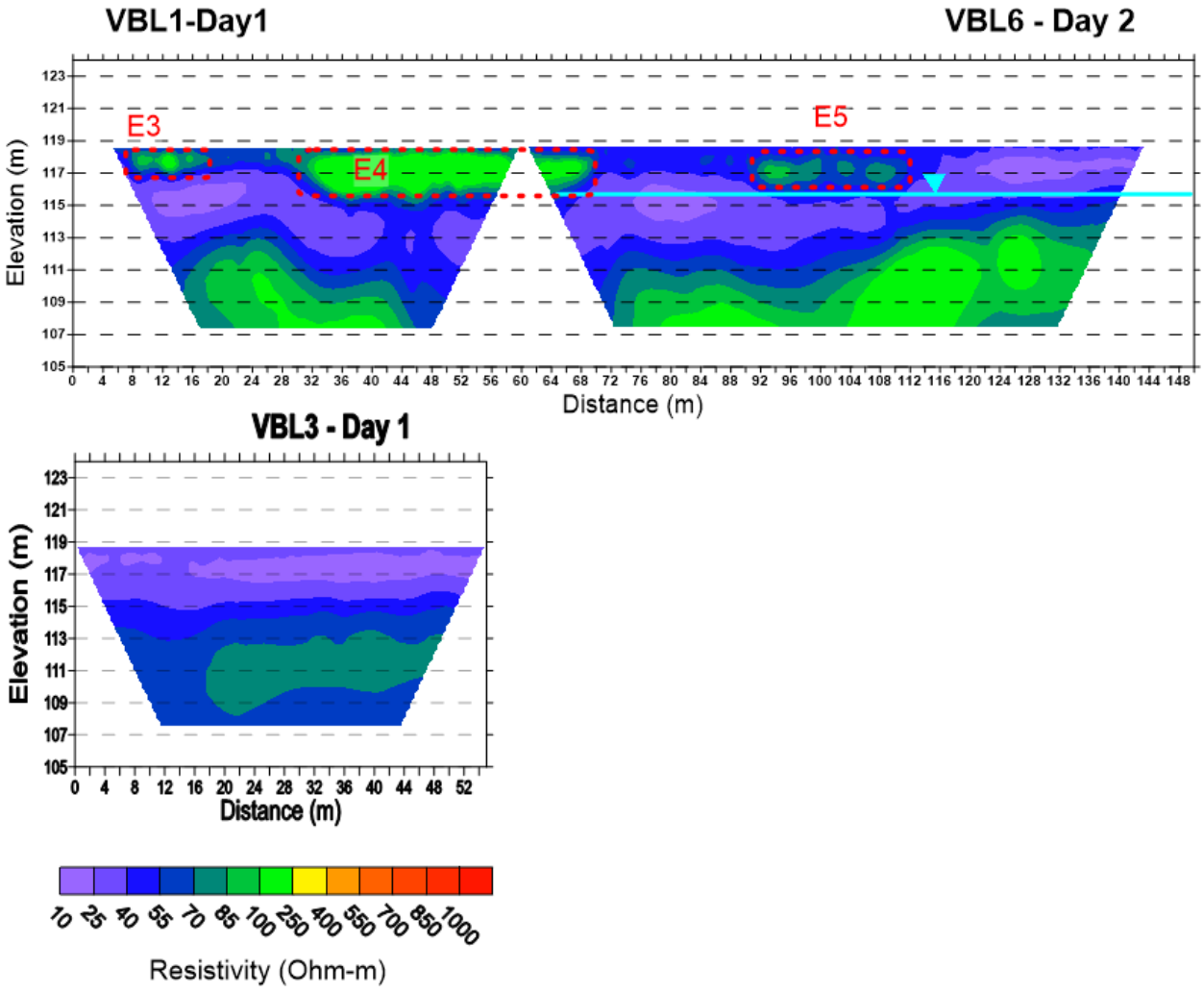

Figure 42 Comparison of select longitudinal internal erosion (top) and control area (bottom) DC ERT lines

A comparison of transverse lines VBL7B (43a), VBL12 (43b), and VBL15(43c) in the internal erosion area and control area transverse line VBL11B (Figure 43d) is presented below. There is a greater top stratum thickness present in the riverside slope of VBL11B than present in many of the internal erosion transverse lines (e.g., VBL7B and VBL15). The decreased riverside top stratum thickness is due to the excavation of borrow pits directly adjacent to the riverside slope of the internal erosion area. The presence of borrow pits directly adjacent to the internal erosion area leads to the formation of high hydraulic gradients across the levee during high water events and is likely a contributing factor to the poor levee performance in the internal erosion area. On the landside toe of VBL11B (Figure 43d), no thinning of conductive top stratum or upward flow of high ER materials is present, as was observed in interpreted zones of internal erosion damage (e.g., E16 on VBL12 (Figure 43b) and E18 on VBL15 (Figure 43c)).

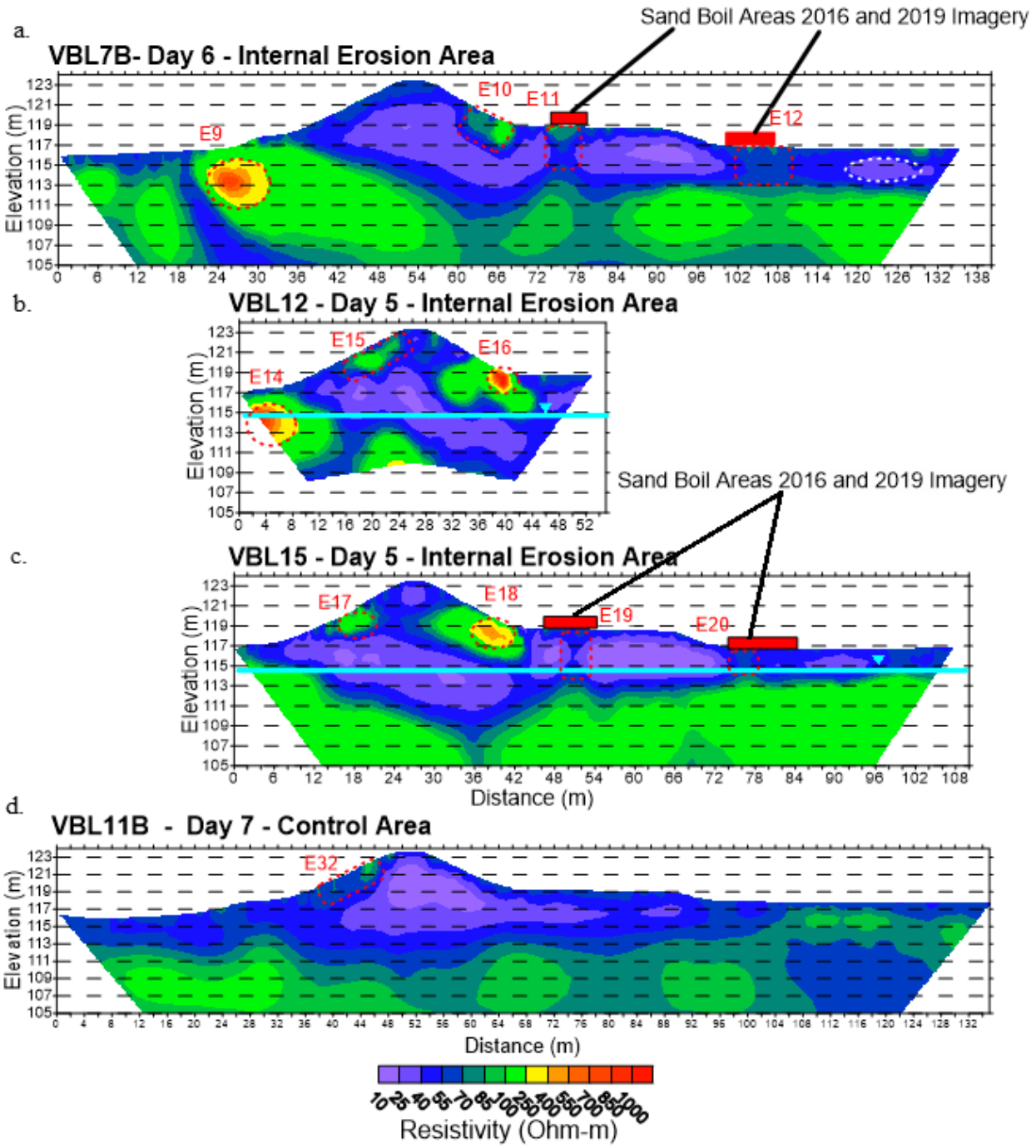

Figure 43 Comparison of select transverse internal erosion area (VBL7B, VBL12, and VBL15) and control area (VBL11b) DC ERT Lines, a) VBL7B, b) VBL12B, c) VBL15, and d) VBL11B

4.4.2 Temporal Comparison of Control Area DC ERT Lines

In Figure 44, the overlapping lines VBL11 and VBL11B (where repeat seasonal DC ERT surveys were performed), and the associated percent difference in ER between VBL11 (Figure 44a) and VBL11B (Figure 44b and c) are presented. In Figure 44a and c, the location of high ER anomaly E32 in VBL11 is delineated with dashed red lines. Figure 44c is a zoomed in version of Figure

44b to match the area surveyed in Figure 44a. Line VBL11 was collected in the dry summer season, and VBL11B was collected in the wet winter season. The ER of seepage berm materials increased by greater than 150 percent between the collection of VBL11 and VBL11B (Figure 44d). The increasing ER of seepage berm materials and near-surface soils (e.g., the levee crest) can likely be attributed to decreased soil temperatures between the collection VBL11 and VBL11B. The ER decreased in most of the levee and foundation materials between the collection of VBL11 and VBL11B (Figure 44d). This decrease in ER can likely be attributed to increasing groundwater elevation and vadose zone saturation levels during the wet season. The consistent response of high ER anomaly E32 to changing surface temperatures and saturation levels further supports the interpretation of the anomaly resulting from material differences. The acquisition of repeat seasonal DC ERT surveys was valuable for evaluating high ER anomalies and suspected zones of internal erosion damage at both the internal erosion and control areas.

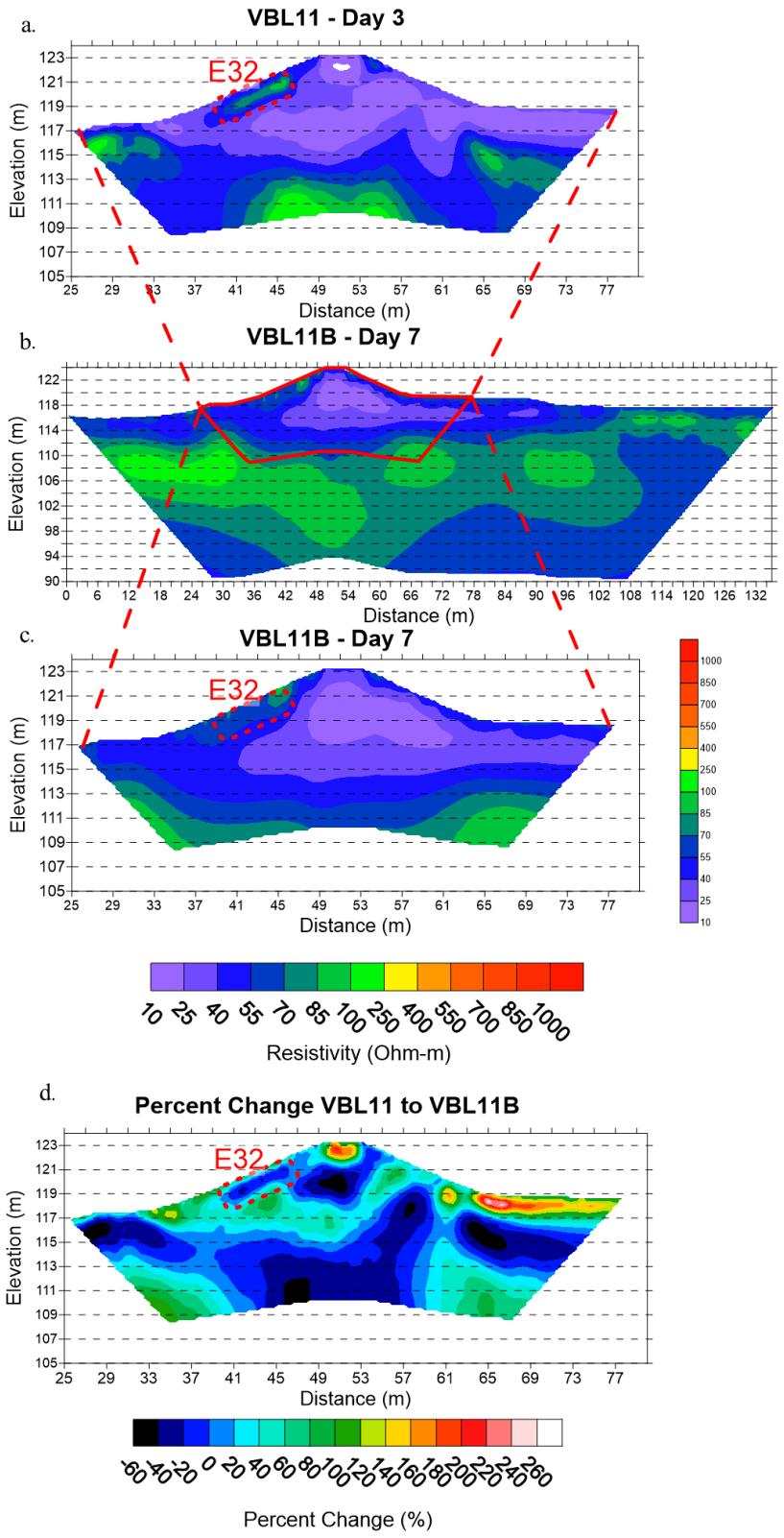

Figure 44 Temporal comparison of VBL11 and VBL11B, a) VBL11, b) VBL11B, c) zoomed in extent of VBL11B overlap with VBL11 d) percent change from VBL11(dry season) to VBL11b (wet season)

4.4.3 Control Area Co-Located MASW and DC ERT Lines

Co-located MASW and DC ERT lines were collected along the crest, and landside of the control area and are presented in Figures 45 and 46, respectively. The co-located MASW and DC ERT lines for the control lines were annotated in the same manner as the internal erosion area. Additionally, the projected location of historical boring F44C5 is included for comparison of Vs/ER and stratigraphy.

MASW Line B (top) and DC ERT Line VBL3 (bottom) are co-located along the landside of the control area and are presented aligned with satellite imagery (middle) in Figure 45. Comparing MASW Line B with historical boring F44C5, discerning the stratigraphy based on the Vs profile is difficult. The transition from seepage berm materials to native soils coincides with the 140 m/s contour at an elevation of approximately 117 m (Figure 45). Landside DC ERT Line VBL3 more effectively resolves the transition from near-surface silty clay and sandy silt to sand than MASW Line B (Figure 45). No high ER or low Vs anomalies of interest are present in the landside of the control area, which is consistent with the lack of levee distress features observed in the area.

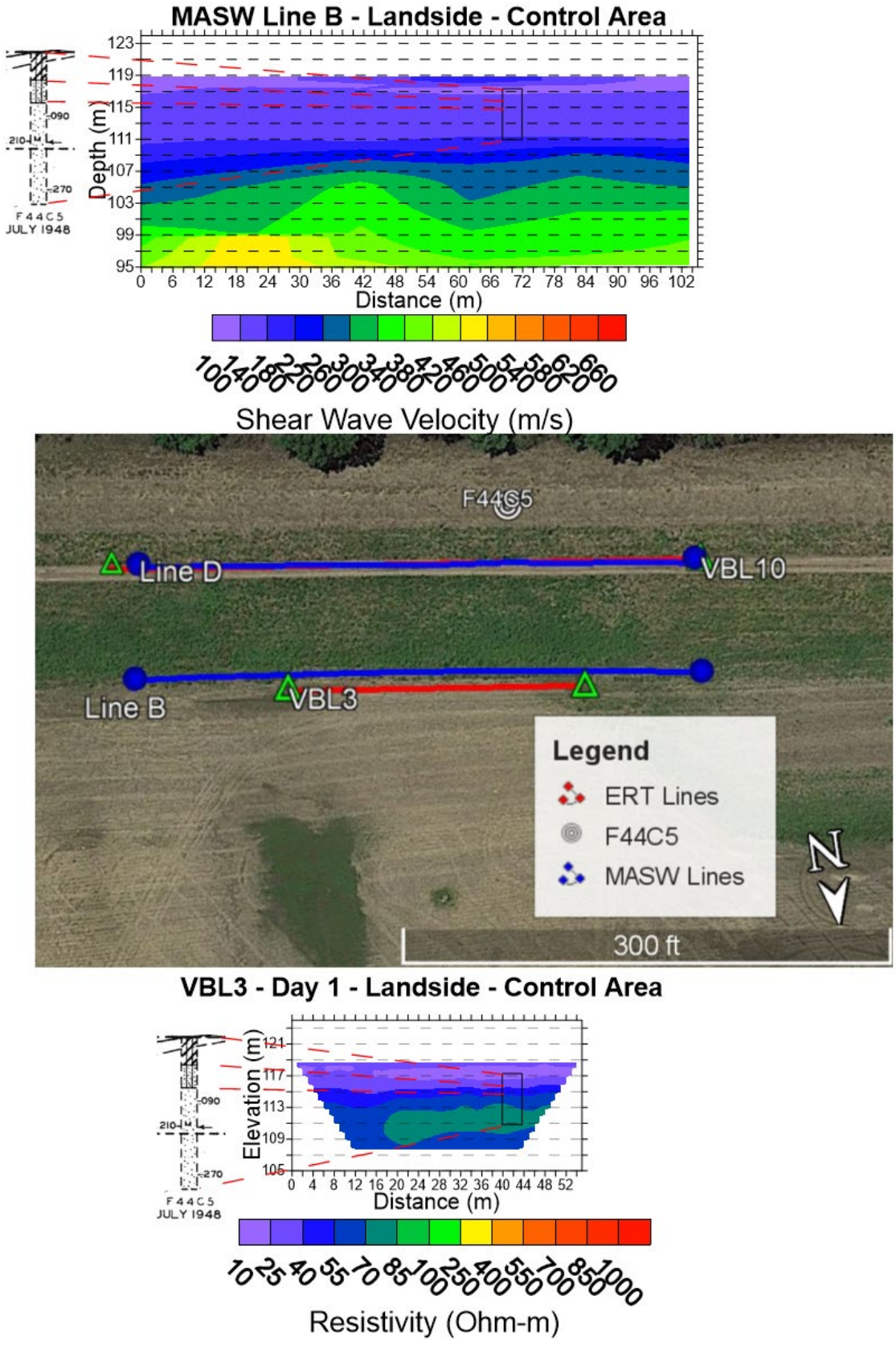

Figure 45 Comparison of co-located control area DC ERT and MASW landside lines

MASW Line D (top) and DC ERT Line VBL10 (bottom) are co-located along the crest of the control area and are presented aligned with satellite imagery (middle) in Figure 46. Comparing historical boring F44C5 with MASW Line D, the Vs profile resolves the transition from near-surface silty clay and sandy silt to sand more effectively than landside line MASW Line B (Figure 46). The transition from fine-grained soil to sand corresponds approximately to the 220 to 180 m/s contour at an elevation of 114 m in MASW Line D. The MASW Line D Vs profile agrees well with DC ERT line VBL10, with the interpreted contact between fine-grained soils (of the levee body and conductive top stratum) and sands varying from approximately 113 m to 117 m in elevation in VBL10 (Figure 46). Low Vs anomaly S4 is present in the levee foundation materials from approximately 0 to 10 m along MASW Line D; however, there is no corresponding high ER anomaly in DC ERT Line VBL10 or observed levee distress features in the satellite imagery. Accordingly, low Vs anomaly S4 is not interpreted as a zone of internal erosion damage and is likely a clay-filled swale crossing underneath the levee. Low Vs anomaly S4 coincides with a trough of low ER material in VBL10 in the levee foundation, which further supports the interpretation of a clay-filled swale crossing the levee at this location. Additionally, satellite imagery supports this interpretation with differences in vegetation apparent in the suspected trough area.

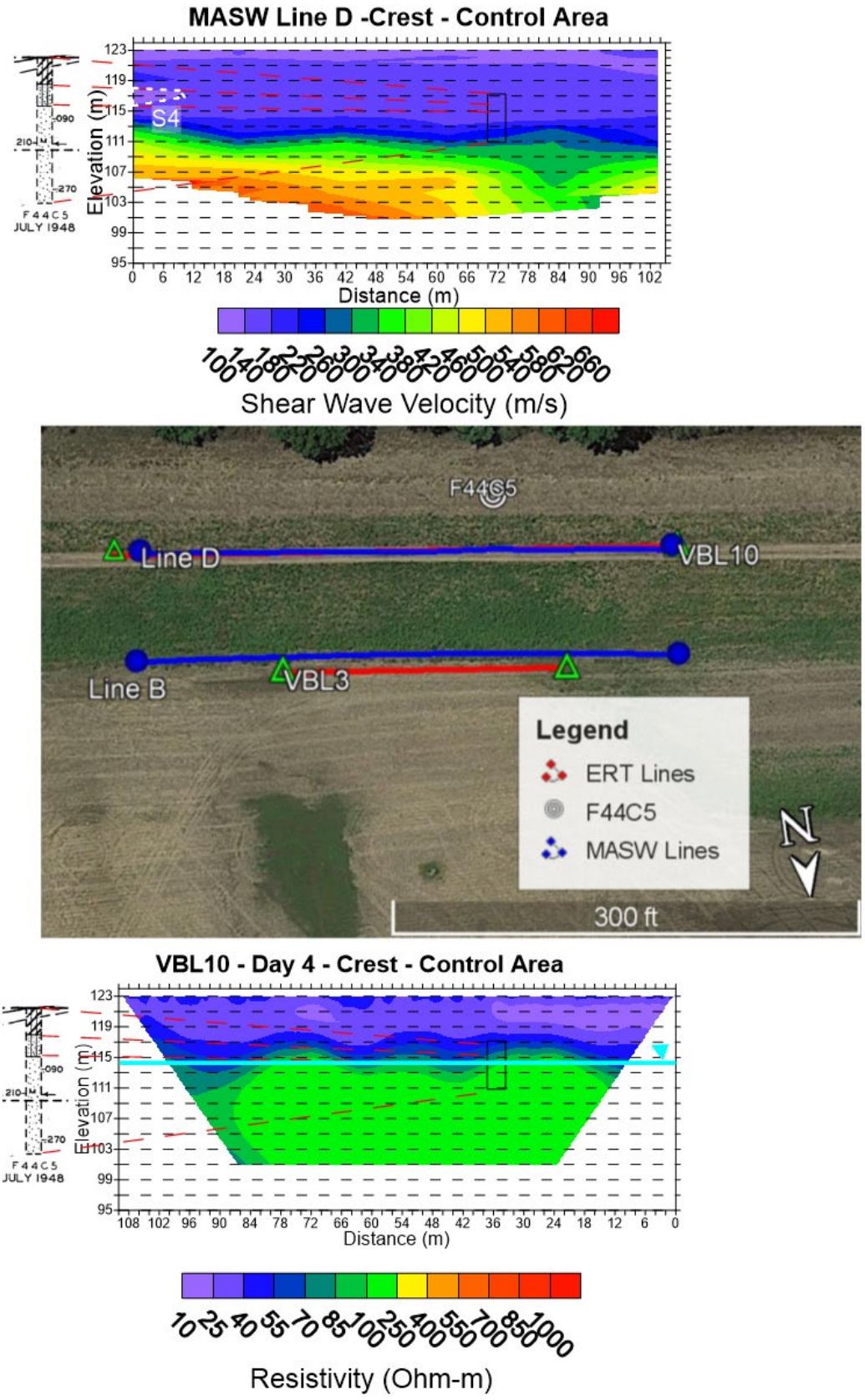

Figure 46 Comparison of co-located control area DC ERT and MASW crest lines

The higher performance of the levee in the control area can largely be attributed to more favorable geological conditions. The continuity and thickness of the conductive top stratum increase moving west from the internal erosion area to the control area, which can be observed both in the CCR data (Figure 32) and when comparing internal erosion area landside toe lines to the control area landside toe lines (Figure 42). Additionally, as discussed in Section 4.1, the clay content of soils encountered in the historical borings increases moving west from the internal erosion area to the control area (Figure 32). The observed decrease in sand content of the levee foundation materials in the CCR, DC ERT, and boring data is consistent with the expected fining of point bar deposits towards the convex side of point bar deposits; therefore, the lack of levee distress features associated with internal erosion damage observed in the control area is likely due to increased clay content of foundation soils moving towards the convex side of the point bar deposits. As previously discussed, the point bar deposits in the control area are nearly perpendicular to the levee, leading to a more randomized distribution of sand boils rather than a concentration of internal erosion damage at the landside toe as observed in the internal erosion area (Kolb 1975). In addition to geological factors, the relief well present near VBL11B, if functional, may prevent the formation of a blocked exit condition and sand boil formation in the control area.

4.5 Laboratory Testing Results

4.5.1 Laboratory Electrical Resistivity

The measured ER for varying plasticity index (PI), dry density, and water content values are given in Table 6, Table 7, and Table 8, respectively. It is evident from the results in Table 6 that as PI increases, the ER decreases for a given density and water content. Also, when water content increases, the ER decreases (Table 8). This is as expected based on results from literature. However, when water content and PI are held constant and density is varied, very little influence in the recorded ER values are observed. It is noted that the differences in density for these samples was very small even though different compaction blow counts were used to make the samples.

Table 6 Results of electrical resistivity for plasticity index

Designation	PI	Test 1			Test 2		
		w (%)	ρ_d (kg/m^3)	ER (Ω·m)	w (%)	ρ_d (kg/m^3)	ER (Ω·m)
SC-1	11	11.2	1838	55	11.2	1842	55
SC-2	14	11.4	1838	12.5	10.9	1839	14.5
SC-3	43	11.1	1846	8.5	10.8	1849	11
SC-4	44	10.9	1868	8.45	11.5	1873	8
SC-5/CL	13	10.6	1826	51.5	NA	NA	NA
SM-1	11	11.1	1847	63	NA	NA	NA

Table 7 Results of electrical resistivity for varying dry density

Designation	w (%)	ρ_d (kg/m^3)	ER (Ω·m)
SC-3	11.31	1904	7.70
SC-3	11.26	1894	8.05
SC-3	11.57	1863	8.11

Table 8 Results of electrical resistivity for varying water content

Designation	w (%)	ρ_d (kg/m^3)	ER (Ω·m)
SC-3	9.88	1859	14.5
SC-3	11.57	1863	8.11
SC-3	14.12	1852	6.5

4.5.2 Hole Erosion Test

The erosion rate index was determined for each HET conducted and the results are presented in Tables 9-11. As shown in Table 9, the ERI tends to increase for increasing PI. The lower PI soils resulted in ERIs of 3-4 which corresponds to a moderately rapid erosion rate. The higher PI soils exhibited ERIs of 4-6 which corresponds to a moderately slow to very slow erosion rate.

The ERI of the soils tended to decrease with decreasing density meaning that less dense soils would erode more easily (Table 10). As water content increased, the ERI also increased slightly (Table 11). This indicates that a wetter soils would exhibit a higher resistance to erosion.

Table 9 Results of HET for varying plasticity index

Designation	PI	Test 1			Test 2			Test 3		
		w (%)	ρ_d (kg/m^3)	ERI	w (%)	ρ_d (kg/m^3)	ERI	w (%)	ρ_d (kg/m^3)	ERI
SC-1	11	11.4	1839	3.93	10.9	1847	4.34*	11.4	1840	4.0
SC-2	14	11.2	1847	4.31	11.1	1833	4.60	NA	NA	NA
SC-3	43	11.0	1837	4.66	10.9	1840	4.72	NA	NA	NA
SC-4	44	11.4	1844	5.24	11.4	1845	4.60*	NA	NA	NA
SC-5/CL	13	11.1	1835	3.83*	11.1	1848	4.25	11.0	1848	4.1
SM-1	11	11.0	1842	4.17	11.1	1835	3.99	NA	NA	NA

Note: Values with (*) correspond to those where one or more problems were encountered during data processing.

Table 10 Results of HET for varying dry density

Designation	Number of Blows	Test 1			Test 2		
		w (%)	ρ_d (kg/m^3)	ERI	w (%)	ρ_d (kg/m^3)	ERI
SC-3	25	11.33	1912	5.20	11.67	1918	5.56
SC-3	22	11.61	1897	5.06	NA	NA	NA
SC-3	19	11.39	1873	4.84	11.69	1867	4.88*

Note: Values with (*) correspond to those where one or more problems were encountered during data processing.

Table 11 Results of HET for varying water content

Designation	Test 1			Test 2		
	w (%)	ρ_d (kg/m^3)	ERI	w (%)	ρ_d (kg/m^3)	ERI
SC-3	9.88	1878	4.89	NA	NA	NA
SC-3	11.39	1873	4.84	11.69	1867	4.88*
SC-3	13.86	1877	4.54*	14.20	1858	4.73

Note: Values with (*) correspond to those where one or more problems were encountered during data processing.

4.5.3 Correlations of Laboratory Electrical Resistivity and HET Erosion Rate Index

The soil erosion rate index (ERI) values were plotted with the electrical resistivity (ER) values to investigate any existing correlations as each of the properties investigated varied (Figure 47, Figure 48, and Figure 49). Figure 47 shows ERI versus ER points when there are only variations in PI. While the groupings do indicate some likely relationship where higher ER corresponds to soils with lower ERI, it was not possible to generate a linear correlation between both parameters since the data are limited and clustered in the extremes. More soils with PI between 20 and 45 should be tested to further derive this trend.

Figure 48 shows that the erosion rate index increases as the resistivity decreases under the influence of dry density. The degree of correlation was described as "very strong" and negative ($r = -0.85$); however, it should be noted that the range of values this trend describes is very small and more testing should be conducted to confirm this relationship.

For variations in moisture content, the ER and ERI have a positive correlation showing that ERI increases with increasing ER (Figure 49). This means that a drier soil will have a higher ERI and erode more.

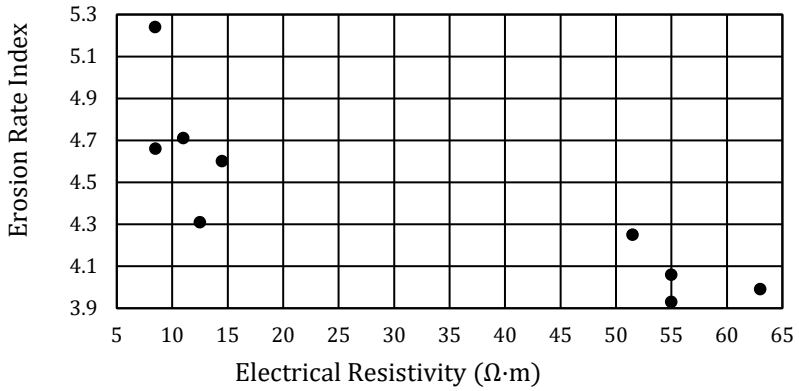

Figure 47 ERI versus ER with variations in plasticity index

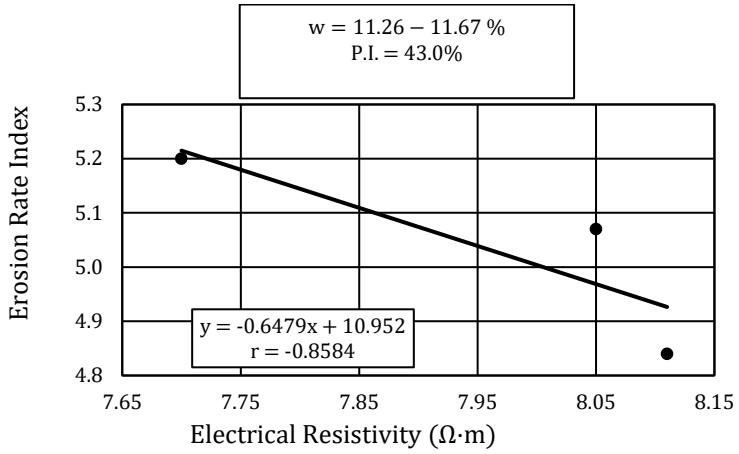

Figure 48 ERI versus ER with variations in dry density

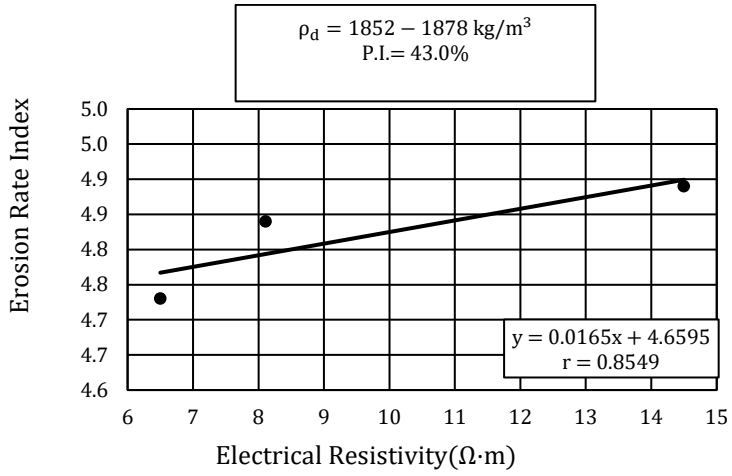

Figure 49 ERI versus ER with variations in water content.

5 Impacts/ Benefits of Implementation

The use of geophysical methods such as CCR, DC ERT, and MASW to assess internal erosion damage in levees provides several key benefits:

- **Rapid, continuous assessment**

  The Capacitively Coupled Resistivity (CCR) method offers a rapid and continuous means of conducting electrical resistivity profiling along long levee stretches. In this study, the CCR surveys efficiently covered the entire approximately 1.5-kilometer length of the levee crest and the landside toe by employing the 5-receiver OhmMapper TR5 measurement system, towed along designated survey lines. Unlike traditional methods that involve fixed electrodes driven into the ground, this system utilizes capacitive coupling between transmitter and receiver dipoles that are dragged along the ground surface. This innovative approach facilitates rapid data collection without the time-consuming process of installing numerous electrodes.

  The continuous CCR survey delivers a comprehensive overview of subsurface resistivity and stratigraphy variations along the levee system, providing insights up to 5 meters in depth on the crest and landside of the levee. It serves as a valuable tool for detecting anomalies in the data that might indicate conditions related to internal erosion damage, such as the presence of thin or intermittent clay layers, vertical upward flow of high-resistivity sands, or high-resistivity zones in general. This data guides the selection of specific targets for more detailed follow-up testing, such as higher resolution geophysical methods like DC ERT or direct invasive techniques like geotechnical drilling. This refined targeting of follow-up efforts significantly enhances investigation efficiency, ensuring that time-consuming and intrusive direct testing is focused solely on the highest-risk zones identified during the initial CCR survey.

  For instance, in this study, landside CCR data pinpointed the zone where the 2019/2021 slope failures and intense sand boil activity occurred as the critical "internal erosion area." This observation informed the decision to concentrate follow-up DC ERT surveying on this particular area due to the observed high-resistivity anomalies. The preliminary continuous CCR survey, particularly valuable in cases where the locations of internal erosion damage are unknown, facilitates the precise targeting of comprehensive investigations aimed at characterizing and mitigating any identified damage.

- **Detailed subsurface stratigraphy**

  The Direct Current Electrical Resistivity Tomography (DC ERT) method offers significantly higher-resolution imaging of subsurface stratigraphy when compared to the sparse and spatially constrained data obtained through geotechnical boring. In this study, we employed a 56-electrode system with electrode spacings ranging from 1 to 3 meters, allowing us to achieve meter-scale imaging of the subsurface along survey lines spanning

from 55 to 165 meters in length. The collection of multiple perpendicular survey lines further facilitated pseudo-3D mapping.

This enhanced resolution afforded by DC ERT subsurface imaging enables a more precise delineation of critical features indicative of internal erosion processes. For instance, it enables the identification of thinning or absence of low-resistivity surface clay layers and the occurrence of the upward flow of high-resistivity sands. These characteristics can be challenging to conclusively pinpoint using sporadic boring data, which often misses crucial inter-borehole stratigraphy. The extensive spatial coverage and multi-directional imaging capabilities of DC ERT provide a more definitive identification of internal erosion indicators, as mentioned earlier.

Furthermore, the heightened resolution of DC ERT empowers us to create more accurate maps of the boundaries and spatial extents of zones affected by internal erosion damage. This stands in stark contrast to the limited subsurface insights gained from isolated borings. The increased level of detail enables a more thorough assessment of the progression and geometric aspects of subsurface damage. This, in turn, informs decisions regarding the most critical locations for repairs or risk reduction measures, ultimately enhancing the integrity and safety of levees.

In summary, the fine-scale stratigraphic imaging delivered by extensive DC ERT surveying offers superior identification and delineation of internal erosion features that are typically challenging to definitively characterize using conventional sparse boring data.

- **Improved visualization of damage geometry**

  Employing perpendicular longitudinal and transverse DC ERT survey lines significantly enhances our ability to accurately map the 3D geometry of internal erosion damage zones within the levee system. Relying solely on traditional visual inspection methods for identifying internal erosion has limitations, as visual cues, such as sand boils, cannot conclusively reveal the subsurface progression and extent of internal piping and erosion. Sparse boring data also offers very limited subsurface sampling, rarely intersecting the full 3D extent of internal erosion damage zones.

  In contrast, the collection of multiple DC ERT survey lines, both in longitudinal (along the levee crest and toe) and transverse (perpendicular to the levee) orientations, enables the mapping of interpreted internal erosion damage in multiple dimensions. This approach provides a more definitive delineation of damage zone boundaries and spatial extent in 3D, transcending the confines of 2D surface expressions or widely spaced borings.

  For example, in our study, suspected areas of internal erosion damage were identified in longitudinal DC ERT lines along the levee toe based on anomalies such as high resistivity and upward-flowing sand. Subsequent transverse DC ERT lines played a crucial role in confirming the subsurface extent and geometry of these damage zones across the width of the levee. The additional perspective offered by transverse surveys supplies vital

information regarding whether and how interpreted internal erosion zones from longitudinal surveys may extend across or be contained within the levee. This additional data, derived from multiple survey directions, proves invaluable in determining the complete 3D geometries of internal erosion features.

The utilization of integrated longitudinal and transverse DC ERT surveys to map internal erosion in multiple dimensions offers a level of damage zone visualization that conventional methods, such as visual inspection or limited borings, cannot achieve. This approach overcomes the limitations of other techniques and provides a superior understanding of subsurface erosion geometries, which is critical for effective repair and risk management.

- **Temporal monitoring:**

  Conducting repeat DC ERT surveys along the same lines during different seasons proves invaluable in corroborating interpreted internal erosion damage zones. These surveys track how the measured resistivity changes in response to evolving subsurface conditions over time.

  It's important to note that the electrical resistivity of soils naturally undergoes seasonal variations due to fluctuations in saturation levels, pore fluid resistivity, temperature, and various environmental factors. However, zones affected by genuine internal erosion damage often exhibit distinct resistivity changes over time when compared to the surrounding intact soils.

  For instance, in our study, longitudinal DC ERT surveys were repeated during both wetter and drier periods. Suspected internal erosion damage zones displayed more pronounced increases in resistivity over time compared to the surrounding soils. This phenomenon was attributed to the greater drainage capacity of these higher permeability zones as water levels decreased between surveys.

  Furthermore, internal erosion damage zones demonstrated more significant resistivity decreases in comparison to the surrounding soils during wetting periods. This behavior aligns with the extensive flushing and saturation of the damaged zones. By monitoring how an interpreted internal erosion zone responds over time in contrast to the surrounding undamaged zones, repeat seasonal DC ERT surveys enhance confidence in the accuracy of the internal erosion interpretation. These distinct seasonal responses serve to validate that an identified anomaly indeed represents a zone characterized by enhanced permeability and porosity, rather than an intact soil layer.

  This capacity for time-lapse resistivity monitoring stands as a fundamental advantage of DC ERT over conventional direct methods, such as boring logs, which only offer a static, one-time snapshot of subsurface conditions. Repeat ERT surveys provide dynamic validation of internal erosion damage interpretations through the tracking of seasonal resistivity changes.

- **Complementary information:**

  The integration of multiple complementary geophysical datasets, such as electrical resistivity data obtained from ERT surveys and shear wave velocity data acquired through MASW surveys, plays a crucial role in enhancing our understanding of subsurface stratigraphy, anomalies, and material properties. This integration significantly bolsters our confidence in interpreting internal erosion zones.

  While ERT data offers valuable insights into the distribution of subsurface resistivity and potential anomalies, it's important to recognize that the fundamental property being measured is electrical conductivity. This conductivity is influenced by a complex interplay of factors within the subsurface. In contrast, shear wave velocity data directly informs us about mechanical stiffness, a property that more directly correlates with the engineering properties of interest. Essentially, harder, stiffer, and intact materials transmit shear waves at faster speeds compared to softer, weaker, and potentially damaged zones.

  Furthermore, shear velocity profiles can provide high-resolution information regarding stratigraphic layering. By amalgamating the complementary information offered by both methods into an integrated interpretation, we enhance our confidence in identifying internal erosion damage zones, surpassing the level of certainty achievable when relying solely on one method. For instance, in our study, suspected internal erosion zones were initially flagged as high resistivity anomalies in the ERT data. The low velocity anomalies identified in the MASW data subsequently provided corroborating evidence of disturbance within those same zones. This integrated interpretation, which draws upon the collective evidence from both datasets, lends stronger support to the presence of internal erosion compared to evaluating each dataset in isolation.

  Leveraging complementary geophysical techniques within an integrated interpretation capitalizes on the unique strengths of each method while mitigating the limitations of any single technique. This approach significantly enhances our confidence in identifying internal erosion damage zones, thereby providing invaluable insights for effective levee management.

- **Rapid repair decisions:**

  The precise location and detailed characterization of internal erosion damage zones through geophysical imaging offer a strategic approach to levee maintenance. This approach prevents the need for broad, all-encompassing repairs along entire levee segments and instead directs repair efforts toward specific areas at the highest risk of developing issues such as leaks, seepage, and piping failures.

  Conventional methods, such as visual inspections and sparse direct testing, often struggle to definitively ascertain the full extent of internal erosion damage within a levee. This inherent uncertainty can lead to extensive and costly repairs being carried out along significant stretches of the levee in an effort to mitigate perceived risks. In contrast,

comprehensive geophysical datasets are better equipped to identify and characterize damage zones with precision in three dimensions. As a result, repairs can be strategically concentrated in locations where imaging has conclusively identified subsurface degradation and heightened risk. For instance, in our study, suspected internal erosion zones were widespread along specific sections of the levee toe, while other sections showed no signs of damage. This selective identification of damage zones allows for targeted repairs only where necessary, eliminating the need to rebuild the entire levee toe. This focused mitigation approach optimizes the allocation of repair resources, minimizes unnecessary costs, and reduces environmental and community impacts. Additionally, by prioritizing the most critical areas of concern, it ensures that the most pressing damage is addressed promptly.

In summary, the geophysical assessment of internal erosion damage, with its ability to facilitate targeted repairs, yields a host of environmental, social, and economic benefits in comparison to conventional approaches that necessitate wholesale repairs along entire levee segments based on worst-case scenarios.

- **Improved risk assessment:**

  The detailed and high-resolution mapping of internal erosion damage, facilitated by geophysical imaging, plays a pivotal role in enhancing the engineering assessment of risks associated with piping and seepage failures. This improvement allows for a more accurate prioritization of repair needs and the implementation of emergency flood control measures during high-water events.

  Conventional methods such as visual inspections and sporadic direct testing face challenges in accurately gauging the risks associated with piping failures, primarily because the precise locations of subsurface degradation remain unknown. This uncertainty often leads to conservative risk assessments based on worst-case scenarios. In contrast, the comprehensive 3D geophysical imaging provides a clear delineation of compromised subsurface integrity and furnishes essential data for analyzing the mechanisms underlying potential failures. Risk assessment benefits from the inclusion of intricate damage zone geometries, the identification of high-permeability pathways, and the monitoring of seasonal changes over time.

  For instance, in our study, ERT imaging revealed that certain sections of the levee toe exhibited extensive evidence of piping erosion and upward sand flow, while other sections remained structurally intact. This variability in risk information allows for a logical and strategic approach to prioritize and stage repairs, as opposed to merely reacting to worst-case assumptions. Additionally, during flood fighting scenarios, the observed progression of mapped piping zones offers advanced notice of potential breach locations, thereby indicating where proactive emergency mitigation efforts should be deployed.

In summary, high-resolution geophysical mapping substantially enhances the assessment of piping and failure risks compared to reliance solely on visual inspections or sparse data. This improvement empowers levee management decision-making processes, enabling actions based on actual measured conditions rather than uncertainties.

- **Non-destructive Testing:**

  One of the paramount advantages of geophysical imaging methods like ERT and MASW is their complete non-invasiveness, which ensures that they do not introduce any permanent alterations or weaken the integrity of the levee, in stark contrast to extensive direct investigation campaigns involving boring and trenching.

  Techniques like boring and trenching necessitate intentional damage to the levee's integrity by removing soil and creating pathways that allow water infiltration. If carried out extensively to map subsurface conditions, these methods have the potential to disrupt large areas, potentially exacerbating internal erosion risks. In contrast, geophysical surveys employ sensors placed on the ground surface, which produce no lasting alterations or degradation to the levee prism. The techniques discussed in this study, including ERT, MASW, and CCR, are entirely non-destructive and leave no lasting negative impacts.

  The ability to repeatedly survey the same levee sections over time without concerns of cumulative damage is a significant advantage. It enables the safe monitoring of internal erosion development across multiple flood seasons, offering insights that inform repair timelines. Moreover, the effectiveness of mitigation efforts can be assessed through repeat post-repair imaging. While some degree of direct investigation may still be necessary for ground-truthing, the non-invasive nature of geophysics minimizes risks, avoids the creation of new damage pathways, and facilitates flexible, repeat data collection to continuously evaluate and manage levee integrity. This advantage enhances both safety and sustainability when compared to relying solely on destructive direct testing.

  In summary, the non-invasive character of geophysical methods yields substantial benefits in terms of levee monitoring, management, and safety, particularly when contrasted with techniques that permanently impair levee integrity, such as boring and trenching campaigns.

- **Laboratory Testing:** The laboratory hole erosion test (HET) and electrical resistivity (ER) test can be used to obtain an estimate of erodibility that can be tied to the field gathered geophysical data to provide improved predictions of erosion resistance for a particular site. The field ER values can also be more accurately linked to soil type through developments and further testing of additional benchmark samples. This testing can be used to create a database that contains the relationships and typical values for a range of soil types so that improved field estimates and mapping can be made.

6 Recommendations and Conclusions

The results of geophysical surveys, including CCR, DC ERT, and MASW, performed on a section of the Crawford County Levee System supports that internal erosion damage can be assessed using geophysical methods. However, further research including additional geophysical surveying at project site, ground-truthing of interpreted zones of internal erosion damage, and application of the methods this study to other projects sites is needed to understand the uncertainties associated with geophysical assessment of internal erosion damage in levees. Preliminary continuous CCR surveying was found to be valuable for selection of locations for additional DC ERT and MASW surveying. A combination of longitudinal and transverse DC ERT surveys was more effective than MASW for assessing internal erosion damage at the project site. The MASW surveying provided additional information on subsurface stratigraphy and verified a zone of internal erosion damage identified in the DC ERT lines; however, no additional zones of internal erosion damage were identified in the MASW lines. Multi-Channel Analysis of Surface Wave surveys with decreased spacing of landstreamer setups are recommended for future studies to obtain higher resolution 2-D Vs profiles.

Zones of potential internal erosion damage in the DC ERT lines were identified by high ER, thinning of the conductive top stratum, upward flow of high ER soils, and the presence of levee distress features in satellite imagery. Due to the 3D nature of internal erosion damage, the acquisition of perpendicular DC ERT lines is valuable for assessing potential zones of internal erosion damage and provides improved visualization of internal erosion damage over traditional destructive testing methods. Additionally, repeat DC ERT surveys in different seasonal conditions assisted in assessing suspected zones of internal erosion damage.

The HET and laboratory electrical resistivity results showed that properties could be singled out and systematically varied to obtain a better understanding of the influence of various properties on erosion resistance. These tests can also be used to develop correlations tying laboratory ER and ERI with field measured ER to enable improved field predictions of erodibility. More testing is needed to confirm the trends observed herein and develop relationships for a larger range of soil properties and soil types.

7 References

Abu-Hassanein, Z. S., Benson, C. H., & Blotz, L. R. (1996). Electrical resistivity of compacted clays. *Journal of Geotechnical Engineering*, *122*(5), 397–406. https://doi.org/10.1061/(ASCE)0733-9410(1996)122:5(397)

American Society of Civil Engineers. (2021). *2021 report card for america's infrastructure.*

Arato, A., Vagnon, F., & Comina, C. (2022). First application of a new seismo-electric streamer for combined resistivity and seismic measurements along linearly extended earth structures. *Near Surface Geophysics*, *20*(2), 117–134. https://doi.org/10.1002/nsg.12198

Archie, G. E. (1942). The Electrical Resistivity Log as an Aid in Determining Some Reservoir Characteristics. *Transactions of the AIME*, *146*(01), 54–62. https://doi.org/10.2118/942054-G

Barner, M., Hauser, E., & Wolfe, P. (2001). The Use of Non-Invasive Geophysics to Assess Damage by Burrowing Animals to Earthen Levees Near Dayton, Ohio. In *Symposium on the Application of Geophysics to Engineering and Environmental Problems 2001* (pp. GTD4–GTD4). Environment and Engineering Geophysical Society. https://doi.org/10.4133/1.2922903

Bierman, P. R., & Montgomery, D. R. (2014). *Key concepts in geomorphology*. W.H. Freeman and Company Publishers.

Bonelli, S. (Ed.). (2013). *Erosion in geomechanics applied to dams and levees*. ISTE Ltd ; John Wiley and Sons, Inc.

Brackett, T. (2012). *Use of geophysics to map subsurface features at levee seepage locations* [Master's Thesis, The University of Mississippi]. Electronic Theses and Dissertations. https://egrove.olemiss.edu/etd/60

Briaud, J.-L. (2008). Case histories in soil and rock erosion: Woodrow Wilson Bridge, Brazos River Meander, Normandy Cliffs, and New Orleans levees. *Journal of Geotechnical and Geoenvironmental Engineering*, *134*(10), 1425–1447. https://doi.org/10.1061/(ASCE)1090-0241(2008)134:10(1425)

Briaud, J. L., Ting, F. C. K., Chen, H. C., Cao, Y., Han, S. W., & Kwak, K. W. (2001). Erosion function apparatus for scour rate predictions. *Journal of geotechnical and geoenvironmental engineering*, 127(2), 105-113.

Briaud, J. L., Ting, F., Chen, H. C., Gudavalli, R., Kwak, K., Philogene, B., ... & Li, Y. (1999). *SRICOS: Prediction of scour rate at bridge piers*. Texas Transportation Institute, The Texas A&M University, College Station, Texas, USA. Report, 2937-1.

Cardarelli, E., Cercato, M., & De Donno, G. (2014). Characterization of an earth-filled dam through the combined use of electrical resistivity tomography, P- and SH-wave seismic tomography and surface wave data. *Journal of Applied Geophysics*, *106*, 87–95. https://doi.org/10.1016/j.jappgeo.2014.04.007

Cardarelli, E., Cercato, M., & Di Filippo, G. (2010). Geophysical investigation for the rehabilitation of a flood control embankment. *Near Surface Geophysics*, *8*(4), 287–296. https://doi.org/10.3997/1873-0604.2010018

Chlaib, H. K., Mahdi, H., Al-Shukri, H., Su, M. M., Catakli, A., & Abd, N. (2014). Using ground penetrating radar in levee assessment to detect small scale animal burrows. *Journal of Applied Geophysics*, *103*, 121–131. https://doi.org/10.1016/j.jappgeo.2014.01.011

Comina, C., Vagnon, F., Arato, A., Fantini, F., & Naldi, M. (2020). A new electric streamer for the characterization of river embankments. *Engineering Geology*, *276*, 105770. https://doi.org/10.1016/j.enggeo.2020.105770

Cox, B. R., & Wood, C. M. (2011). Surface wave benchmarking exercise: Methodologies, results, and uncertainties. *GeoRisk 2011*, 845–852. https://doi.org/10.1061/41183(418)89

Dahlin, T., & Zhou, B. (2004). A numerical comparison of 2D resistivity imaging with 10 electrode arrays. *Geophysical Prospecting*, *52*(5), 379–398. https://doi.org/10.1111/j.1365-2478.2004.00423.x

Dahlin, T., & Zhou, B. (2006). Multiple-gradient array measurements for multichannel 2D resistivity imaging. *Near Surface Geophysics*, *4*(2), 113–123. https://doi.org/10.3997/1873-0604.2005037

Dal Moro, G. (2015). *Surface wave analysis for near surface applications*. Elsevier.

Dunbar, J. B., Smullen, S., & Stefanov, J. E. (2007). The use of geophysics in levee assessment. *Symposium on the Application of Geophysics to Engineering and Environmental Problems 2007*, 61–68. https://doi.org/10.4133/1.2924719

Dunbar, J. B., Stefanov, J. E., Bishop, M. J., Peyman-Dove, L., Llopis, J. L., Murphy, W. L., & Ballard, R. F. (2003). An integrated approach for assessment of levees in the Lower Rio Grande Valley. *Symposium on the Application of Geophysics to Engineering and Environmental Problems 2003*, 350–362. https://doi.org/10.4133/1.2923176

Flood Damage Reduction/System Inspection Report. (n.d.). United States Army Corps of Engineers. Retrieved December 3, 2022, from https://www.usace.army.mil/Missions/Civil-Works/Levee-Safety-Program/Levee-Inspections/

Foti, S., Lai, C., Rix, G. J., & Strobbia, C. (2015). *Surface Wave Methods for Near-Surface Site Characterization*. CRC Press.

Gillip, J. A., & Payne, J. (2011). *Geophysical characterization of the Lollie Levee near Conway, Arkansas, using capacitively coupled resistivity, coring, and direct push logging. USGS Data Series Report No. 640.* U.S. Geological Survey. https://doi.org/10.3133/ds640

Goff, D., Lorenzo, J., & Hayashi, K. (2015). Resistivity and shear wave velocity as a predictive tool of sediment type in coastal levee foundation soils. In *Symposium on the Application of Geophysics to Engineering and Environmental Problems 2015* (pp. 167–176). Society of Exploration Geophysicists and Environment and Engineering Geophysical Society. https://doi.org/10.4133/SAGEEP.28-026

Griffiths, S. C., Cox, B. R., Rathje, E. M., & Teague, D. P. (2016). Surface-Wave dispersion approach for evaluating statistical models that account for shear-wave velocity uncertainty. *Journal of Geotechnical and Geoenvironmental Engineering*, *142*(11), 04016061. https://doi.org/10.1061/(ASCE)GT.1943-5606.0001552

Hanson, G. J., & Cook, K. R. (2004). Apparatus, test procedures, and analytical methods to measure soil erodibility in situ. *Applied engineering in agriculture*, *20*(4), 455-462.

Hayashi, K., & Inazaki, T. (2013). Integrated geophysical exploration for safety assessment of levee systems. *Geo-Congress 2013.* 182–191. https://doi.org/10.1061/9780784412787.019

Hayashi, K., Inazaki, T., Kitao, K., & Kita, T. (2014). Statistical soil type estimation using cross-plots of S-Wave velocity and resistivity in Japanese levees. *Geo-Congress 2014 Technical Papers*, 2460–2468. https://doi.org/10.1061/9780784413272.238

Hayashi, K., Inazaki, T., Kitao, K., & Kita, T. (2019). Statistical estimation of soil parameters in from cross-plots of S-Wave velocity and resistivity obtained by integrated geophysical method. In J. Lorenzo & W. Doll (Eds.), *Levees and Dams: Advances in Geophysical Monitoring and Characterization* (pp. 1–21). Springer International Publishing. https://doi.org/10.1007/978-3-030-27367-5_1

Hayashi, K., & Konishi, C. (2010). Joint use of a surface-wave method and a resistivity method for safety assessment of levee systems. *GeoFlorida 2010: Advances in Analysis, Modeling & Design*, 1340–1349. https://doi.org/10.1061/41095(365)134

Inazaki, T., Hayashi, K., Watanabe, F., Tokumaru, K. M. T., & Imamura, S. (2008). Ground truth verification of an integrated geophysical investigation for the assessment of an earthen levee. *Proceedings of the 21st EEGS Symposium on the Application of Geophysics to Engineering and Environmental Problems, Apr 2008,* cp-177-00040. https://doi.org/10.3997/2214-4609-pdb.177.57

Karl, L., Fechner, T., Schevenels, M., François, S., & Degrande, G. (2011). Geotechnical characterization of a river dyke by surface waves. *Near Surface Geophysics*, *9*(6), 515–527. https://doi.org/10.3997/1873-0604.2011030

Kelley, J. R., Parkman, K. B., Strange, R. C., Breland, B. R., Dunbar, J. B., & Corcoran, M. K. (2019). *Investigation of sand boils near Ware, IL, Middle Mississippi River, Preston Levee District* [Report]. Geotechnical and Structures Laboratory (U.S.). https://hdl.handle.net/11681/33619

Kita, T., Inazaki, T., & Hayashi, K. (2013). 2-Dimensional linear array microtremor survey techniques for earthen levee investigations. *Proceedings of the 11th SEGJ International Symposium, Yokohama, Japan, 18-21 November 2013*, 214–217. https://doi.org/10.1190/segj112013-054

Kouchaki, B. M., Bernhardt-Barry, M. L., Wood, C. M., & Moody, T. (2019). A laboratory investigation of factors influencing the electrical resistivity of different soil types. *Geotechnical Testing Journal*, *42*(4), 20170364. https://doi.org/10.1520/GTJ20170364

Kresse, T. M., Hays, P. D., Merriman, K. R., Gillip, J. A., Fugitt, D. T., Spellman, J. L., Nottmeier, A. M., Westerman, D. A., Blackstock, J. M., & Battreal, J. L. (2014). *Aquifers of Arkansas: Protection, management, and hydrologic and geochemical characteristics of groundwater resources in Arkansas. USGS Numbered Series No. 2014–5149*. U.S. Geological Survey. https://doi.org/10.3133/sir20145149

Kresse, T. M., Westerman, D. A., & Hart, R. M. (2015). *Lithology, hydrologic characteristics, and water quality of the Arkansas River Valley alluvial aquifer in the vicinity of Van Buren, Arkansas. USGS Numbered Series No. 2015–5044*. U.S. Geological Survey. https://doi.org/10.3133/sir20155044

Kuras, O., Beamish, D., Meldrum, P. I., & Ogilvy, R. D. (2006). Fundamentals of the capacitive resistivity technique. *GEOPHYSICS*, *71*(3), G135–G152. https://doi.org/10.1190/1.2194892

Lane, J. W., Ivanov, J., Day-Lewis, F. D., Clemens, D., Patev, R., & Miller, R. D. (2008). Levee evaluation using MASW: Preliminary findings from the citrus lakefront levee, New Orleans, Louisiana. In *Symposium on the Application of Geophysics to Engineering and Environmental Problems 2008* (pp. 703–712). Environment and Engineering Geophysical Society. https://doi.org/10.4133/1.2963312

Lewis, J. M., & Trevisan, A. R. (2019). *Peak streamflow and stages at selected streamgages on the Arkansas River in Oklahoma and Arkansas, May to June 2019. USGS Numbered Series No. 2019–1129*. U.S. Geological Survey. https://doi.org/10.3133/ofr20191129

Lin, Y.-C., Joh, S.-H., & Stokoe, K. H. (2014). Analyst J: Analysis of the UTexas 1 Surface Wave Dataset using the SASW methodology. *Geo-Congress 2014*. 830–839. https://doi.org/10.1061/9780784413272.081

Liu, P., Wang, K., Wang, Q., & Huang, S. (2021). Data acquisition method and the effectiveness of multichannel analysis of surface waves for defect detections on small earthen dams. *Arabian Journal of Geosciences*, *14*(7), 631. https://doi.org/10.1007/s12517-021-07005-6

Llopis, J. L., & Simms, J. E. (2007). *Geophysical surveys for assessing levee foundation conditions, Feather River Levees, Marysville/Yuba City, California* [Report]. Geotechnical and Structures Laboratory (U.S.). https://hdl.handle.net/11681/10545

Loke, M. H. (2022). *Tutorial: 2-D and 3-D electrical imaging surveys*. www.geotomosoft.com

Loke, M. H., Chambers, J. E., Rucker, D. F., Kuras, O., & Wilkinson, P. B. (2013). Recent developments in the direct-current geoelectrical imaging method. *Journal of Applied Geophysics*, *95*, 135–156. https://doi.org/10.1016/j.jappgeo.2013.02.017

Lüthi, M. (2011). *A modified hole erosion test (het-p) to study erosion characteristics of soil*, Doctoral dissertation, University of British Columbia.

Lüthi, M., Fannin, R. J., & Millar, R. G. (2012). A modified hole erosion test (HET-P) device. *Geotechnical Testing Journal*, *35*(4), 660-664.

McKenna, J. R., Dunbar, J. B., Wakeley, L. D., & Smullen, S. (2006). Near surface geophysical methods to assess levee integrity and potential failure. *Symposium on the Application of Geophysics to Engineering and Environmental Problems 2006*, 320–326. https://doi.org/10.4133/1.2923662

Moody, T. (2017). *Geophysical assessment of Kinion Lake Dam* [Master's Thesis, The University of Arkansas]. Graduate Theses and Dissertations. https://scholarworks.uark.edu/etd/2470

Mofarraj Kouchaki, B. (2017). *Laboratory resistivity measurements for soil characterization* [Master's Thesis, The University of Arkansas]. Graduate Theses and Dissertations. https://scholarworks.uark.edu/etd/2455

Moss, R. E. S., & Eller, J. M. (2007). Estimating the probability of failure and associated risk of the California Bay Delta Levee System. *Probabilistic Applications in Geotechnical Engineering*, 1–10. https://doi.org/10.1061/40914(233)21

National Academies of Sciences, E. (2019). *Relationship Between Erodibility and Properties of Soils*. https://doi.org/10.17226/25470

National Levee Database. (2020, April 4). Retrieved December 21, 2022, from https://levees.sec.usace.army.mil/#/levees/system/3705000008/summary

OhmMapper TR1 Operation Manual. (2001). Geometrics, Inc.

Planès, T., Mooney, M. A., Rittgers, J. B. R., Parekh, M. L., Behm, M., & Snieder, R. (2016). Time-lapse monitoring of internal erosion in earthen dams and levees using ambient seismic noise. *Géotechnique*, *66*(4), 301–312. https://doi.org/10.1680/jgeot.14.P.268

Planès, T., Rittgers, J. B., Mooney, M. A., Kanning, W., & Draganov, D. (2017). Monitoring the tidal response of a sea levee with ambient seismic noise. *Journal of Applied Geophysics*, *138*, 255–263. https://doi.org/10.1016/j.jappgeo.2017.01.025

Rahimi, S., Moody, T., Wood, C., Kouchaki, B. M., Barry, M., Tran, K., & King, C. (2019). Mapping subsurface conditions and detecting seepage channels for an embankment dam using geophysical methods: A case study of the Kinion Lake Dam. *Journal of Environmental and Engineering Geophysics*, *24*(3), 373–386. https://doi.org/10.2113/JEEG24.3.373

Rahimi, S., Wood, C. M., Coker, F., Moody, T., Bernhardt-Barry, M., & Mofarraj Kouchaki, B. (2018). The combined use of MASW and resistivity surveys for levee assessment: A case study of the Melvin Price Reach of the Wood River Levee. *Engineering Geology*, *241*, 11–24. https://doi.org/10.1016/j.enggeo.2018.05.009

Rahimi, S., Wood, C. M., & Teague, D. P. (2021). Performance of different transformationt techniques for MASW data processing considering various site conditions, near-field effects, and modal separation. *Surveys in Geophysics*, *42*(5), 1197–1225. https://doi.org/10.1007/s10712-021-09657-1

Rein, A., Hoffmann, R., & Dietrich, P. (2004). Influence of natural time-dependent variations of electrical conductivity on DC resistivity measurements. *Journal of Hydrology*, *285*(1–4), 215–232. https://doi.org/10.1016/j.jhydrol.2003.08.015

Robbins, B. A., & Griffiths, D. V. (2019). Modelling of backward erosion piping in two- and three-dimensional domains. In S. Bonelli, C. Jommi, & D. Sterpi (Eds.), *Internal Erosion in Earthdams, Dikes and Levees* (Vol. 17, pp. 149–158). Springer International Publishing. https://doi.org/10.1007/978-3-319-99423-9_14

Robbins, B. A., Stephens, I. J., Van Beek, V. M., Koelewijn, A. R., & Bezuijen, A. (2020). Field measurements of sand boil hydraulics. *Géotechnique*, *70*(2), 153–160. https://doi.org/10.1680/jgeot.18.P.151

Samouëlian, A., Cousin, I., Tabbagh, A., Bruand, A., & Richard, G. (2005). Electrical resistivity survey in soil science: A review. *Soil & Tillage Research*, *83*, 173–193.

Samyn, K., Mathieu, F., Bitri, A., Nachbaur, A., & Closset, L. (2014). Integrated geophysical approach in assessing karst presence and sinkhole susceptibility along flood-protection

dykes of the Loire River, Orléans, France. *Engineering Geology*, *183*, 170–184. https://doi.org/10.1016/j.enggeo.2014.10.013

Schaefer, J. A., O'Leary, T. M., & Robbins, B. A. (2017). Assessing the implications of sand boils for backward erosion piping risk. *Geo-Risk 2017*, 124–136. https://doi.org/10.1061/9780784480724.012

Sean. (2019, June 18). Gradient Array: Electrical Resistivity Methods, Part 8. *AGIUSA*. https://www.agiusa.com/blog/gradient-array-electrical-resistivity-methods-part-8

Sjödahl, P., Dahlin, T., & Johansson, S. (2010). Using the resistivity method for leakage detection in a blind test at the Røssvatn embankment dam test facility in Norway. *Bulletin of Engineering Geology and the Environment*, *69*, 643–658. https://doi.org/10.1007/s10064-010-0314-y

Slope stability failure on the Crawford County Levee during the 2019 flooding [Online image]. 2019. US Army Corps of Engineers Little Rock District Website.https://www.swl.usace.army.mil/Missions/Disaster-Response/Levee-System-Status/Crawford-County-Levee/igphoto/2002230471/igphoto/2002230471/igphoto/2002230473/

Strange, R. C., Corcoran, M. K., Dunbar, J. B., & Schmitz, D. W. (2016). *The influence of geologic depositional environments on sand boil development, Tara Wildlife Lodge Area in Mississippi* [Report]. Geotechnical and Structures Laboratory (U.S.). https://hdl.handle.net/11681/20310

Thomas, R. G., Smith, D. G., Wood, J. M., Visser, J., Calverley-Range, E. A., & Koster, E. H. (1987). Inclined heterolithic stratification-Terminology, description, interpretation and significance. *Sedimentary Geology*, *53*(1), 123–179. https://doi.org/10.1016/S0037-0738(87)80006-4

Tucker-Kulesza, S., Rutherford, C., & Bernhardt-Barry, M. (2019). Electrical Resistivity at Internal Erosion Locations in Levees. *ISSMGE International Journal of Geoengineering Case Histories*, *5*(2), 55–69. https://doi.org/10.4417/IJGCH-05-02-01

United States Army Corps of Engineers. (2021, April 22). *Engineer Circular 1165-2-218: U.S. Army Corps of Engineers Levee Safety Program*. Engineering and Design. https://www.publications.usace.army.mil/Portals/76/Users/182/86/2486/EC%201165-2-218.pdf?ver=Gm_2vTnybm3P4xgmb5vUbw%3d%3d

Van Beek, V. M., Van Essen, H. M., Vandenboer, K., & Bezuijen, A. (2015). Developments in modelling of backward erosion piping. *Géotechnique*, *65*(9), 740–754. https://doi.org/10.1680/geot.14.P.119

Van de Lageweg, W. I., Van Dijk, W. M., Baar, A. W., Rutten, J., & Kleinhans, M. G. (2014). Bank pull or bar push: What drives scroll-bar formation in meandering rivers? *Geology*, *42*(4), 319–322. https://doi.org/10.1130/G35192.1

Wahl, T.L. (2010). Relating HET and JET test results to internal erosion field tests. *2nd Joint Federal Interagency Conference, Las Vegas, NV, June 27-July 1*.

Wan, C. F., & Fell, R. (2004). Investigation of rate of erosion of soils in embankment dams. *Journal of geotechnical and geoenvironmental engineering*, *130*(4), 373-380.

Wan, C. F., & Fell, R. (2004). Laboratory tests on the rate of piping erosion of soils in embankment dams. *Geotechnical testing journal*, *27*(3), 295-303.

Wathelet, M. (2008). An improved neighborhood algorithm: Parameter conditions and dynamic scaling. *Geophysical Research Letters*, *35*(9), L09301. https://doi.org/10.1029/2008GL033256

Wodajo, L. T., Hickey, C. J., & Brackett, T. C. (2019). Application of seismic refraction and electrical resistivity cross-plot analysis: A case study at Francis Levee site. In J. Lorenzo & W. Doll (Eds.), *Levees and Dams: Advances in Geophysical Monitoring and Characterization* (pp. 23–40). Springer International Publishing. https://doi.org/10.1007/978-3-030-27367-5_2

Zywicki, D. J. (1999). *Advanced signal processing methods applied to engineering analysis of seismic surface waves* [Ph.D., Georgia Institute of Technology]. ProQuest. https://www.proquest.com/docview/304501274/abstract/49D6E4D663D04759PQ/1

Appendix

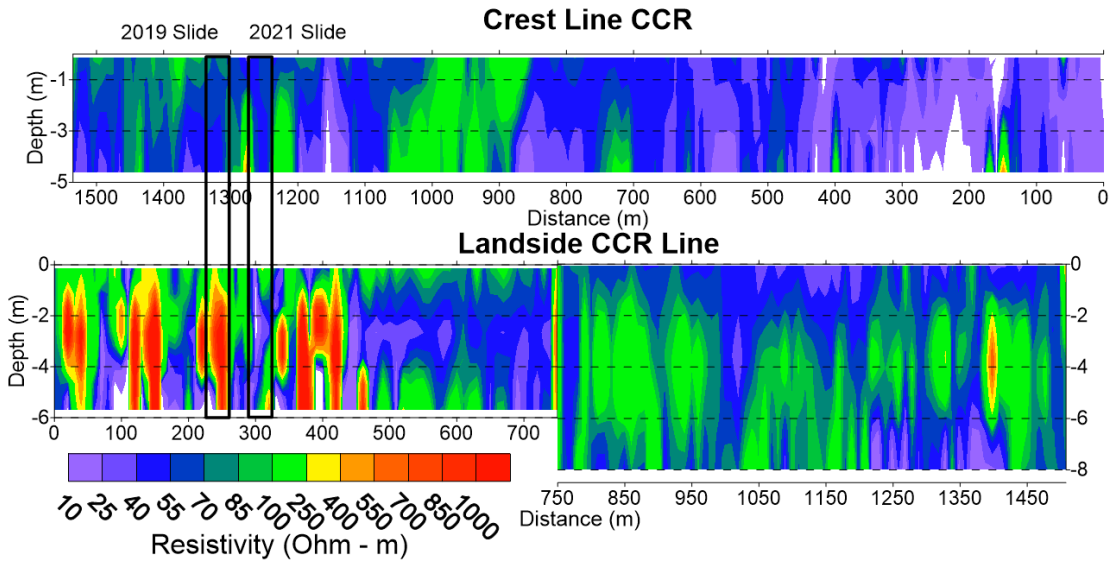

Appendix A-1 Crest and landside CCR lines

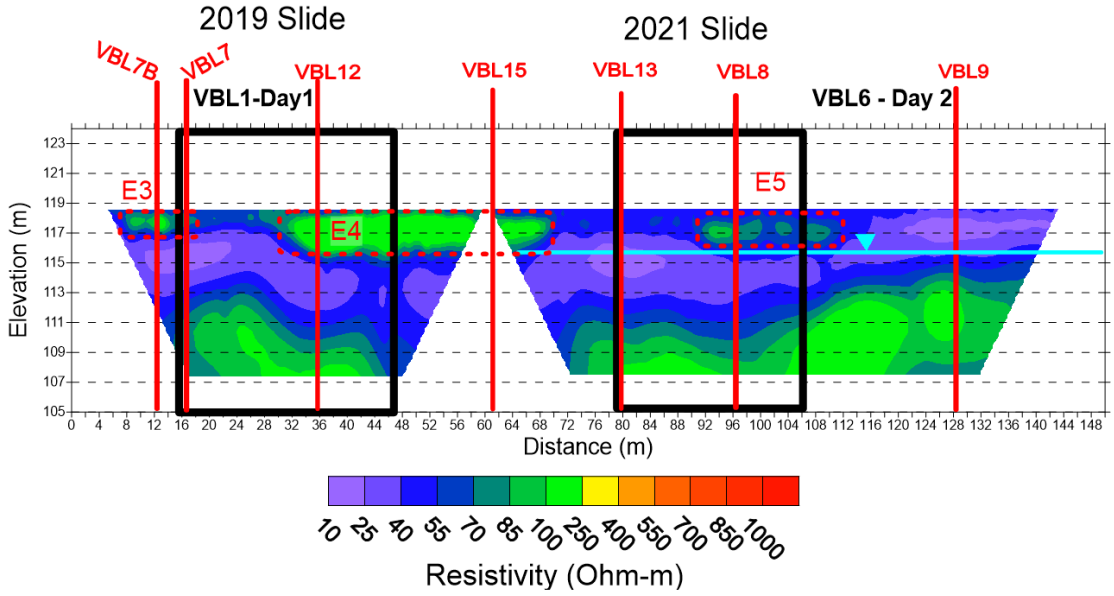

Appendix A-2 Internal erosion area longitudinal landside DC ERT lines VBL1 and VBL6

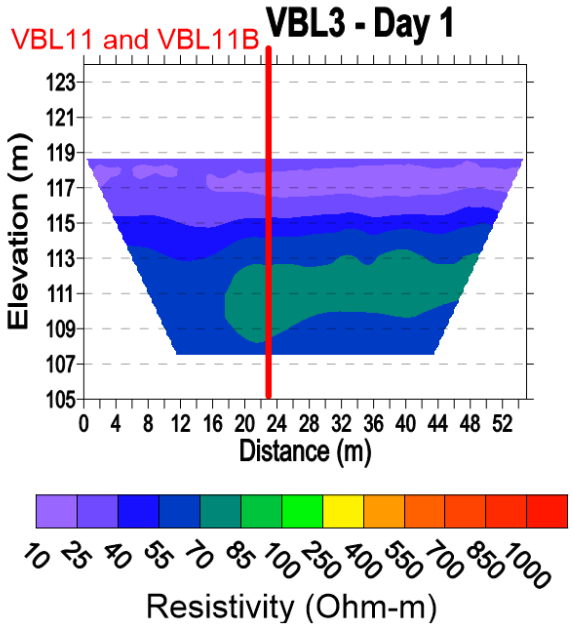

Appendix A-3 Control area longitudinal landside DC ERT line VBL3

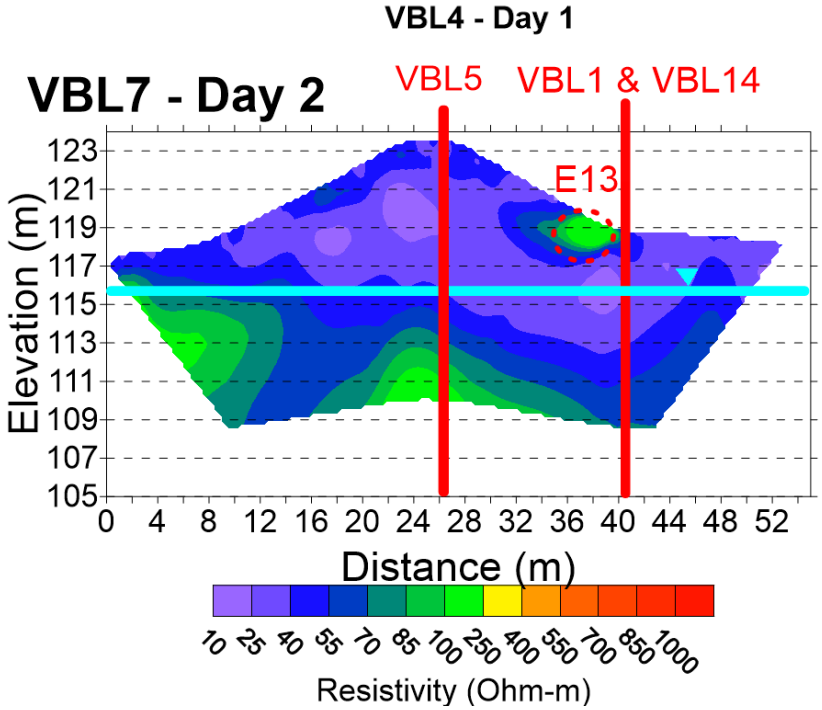

Appendix A-4 Longitudinal landside DC ERT line VBL4, located to the west of the control area

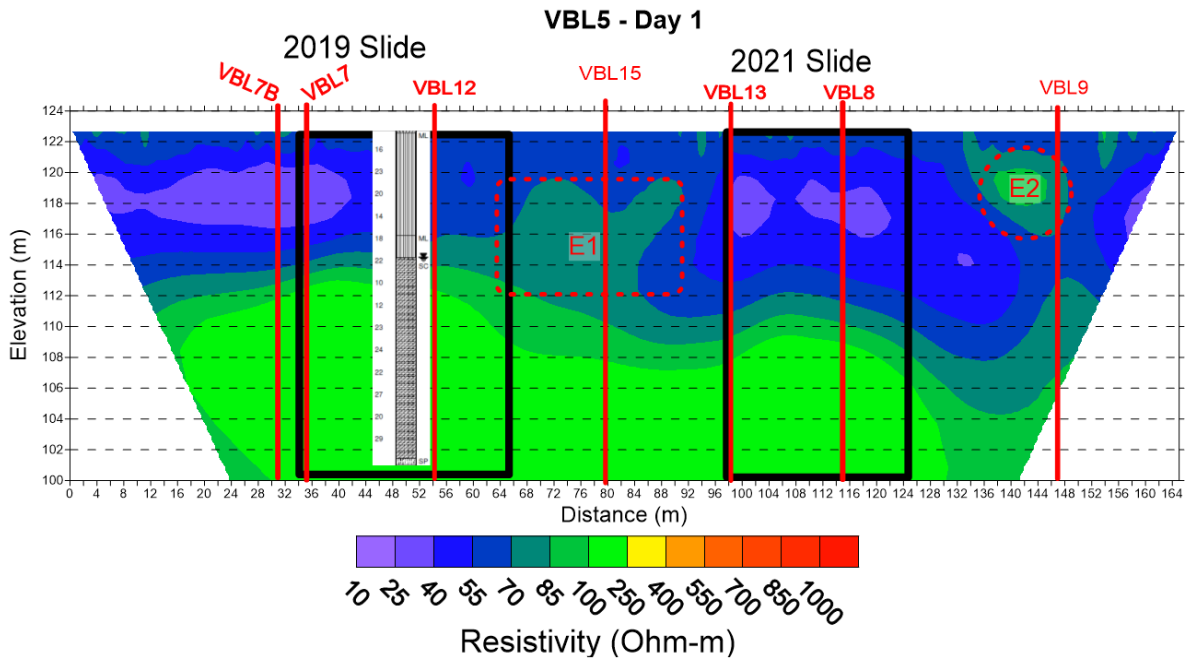

Appendix A-5 Internal erosion area longitudinal crest DC ERT line VBL5

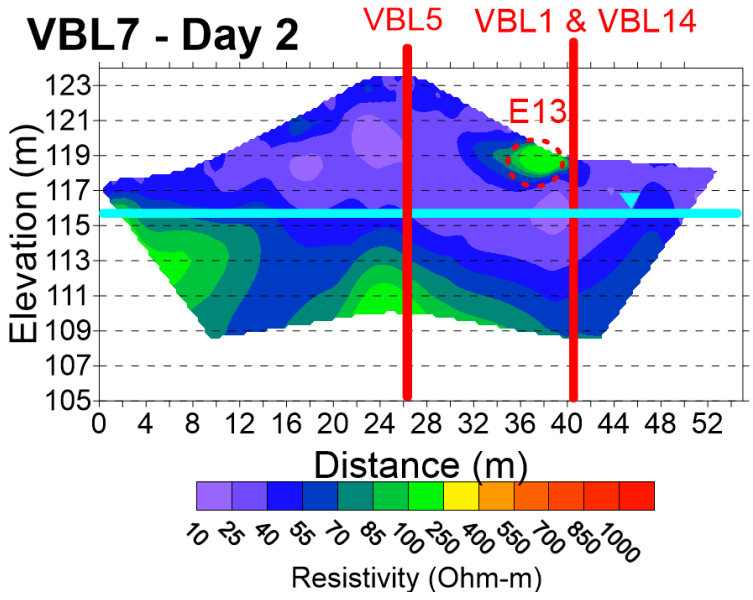

Appendix A-6 Internal erosion area transverse DC ERT Line VBL7

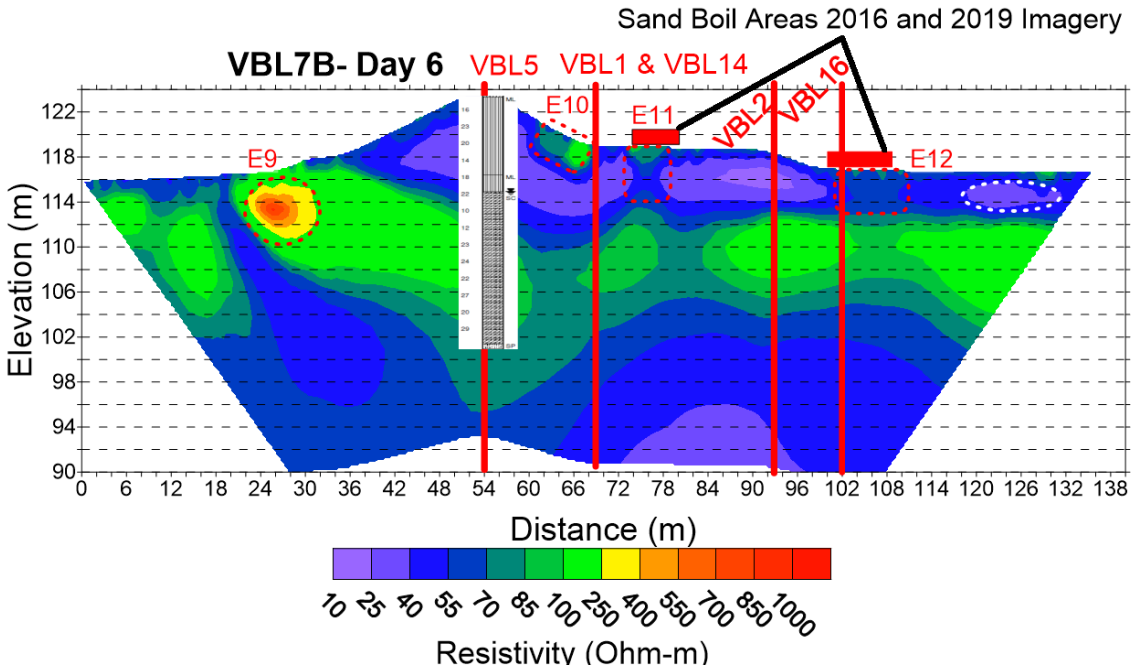

Appendix A-7 Internal erosion area transverse DC ERT Line VBL7B

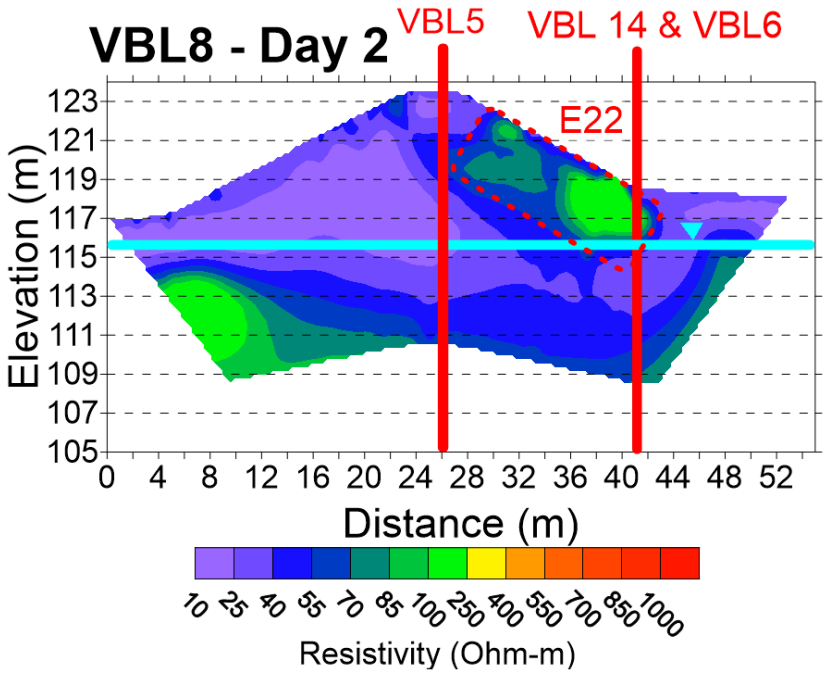

Appendix A-8 Internal erosion area transverse DC ERT Line VBL8

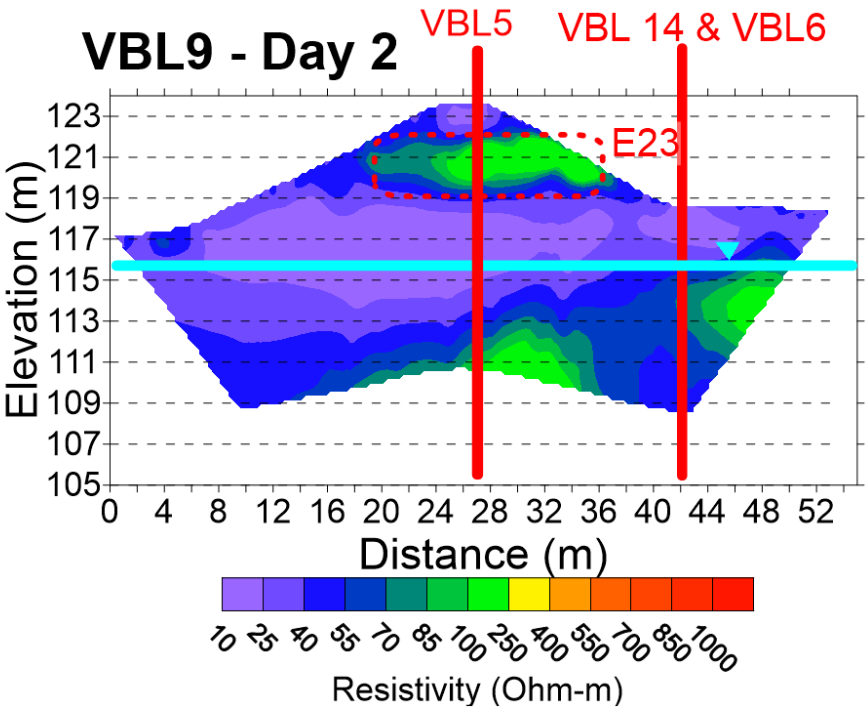

Appendix A-9 Internal erosion area transverse DC ERT Line VBL9

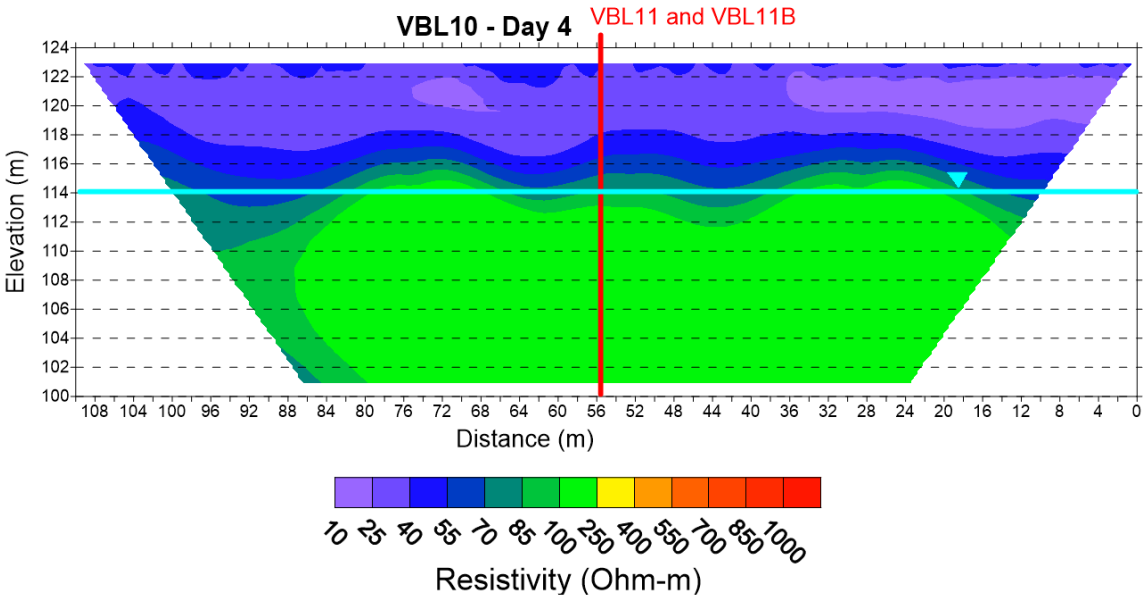

Appendix A-10 Control area longitudinal crest DC ERT line VBL10

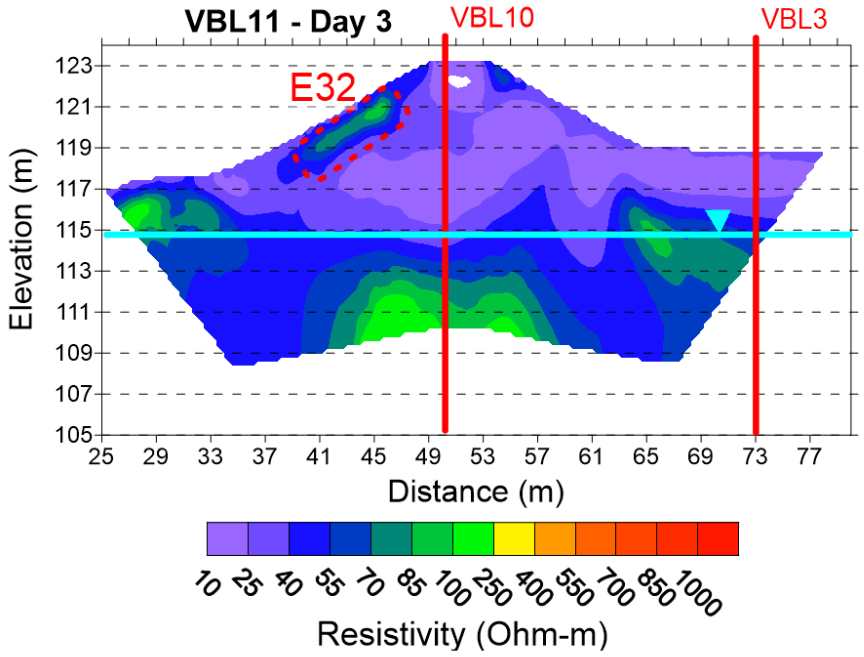

Appendix A-11 Control area transverse DC ERT Line VBL11

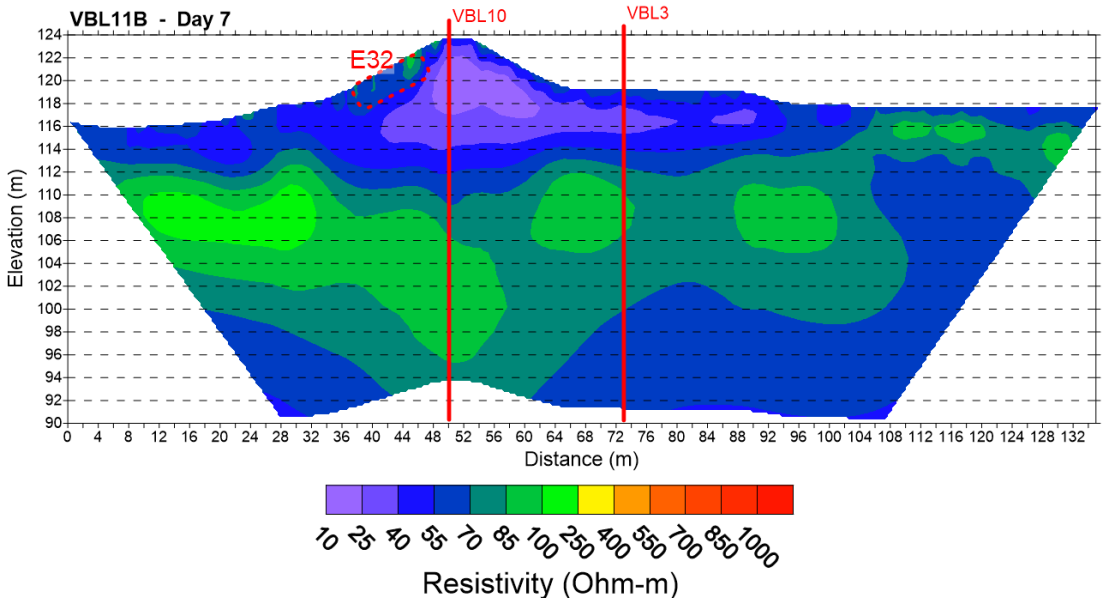

Appendix A-12 Control area transverse DC ERT Line VBL11B

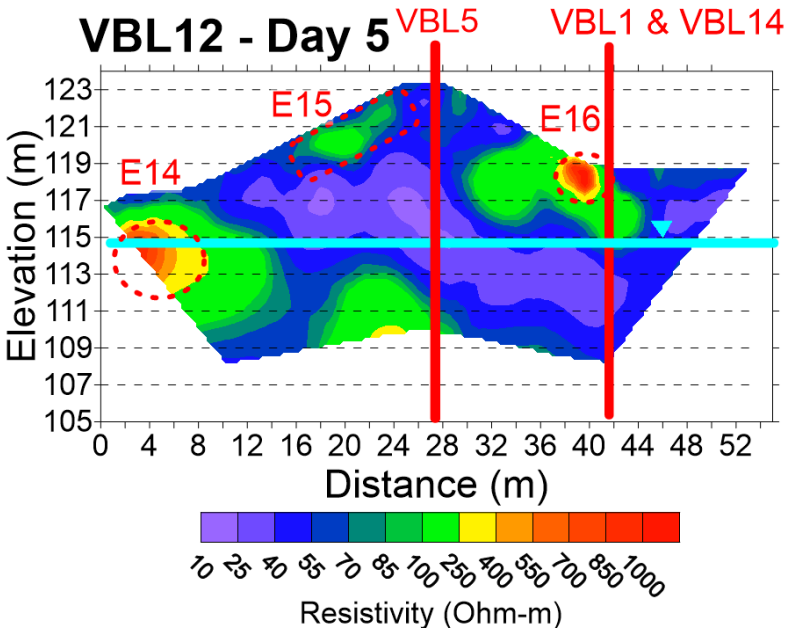

Appendix A-13 Internal erosion area transverse DC ERT Line VBL12

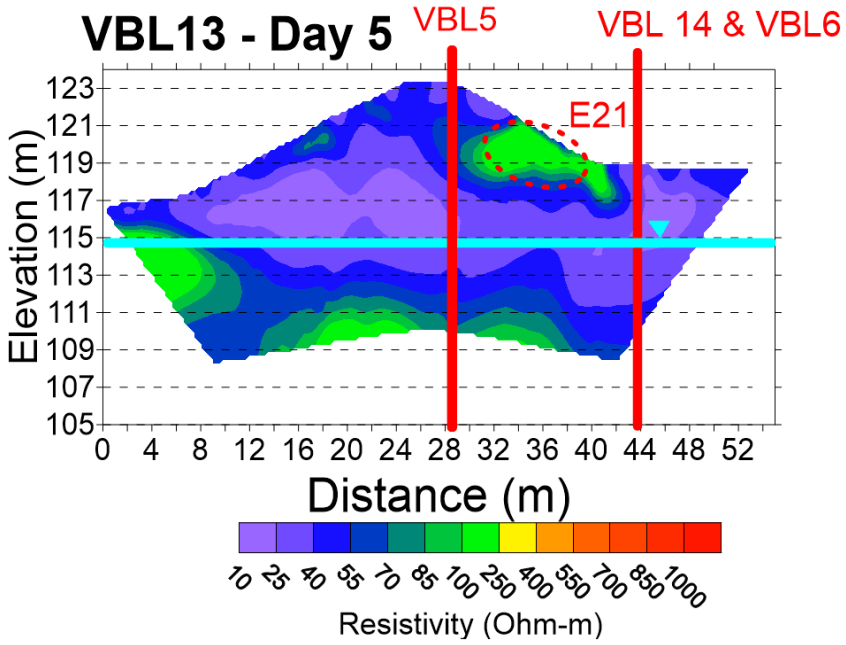

Appendix A-14 Internal erosion area transverse DC ERT Line VBL13

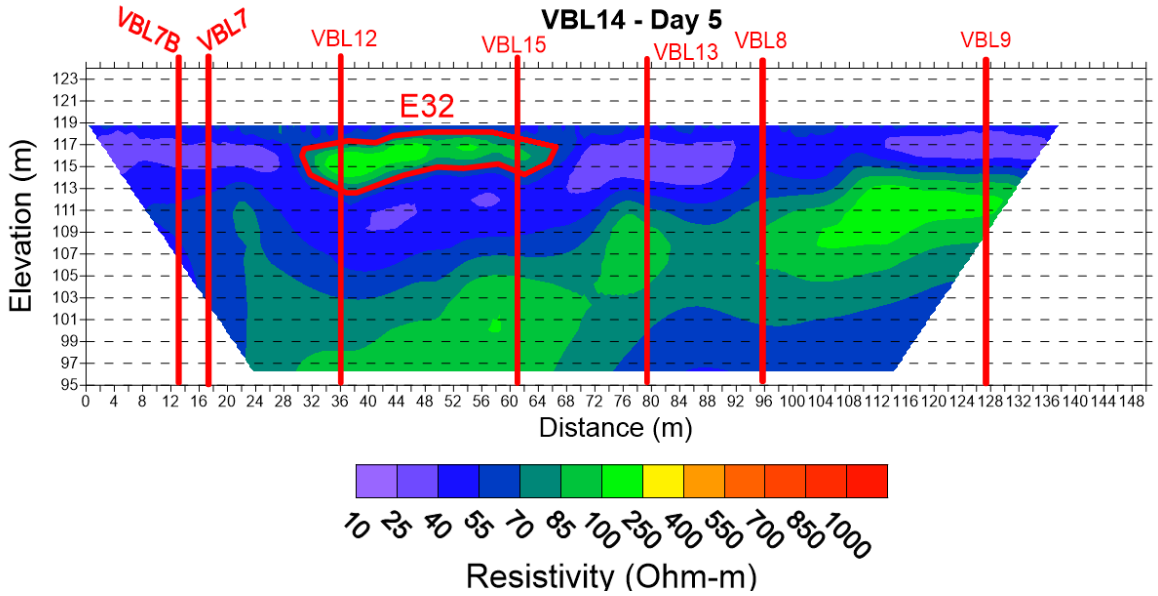

Appendix A-15 Internal erosion area longitudinal landside DC ERT line VBL14

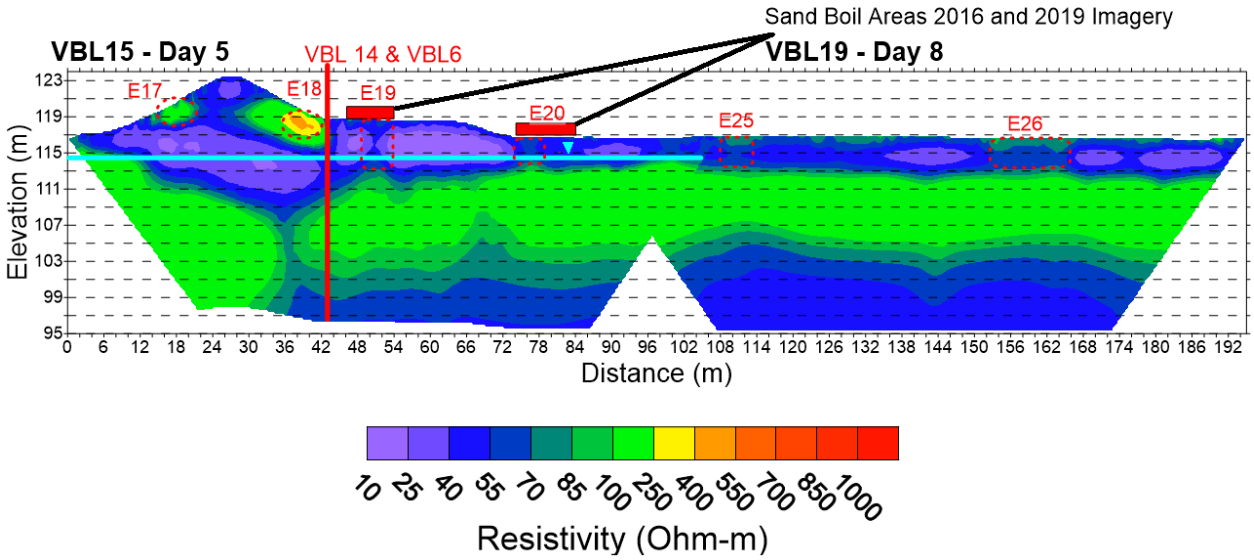

Appendix A-16 Internal erosion area transverse DC ERT Line VBL15 and VBL19

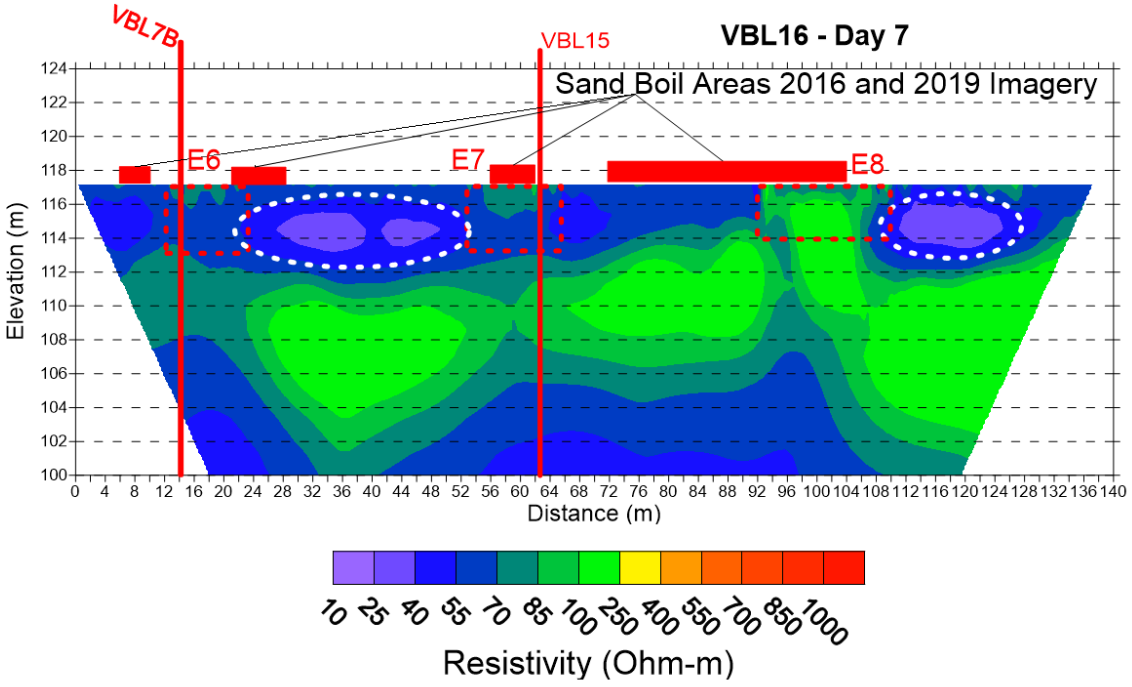

Appendix A-17 Internal erosion area longitudinal landside DC ERT line VBL16

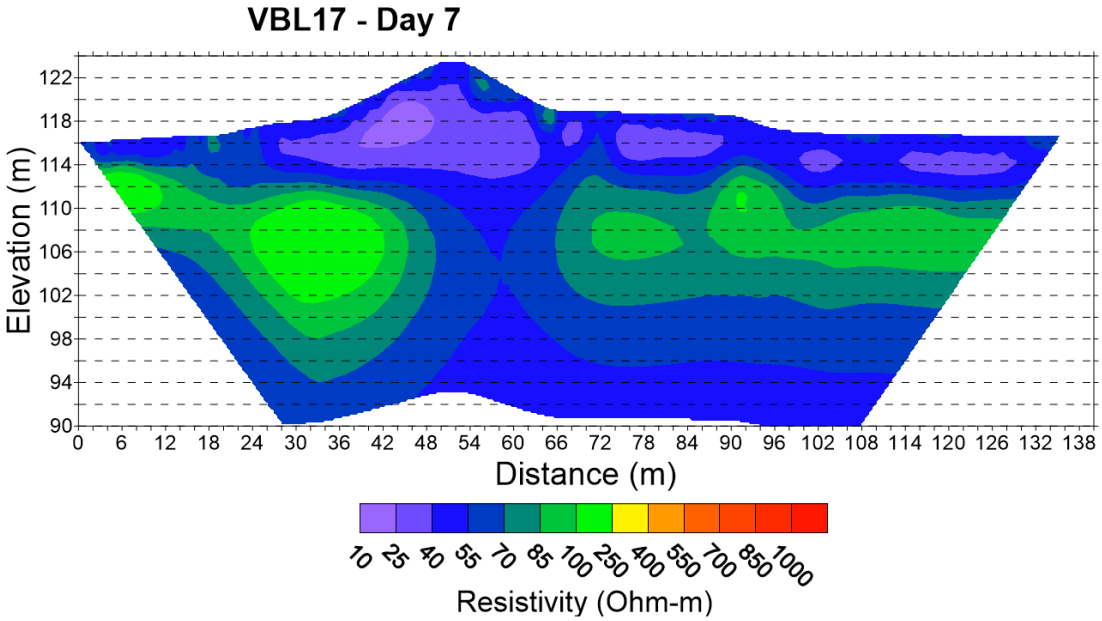

Appendix A-18 Transverse DC ERT line VBL17 located to the east of the internal erosion area

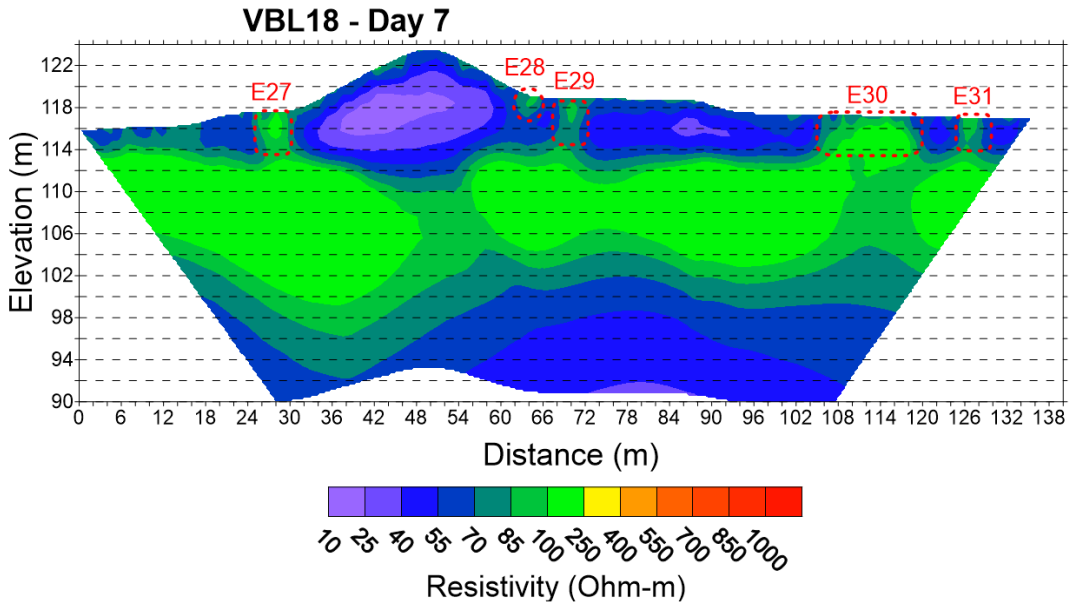

Appendix A-19 Transverse DC ERT line VBL18 located to the west of the internal erosion area

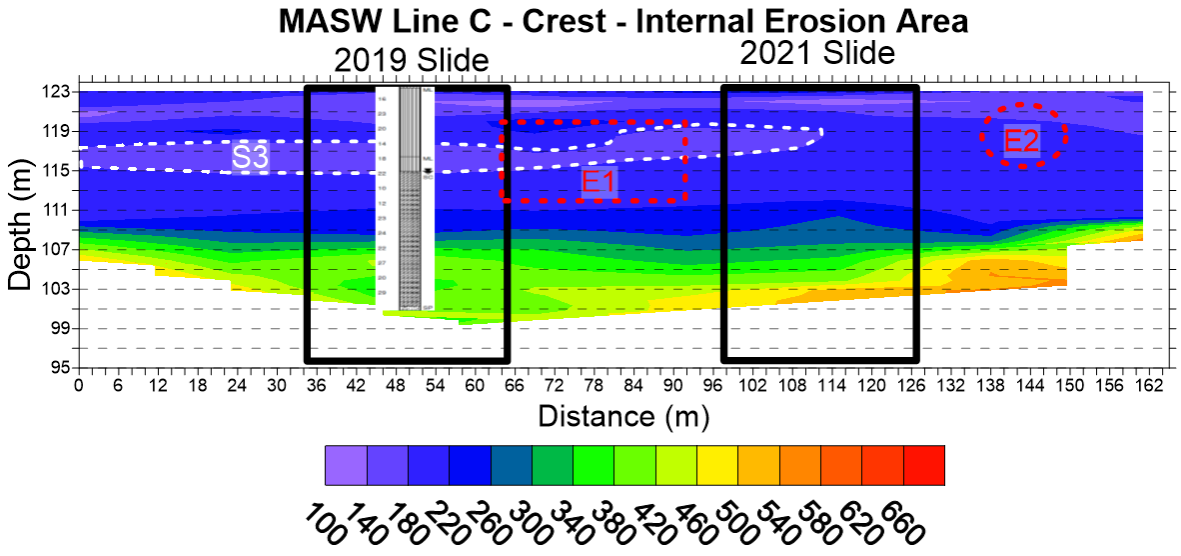

Appendix A-20 Internal erosion area crest MASW line C

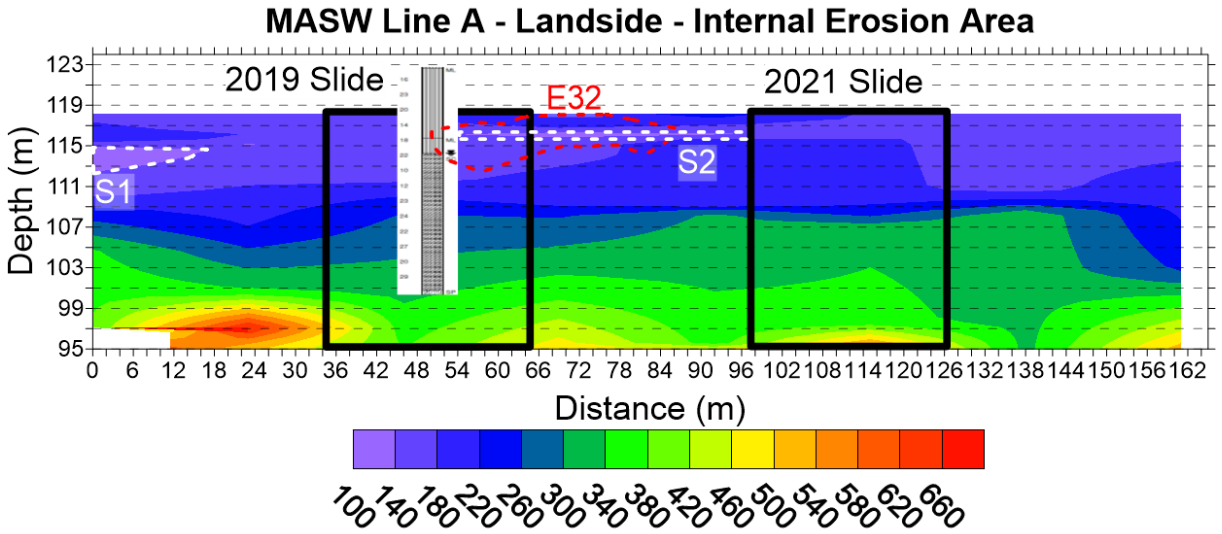

Appendix A-21 Internal erosion area landside MASW line A

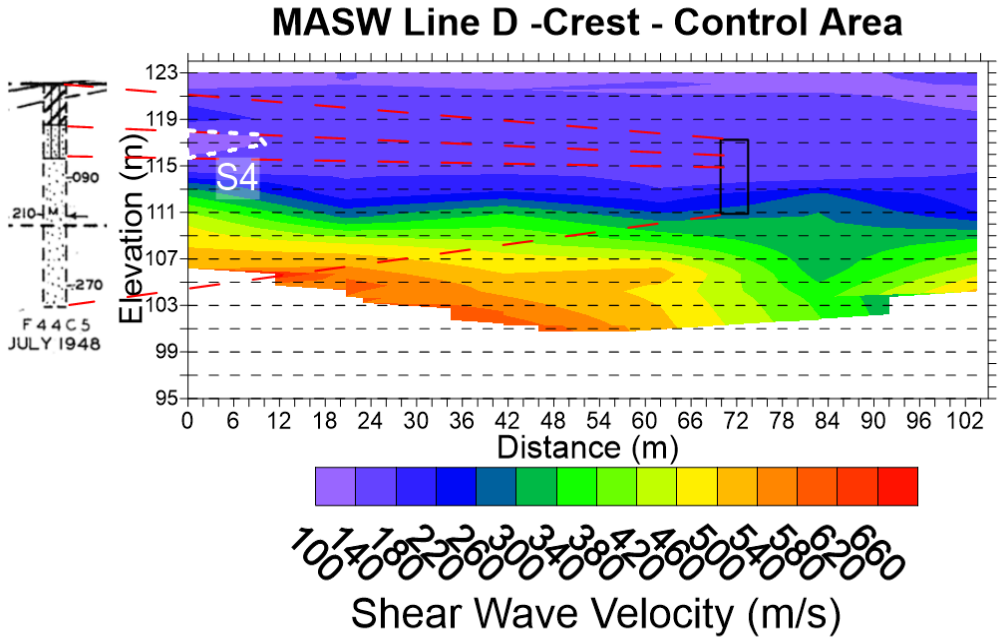

Appendix A-22 Control area crest MASW line D

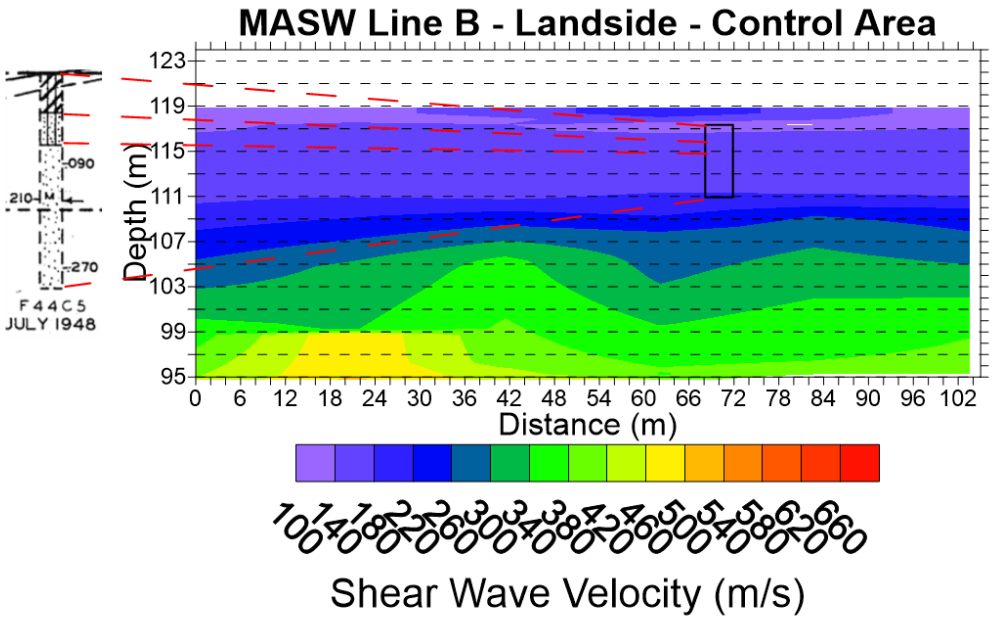

Appendix A-23 Control area landside MASW line B